Processing, Microstructure, and Mechanical Properties of Si_3N_4/SiC Nanocomposites from Precursor Derived Ceramics

Kevin Thomas Strong Jr.

A dissertation

submitted in partial fulfillment of the

requirements for the degree of

Doctor of Philosophy

University of Washington

2015

Reading Committee:

Rajendra Bordia, Chair

Brian Flinn

Lucien Brush

Program Authorized to Offer Degree:

Materials Science and Engineering

University of Washington

Abstract

Processing, Microstructure, and Mechanical Properties of Si_3N_4/SiC Nanocomposites from Precursor Derived Ceramics

Kevin Thomas Strong Jr.

Chair of the Supervisory Committee:

Professor Rajendra Bordia

Materials Science and Engineering

Polymer-derived ceramics (PDCs) provides a unique processing route to create Si_3N_4/SiC composites. Silazane precursor polyureasilazane (Ceraset PURS20) produce's an amorphous SiCN ceramic at temperatures of ~800 – 1200 ˚C and crystallizes to a Si_3N_4/SiC nanocomposite at temperatures >1500 ˚C. A novel processing technique was developed where crosslinked polymers were heat-treated in a reactive NH_3 atmosphere to control the stoichiometry of the pyrolyzed SiCN ceramic. Using this technique processing parameters were established to produce SiCN powders that resulted in nanocomposites with approximately 0, 5, 10, 20 and 30 vol. % SiC. Lu_2O_3 was added to these powders as a sintering aid and were densified using Hot Pressing and Field Assisted Sintering. The sintered nanocomposites resulted in microstructures with multiple-length scales. These length-scales included Si_3N_4 (0.1 – 5 μm), SiC (10 – 100 nm) and the intergranular grain boundary phase (<1 nm). Using a combination of SEM and TEM it was possible to quantify some of these microstructural features such as the size and location of the SiC. Hardness and fracture toughness testing was conducted to compared the room temperature mechanical properties of these resultant microstructures.

This research was intended to develop robust processing approaches that can be used to control the nanostructures of Si_3N_4/SiC composites with significant structural features at multiple length scales. The control of their features and the investigation of their affect on the properties of composites can be used to simulate the affect of the structure on properties. These models can then be used to design optimal microstructures for specific applications.

Acknowledgements

It has been a long and arduous journey in the pursuit of my PhD. This research took 6 long years and spanned 3 different continents and I myself physically resided at 3 different universities. This could not have been accomplished without the help and support of so many people along the way.

The University of Washington administrative staff was always helpful with day-to-day nuances, especially Bichtien Thach for always helping me with paperwork issues, Karen Wetterhahn, for making sure that I was on track with my PhD paperwork from the other ocean, and Tuesday Kuykendall, for always giving me some leeway when using department equipment. Thanks to the UW Bordia group members. Dr. Clifford Leslie, Dr. Kaishi Wang, and Dr. Nik Hrabe for helping me get settled in. The Flinn group for always listening when I was bouncing ideas off of them in the laboratory. Dr. Hanson Fong for teaching me electron microscopy, which was very useful later on in my research.

I would like to thank my Clemson University colleagues for all of their help, especially the original Clemson Bordia Group members: Dr. Thomas Konegger, Dr. Engin Ciftyurek, and Dr. Chen-Chih Tsai for welcoming me to Clemson and helping me set up the laboratory that I packaged and shipped from the University of Washington. An extra thanks to Dr. Chen-Chih Tsai for always going out of his way to help me with my research and his all around positive attitude that was great to have around during the final moments of my PhD. I also would like to thank the Clemson University Electron Microscopy centre for going out of their way to help me gather the images I needed for my research in a timely manner.

I would like to thank the people at the Centre for Microscopy and Microanalysis at the University of Queensland in Australia for hosting me during my research fellowship. Thanks to Dr. John Drennan for inviting me to come to his facilities. Although I like to think of it as repayment for helping him while he was a visiting scholar with the Bordia Group. A special thanks to Dr. Graeme Auchterlonie for taking time to teach me TEM during my time there as well for inviting me out for Wednesday bubbles, a tradition I hope to have some day. Also thanks to Zhi Zhang for babysitting me on the TEM every time I needed to use it, but always doing it with a smile. Thanks to the University of Washington's Graduate School for awarding me the Trans Pacific Fellowship, which allowed me to travel to Australia and conduct the TEM work in this thesis.

I would like to thank the people at Oak Ridge National Laboratory for all of their advice and allowing me to use some of their facilities. Thanks to Dr. Paul Becher for taking time out of his retirement to bestow some of his knowledge to a young researcher. Thanks to Shirley Walters for taking some time to help me use some equipment. A special thanks to Dr. Andy Wereszczak, not only for his advice during this PhD, but also for hiring me as a Post-Bachelor student prior to this work where my interest for mechanical properties of ceramics began.

Thanks to Dr. Zoltan Lences from the Institute of Inorganic Chemistry, Slovak Academy of Sciences for helping with the processing of my hot pressed samples and continuing to collaborate with us on this project.

I would like to thank the committee members, Dr. Lucien Brush and Dr. Brian Flinn for their time with this dissertation. A second thanks to Dr. Brian Flinn for taking the time to bestow his knowledge of the laboratory equipment down to me.

Thank you to my advisor Dr. Raj Bordia for giving me the opportunity to pursue a PhD with him. You gave me a lot of freedom to pursue the project in the manner I felt was most interesting and also was very encouraging for me to apply for travel fellowships, which allowed me to travel to Australia for research and to Brazil for a conference. You were also very supportive to send me to conferences and help expand my network. I look forward to continuing our relationship during my independent research career.

Finally I would like to thank the soon to be Dr. Shelly Arreguin for being my partner both in and outside of the laboratory. The last 6 years have been especially special having you there.

You have taught me so much from chemistry and polymer-derived ceramics to caving, climbing, mushrooms, burlesque and knitting. You were definitely the best part of my PhD adventure. Oh and thanks for hot pressing all of my samples, that was helpful too.

Last but not least, thank you Mom and Dad for supporting me through my entire academic adventure. I would not be where I am if it were not for your support.

This work was financially supported by UW GFSEI and AFSOR FA9550-09-1-0633.

Table of Contents

List of Figures

List of Tables

Chapter 1

Introduction

Ceramic materials have a very wide range of applications and are generally categorized into two groups: traditional (whitewares, electrical insulating porcelain, bricks, concrete, etc.) and advanced (bioceramics, structural engineering ceramics, electronic ceramics, etc.) ceramics. In either case ceramic properties are dictated by their structure, which can be categorized in two areas: atomic structure (atomic bonding and crystal/amorphous structure) and microstructure (grain size and morphology and grain boundaries). The intrinsic properties (e.g. the elastic modulus) of a ceramic material are dictated by its atomic structure. Once a material, its composition and atomic structure has been related, microstructure control and optimization is critically important. Currently research and development of ceramic materials are conducted utilizing the traditional materials science and engineering approach of processing-structure-property relationship. In general variables in a ceramic process are altered to change the microstructure of the resulting material, which dictates its properties. This phenomenological trial and error approach is repeated until a process is developed such that the resulting microstructure has optimized properties for specific applications. Although the ceramic science community has come a long way in understanding the processing-structure-property relationship, this empirical approach is associated with high cost and long development cycles.

Advancements in computational simulations, such as Finite Element Analysis (FEA) or Molecular Dynamics (MD), have helped identify microstructural features that dictate the mechanical properties of the materials (e.g. fracture toughness).[1,2] These numeric models can help identify microstructures not yet developed for improved properties. However, there lacks a predictive tool to optimize microstructures and a lack of approaches to optimize multiple properties. This study aims to develop an experimentally validated approach to numerically design nanocomposite ceramic microstructures for high temperature applications.

Applications where ceramics have been identified as necessary materials for high temperature applications include: advanced gas turbines[3,4], high temperature combustion engines and other related areas where temperatures exceed 1000 ˚C in a hot gas or oxidative environment.[5] High temperature metallic materials (e.g. Nickel-based superalloys) are limited to a real material temperature potential of about 1000 ˚C because of their inherent physical properties (melting temp, creep, oxidation etc.). Various ceramics have been subjected to comprehensive scientific studies in order to determine their use for these long-term elevated temperature applications. Non-oxide silicon based ceramics have the greatest potential for these applications as they exhibit low diffusion coefficients (due to their covalent bonding) and high oxidation stability (due to a SiO_2 barrier that forms at high temperatures).

Liquid phase sintered Silicon Nitride has been extensively studied as a top candidate for these high temperature gas turbines. The material exhibits high strength, wear resistance, and fracture toughness, however, it lacks high temperature creep resistance due to its glassy intergranular phase that is formed during processing from the oxide additives needed for processing. The addition of SiC nanoparticles has been shown to improve the high temperature stability of this material. An extensive amount of research has been done on this Silicon Nitride / Silicon Carbide ceramic composite, however, no research has been attempted to optimize the multiple properties in this material system. The complexity of this composite system combined with the various properties to optimize makes it the ideal material system for this study.

Chapter 2

Literature Review

2.1 Silicon Nitride/Silicon Carbide Ceramics

2.1.1 Nanocomposite Concept

Structural ceramics tend to show deterioration in their mechanical properties (e.g. strength, fracture toughness) at high temperatures. In the case of Silicon Nitride this can be attributed to the intergranular (or grain boundary) phase. Oxide additives are added to Silicon Nitride as a sintering aid in order to densify the material. (This will be discussed in more detail in Section 2.1.2.). These oxide grain boundaries can act as a glassy phase and soften at high temperatures causing a reduction in fracture toughness, strength and creep resistance.

The addition of SiC nanoparticulates (10 – 200 nm) to Si_3N_4 matrix as a reinforcing phase has been shown to enhance mechanical performance. Niihara *et al.* first demonstrated this concept by adding SiC nanoparticles to a variety of materials (e.g. Al_2O_3, Si_3N_4, etc.) and coined the term "Nanocomposite Concept."[6] When adding SiC at various volume % his team noticed that the SiC phase was located in different regions of the microstructure. If the SiC particles are sufficiently small (<100nm), the Si_3N_4 matrix grains will grow around and consume the isolated SiC particles during high temperature processing. If the SiC particles are larger (>200 nm) or if the vol.% is significantly high where clustering of the SiC particles can occur, the SiC phase is located between the Si_3N_4 grains phases within the grain boundary phase. If the vol.% of SiC is nearly equal to that of the matrix phase then grain growth is inhibited due to grain boundary pinning and both phases are of equal size. This then defines three types of nanocomposites: intra-granular, inter-granular, combination of intra/inter-granular nanoparticles and nano-nano structures where both the matrix and reinforcing phase are on the same length-scale (Figure 2.1).

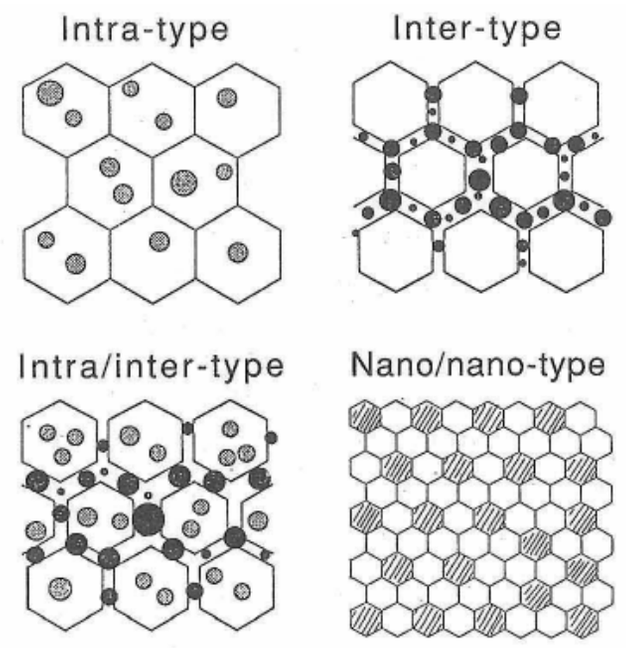

Figure 2.1 Schematic showing the different types of nanocomposites.[6]

Niihara and colleague's first studies on this material system were processed via hot pressing amorphous SiCN powders produced by chemical vapor deposition process.[7-14] The SiCN powders crystallize during the sintering process to produce the Si_3N_4/SiC nanocomposite. The group,[15,16] as well as others,[17-19] also produced nanocomposites via mixing commercially available crystalline powders of submicron sized Si_3N_4 and nanosized SiC powders and subsequent hot pressing or hot isostatic pressing. Various other methods of incorporating nano-grained SiC in Si_3N_4 have been studied. Si-based polymeric precursors have been widely used. One approach is the production of amorphous SiCN powders from pyrolyzed polysilazane precursors followed by either hot pressing, pressureless sintering or field assisted sintering.[20-23] SiCN powders have also been added in small quantities to commercially available Si_3N_4 crystalline powders as an additive followed by hot pressing.[24-26] Polysilazane precursor has also been used as a binder in its liquid form followed by a 3-stage heat treatment: cross-linking, pyrolysis and gas pressure sintering.[22,27] Other methods of producing amorphous SiCN powders include laser irradiation of gas mixtures[28,29] and laser interaction with droplets of a liquid

hexamethyldisilazane.[30] Another method to produce Si_3N_4/SiC nanocomposites is through the addition of SiO_2 and C black powders to Si_3N_4 followed by hot pressing. SiC forms in situ due to a carbothermal reaction process between the SiO_2 and C (Eq. 2.1).[31,32] A major

$$SiO_2(s,l) + 3C(s) \rightarrow SiC(s) + CO(g) \qquad \text{(Eq. 2.1)}$$

advantage of this process in comparison to the others stated is the cost effectiveness. SiC nanoparticles and preceramic polymers are expensive to purchase and the CVD method is costly to setup and produce large quantities of powders. SiO_2 and C are inexpensive and the high temperature densification process is the same or similar to the ones stated above.

As stated there are various creative ways of producing these nanocomposites. The starting powder in conjunction with the densification technique dictates the type of nanocomposite (Figure 2.1) that is produced. The location of the SiC particles and vol% has a profound effect on the high temperature properties. Niihara and colleagues' first studies showed increase in creep resistance and strength retention at high temperatures.[8,12,14,33,34] In their studies of the SiCN powders that produced high vol% (~40%) SiC they also found that the material exhibited superplasticity.[6,35] This was attributed to nano-nanostructures that were produced. The high vol% SiC caused grain boundary pinning of the Si_3N_4 phase, which inhibited grain growth forming equiaxed grains after densification. The equiaxed small grains allowed for grains to flow past one another during straining. One other group has produced these nano-nanostructures, more recently, through the use of SiCN powders (formed from preceramic polymers) and the use of field assisted sintering (FAST) for densification.[22,36] They also show a drastic improvement in creep resistance; however, they did not report the approximate vol% of SiC.[37] It is thought that the nano-nanostructure was formed due to the rapid densification in the FAST process compared to hot pressing, which did not allow time for grain growth to occur.

Most of the other processing techniques produce what is termed a micro/nano composite with micron sized (0.5 – 10 μm) Si_3N_4 and nanosized (10 – 200 nm) SiC with a mixture of intra- and inter- granular grains (type III in Figure 2.1). The inter-granular grains have been attributed to the improved high temperature properties. Niihara *et al* first explained this phenomenon as a result of direct mechanical bonding between the Si_3N_4 and SiC grains essentially creating a rigid bridge across the intergranular oxide phase.[6] This would prevent grain boundary sliding and subcritical crack growth at high temperatures. Pezzotti *et al* challenged this theory, stating that their improved high temperature properties were due to a modification of the grain boundary phase from chemical interactions with the reinforcing SiC phase.[17] It has been stated by multiple authors that improvements in creep resistance is due to hindrance of grain boundary sliding of the Si_3N_4 phase.[29,38-41] However, it has also been shown that localized grain boundary chemistry changes in the presence of SiC particles.[24,29,42,43] Specifically the thermodynamic calculations show the formation of MOx gaseous phases resulting in a loss of grain boundary glassy phase.[42] It is likely a combination of the two mechanisms, however, there is no definitive evidence that one mechanism is dominant over the other. It is accepted though that the inter-granular nano SiC is the reason for improved high temperature mechanical properties. A study, done by Besson *et al.*, with very low vol% SiC generated only intra-granular SiC. This study showed no improvements in creep resistance.[29]

Despite the lack of high temperature creep resistance; intra-granular nano SiC does improve other mechanical properties. Niihara et al first reported the interfacial structure of the intra- SiC and Si3N4. They showed specific Si_3N_4 and SiC crystal orientations have very low lattice mismatch. In TEM images there are flat interfaces between the Si_3N_4 grains and both α- and β-SiC grain with no interfacial phase.[44] In another report it was shown that some intragranular SiC grains exhibit an amorphous interfacial phase.[11] This is because of the liquid phase that exists during sintering of these nanocomposites. During sintering, SiC grains are able to rotate and orient to reduce interfacial energy due to the lattice mismatch. If the grains cannot

rotate enough due to a large lattice mismatch, a liquid oxide phase remains between the Si_3N_4 and intragranular SiC. These different types of interfaces between the Si_3N_4 and SiC grains have an influence on the hardness and fracture strength of these grains. Sajgalik *et. al.*[45] performed nano indentations on Si_3N_4 grains with and without intragranular SiC and showed a higher hardness value for the Si_3N_4 with intragranular SiC. However, measurement of microhardness has reported have shown both improved[21,45,46] or constant hardness as SiC content increases[43]. An increase in hardness with SiC content intuitively makes sense, as SiC is a harder material than Si_3N_4, however there is no explanation for lack of improvement in some studies.

It should be noted that the Si_3N_4/SiC ceramic material truly is a "nanocomposite concept" and not a "composite concept". Studies have been done on adding different size and shaped SiC to Si_3N_4 with little to no improved properties. The addition of SiC whiskers have shown to have little to no major room temperature strength improvements[47,48] and have actually shown deterioration in creep resistance and high temperature strength.[49-52] Addition of SiC platelets have shown to lead to a significant loss in room temperature strength as the platelets were considered to act as failure initiation sites.[53-57] The fracture toughness has shown mixed results with one group displaying a large increase in toughness[54] and others displaying only weak influences[55,57]. Creep of SiC platelet reinforced Si_3N_4 was shown to have both a slight increase[54] and deterioration in resistance[55-57]. Micron sized SiC particles have demonstrated strength retention at high temperatures, however, their was a decrease in room temperature strength.[58] Nanocomposites may show little to no influence on the room temperature properties of Si_3N_4; however, it has been consistently shown that these nanocomposites do improve the high temperature properties. Since for Si_3N_4, the critical properties are high temperature properties, Si_3N_4/SiC nanocomposites remain an active area of research.

2.1.2 Sintering Silicon Nitride

Sintering of ceramics occurs when compacted particles are heated to temperatures below that of the melting point (usually 2/3 of the absolute melting point). This allows for mass transport of ions, atoms or defects to move efficiently from areas of high chemical potential (grains and grain boundaries) to areas of low chemical potential (pores) to close pores to form a polycrystalline solid. There are three driving forces for this process: 1) curvature of the particle surface, 2) externally applied pressure and 3) a chemical reaction.

The surface curvature provides a driving force due to the particle systems drive to decrease its surface free energy (E_s). If we assume 1 mol of powder, E_s can be represented by

$$E_S = \frac{3\gamma_{SV}V_m}{a} \qquad \text{(Eq. 2.2)}$$

where γ_{sv} is the specific surface energy (i.e., the surface energy per unit area) of the particles, V_m is the molar volume and a is the radius of the particles.[59] An externally applied pressure during the heat treatment process can also drive the sintering process. This is related to the work (W) of the external applied pressure and is represented by

$$W = p_a V_m \qquad \text{(Eq. 2.3)}$$

where p_a is the applied pressure.[59] A chemical reaction can also provide a driving force for sintering, but is not considered because the microstructure control becomes difficult when a chemical reaction occurs concurrently with sintering.

Material transport path define the mechanisms of Solid State Sintering (SSS). These paths are illustrated in Figure 2.2.[59] Only certain mechanisms lead to densification or shrinkage of the particle compact and so the mechanisms can be separated as *densifying* and *nondensifying* mechanisms. Surface diffusion, lattice diffusion from the particle surfaces to the neck, and vapor

transport (mechanisms 1, 2, and 3) lead to neck growth without densification and are referred to as nondensifying mechanisms. These mechanisms reduce the neck curvature (i.e. the driving force) but do not close pores. Grain boundary diffusion and lattice diffusion from the grain boundary to the pore (mechanisms 4 and 5) permits both neck growth and densification. Plastic flow (mechanism 6) also leads to densification but is more common in metals rather than ceramics. In addition to these mechanisms defining the densification process, the rate of diffusion of the matter dictates the rate of densification. In ceramics, this is usually governed by the slowest diffusing species.

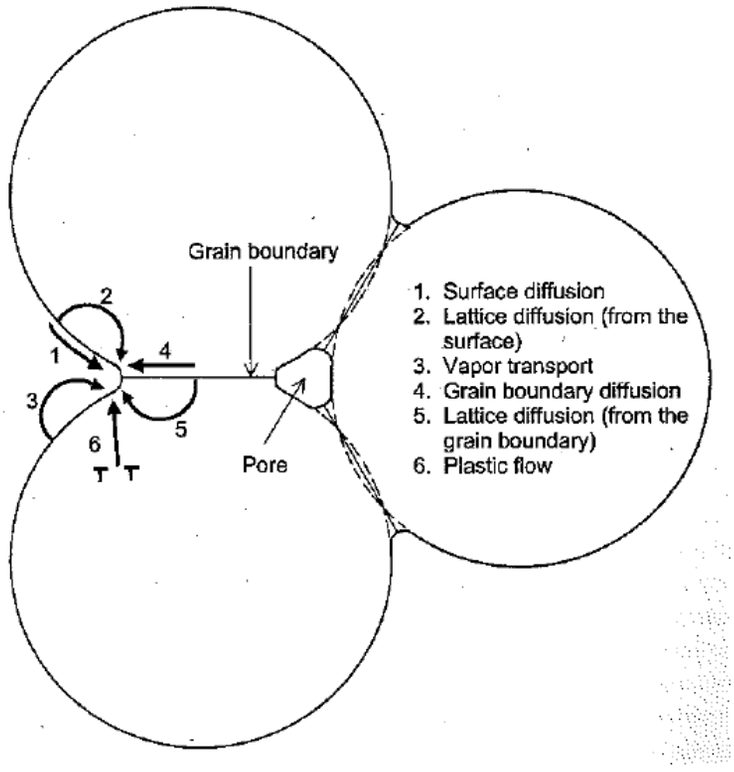

Figure 2.2 Schematic displaying six distinct mechanisms for sintering a consolidated mass of crystalline particles.[59]

Silicon Nitride is inherently a difficult material to sinter via SSS. The material does not have a melting point but decomposes to Si(*l*) and N(g) at 1884 ˚C at a N_2 partial pressure of 1 bar and thus has a high temperature limit for processing.[60,61] Silicon Nitride has a high degree of covalent bonding and is assumed to have very low lattice diffusion. The slow mass transport and

temperature limits of silicon nitride make it extremely difficult to densify by solid state sintering (SSS). Metal Oxide (MO) additives are used to aid densification through liquid phase sintering (LPS) as described below.

Silicon Nitride naturally develops a silica (SiO_2) layer on the surface of the particles. This combined with the MO additives allows for silicon based oxynitride glasses (nitrogen coming from the dissolved Si_3N_4 grains) to form at the grain boundaries. This enhances densification by enhancing 1) rearrangement of the particles and 2) matter transport through the liquid phase.[59] Rearrangement is much easier in the presence of a liquid phase because (assuming the liquid completely covers the particles) the friction between particles is reduced. The particles can rearrange easily under the compressive capillary stresses exerted by the liquid. Matter transport is enhanced because it is dependent on the rate of diffusion through the grain boundaries, which is a product of the grain boundary diffusion coefficient and grain boundary thickness. In LPS the grain boundary thickness is generally many times greater than in SSS and diffusion through a liquid is much faster than in solids, thus providing enhanced matter transport through the liquid.[59]

Early studies of dense silicon nitride ceramics prepared by hot pressing used magnesium oxide (magnesia) as a sintering aid.[62-64] Prior to this work it was believed that a complete phase transformation (trigonal $\alpha \rightarrow$ hexagonal β Si_3N_4) was necessary to achieve fully dense Si_3N_4, however, hot pressed silicon nitride with MgO additives clearly showed only partial transformation occurring.[63,65] This material drew great attention as it showed exceptional fracture toughness that was attributed to the elongated needle like grains that form during grain growth of the hexagon β-Si_3N_4. Further progress in silicon nitride sintering aids included the use of yttrium oxide (yttria)[66,67] or an yttria / aluminum oxide (alumina)[68-74], which resulted in higher density microstructures with improved mechanical properties. Significant effort has been placed on understanding how these sintering aids influence the resulting microstructures and thus the mechanical performances.

Growth kinetics of Si_3N_4 was studied by placing a small amount of α-Si_3N_4 in a Si-Al-Y-O-N glass. It was found that the α/β transformation and Ostwald ripening can be considered as different kinetic stages of grain growth. During the phase transformation process the β phase grain growth was predominantly in one direction along the c-axis indicating. The growth of the prismatic and basal plane was independent indicating that growth of the basal plane was interface controlled.[75] This basic understanding led to change in the sintering profile of this material system in order to control the resulting microstructures.[76] The addition of a small amounts of β-Si_3N_4 to the starting α-Si_3N_4 powder can act as seeds to allow for large elongated grains to form.[73] Other studies of this intergranular system have shown that crystalline β-SiAlON can grow epitaxially on the β-Si_3N_4, which can influence the mechanical performance (Sec. 2.2.2).[69,77]

Research has also been performed on rare-earth oxides (REOs) other than Y as sintering aids (e.g. La, Sm, Yb, Lu). It has been found that the aspect ratio of the β-Si_3N_4 increases with increase in RE ion size (La>Sm>Y>Yb>Lu).[78] This has been attributed to the larger RE ions having a greater affinity to bond to the prismatic plane of the β-Si_3N_4 rather than the glass phase. This was proven numerically by calculating the binding energies of each RE and their affinity to bond to N vs. O. It was also seen through STEM experiments that there are more bonding sites for La vs. Lu.[79] Because of this, the prismatic plane grows at a slower rate for the larger RE allowing for higher aspect ratio β grains to grow.

Besides the anisotropic growth of the β-Si_3N_4 the viscosity of the intergranular phase was studied. This is important as the viscosity of the glassy intergranular phase can not only affect the microstructure during sintering, but also affect the high temperature properties, such as creep, fracture toughness and strength. For the REOs, the smaller the ion size in the glass the higher the viscosity. This is due to the higher cationic field strength leading to stronger RE–(O, N) bonds.[80] The higher viscosity glassy phases have been shown to need higher processing temperatures, as the intergranular phase cannot efficiently spread throughout the microstructure causing pockets

of glass to form.[81] Depending on the composition of the intergranular phase, sometimes crystallization will occur.[66,82,83] This also can affect the high temperature mechanical properties.

In addition to the investigation of sintering aids, much work has been done with various types of densification techniques (e.g. hot pressing, hot isostatic pressing, gas pressure sintering, electric field assisted sintering). The majority of research has focused on hot pressing because it provides mechanical stress, which aids the densification mechanisms discussed above.[59] It is also a simpler setup compared to hot isostatic pressing. Recently there have been significant developments in using field assisted sintering (FAST) for silicon nitride materials.[84,85] FAST research in silicon nitride ceramics has focused around an apparatus called Spark Plasma Sintering (SPS) unit. Although it has been proven that there is neither spark nor plasma during this process, many investigations still use SPS as the name of the process. This study will refer to the process as FAST sintering. A schematic of the FAST apparatus is shown in Figure 2.3. A graphite die containing the powder material is placed between two electrodes. Force is applied to the graphite punches and the electrodes supply pulsed direct current through the graphite die. The temperature is measured on the outside of the die by using either an optical pyrometer or radiation camera.

FAST sintering has shown to produce fine grain microstructures in silicon nitride ceramics.[86,87] One proposed reason states that the very high heating rates (>100 ˚C) and the short hold time needed for complete densification does not allow the microstructure to coarsen.[88] Besides finer grain sizes silicon nitrides have shown enhanced densification rates at lower temperatures (<1700 ˚C) using FAST. The wetting of the glass phase on the Si_3N_4 particles enhances when an electric field is applied. This new densification mechanism has been termed electrowetting.[89] FAST is an attractive technique for fabrication of parts as it can reduce the temperatures needed for sintering and have short processing times. These advantages can significantly reduce the cost of parts. However, FAST with the SPS unit is limited to cylindrical

parts because of a build up in charge density at the corners of dies with sharp corners (e.g. square parts).

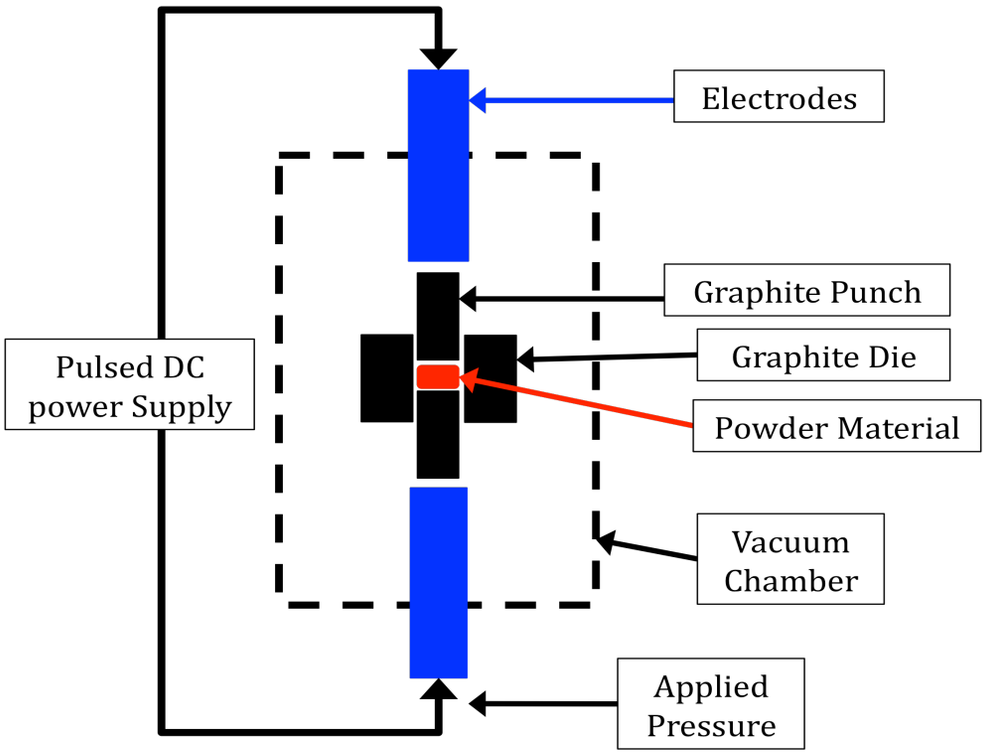

Figure 2.3 Schematic of FAST process.

2.2 Mechanical Properties of Si_3N_4/SiC Composites

2.2.1 Creep

For structural materials that are to be operated at elevated temperatures (e.g. turbine blades, engine valves, etc.), creep is an important property to optimize. Creep is the tendency of a solid material to deform in a time dependent manner leading to permanent deformation. For metals and ceramics creep is generally investigated at a constant low stress (< Yield Strength) and at a constant high temperatures. Three stages of creep observed during testing shown in Figure 2.4, i) Primary, ii) Secondary, and iii) Tertiary stages. The material being tested will initially exhibit a decrease in strain rate over a relatively short period of time until it reaches a steady strain rate. The secondary stage occurs over a long period of time and is the focus of most studies involving

creep. During the Tertiary stage the part will have an increase in strain rate until the part fails. The secondary stage, known as steady-state creep, is usually described by the Norton creep equation:[90]

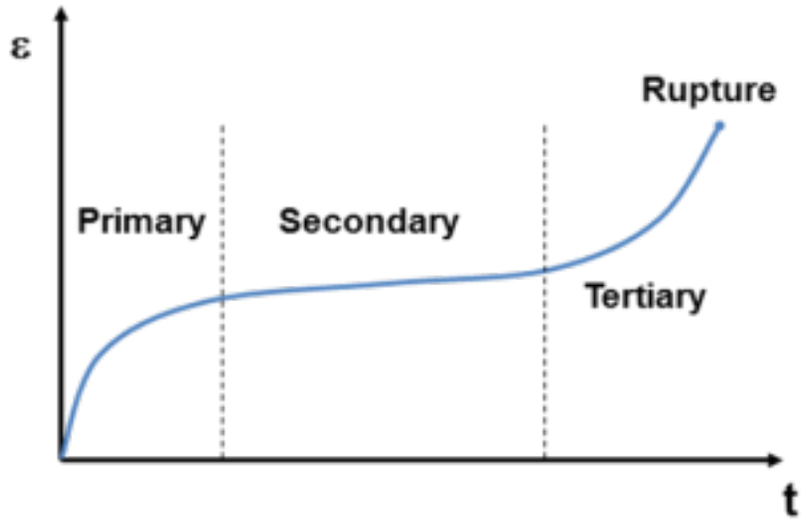

Figure 2.4 Typical strain vs. time plot of a creep test that indicates the three stages of creep: i) Primary, ii) Secondary, and iii) Tertiary.

$$\dot{\varepsilon}_s = A\sigma^n \exp\left(-\frac{Q_c}{RT}\right)\left(\frac{1}{d^m}\right) \qquad \text{(Eq. 2.4)}$$

where $\dot{\varepsilon}_s$ is the steady state strain rate, A is material dependent constant, σ the stress, n the stress exponent, Q_c the activation energy for creep, T the temperature, R the Boltzmann constant, d the grain size, and m the grain size exponent.

Models of diffusional creep in polycrystalline materials have been developed that yield realistic creep strain rates compared to experiments for steady-state creep.[91,92] At elevated temperatures and relatively low stresses (much lower than the yield strength) creep is governed by diffusion of interstitials or vacancies through the crystal lattice (Nabarro-Herring)[91] or through the grain boundaries (Coble)[92] from areas of compression to areas of tension. At lower temperatures diffusion is essentially frozen and diffusional creep mechanism is unimportant

compared to dislocation motion mechanisms of deformation. If a liquid phase is present between the grain boundaries the crystal phases become partly soluble and deformation is governed by dissolution-precipitation of the crystal grains in the glassy grain boundaries.[93] In ceramics this solubility is caused by a eutectic melt that can form between the grain faces and glassy grain boundary phase. There are two mechanisms that govern the rate of creep by solution-precipitation mechanisms: 1) interface reaction between the grains and glass or 2) transport through the glass phase. The slower of the two will be the rate-limiting factor. Raj was the first to develop creep equations based on the interface reaction and glass transport mechanisms shown in Eq. 2.5 and 2.6 respectively.[94]

$$\dot{\varepsilon}_1 = \frac{\sigma\Omega}{2RT(1-x)}\frac{k_1}{d} \qquad \text{(Eq. 2.5)}$$

$$\dot{\varepsilon}_2 = \frac{\sigma\Omega\bar{c}}{(1-x)\eta}\frac{\alpha}{d^3} \qquad \text{(Eq. 2.6)}$$

where Ω is the molecular volume, k_1 the rate at which atoms are exchanged between the glass and crystal at the interface, *(1 - x)* is a factor that takes into account that only a specific area fraction in the glass phase that occupies the two grain junctions (x) can support stress, $\bar{c}$ is the average molar concentration, η is the viscosity of the glass phase, $\alpha = xh/\Omega^{1/3} \approx 1$ and h is the thickness of the two grain junction. Wakai built up this model to include boundary conditions of the liquid phase. [95] Focus was emphasized on a step model where atoms dissolve and precipitate at the kinks and steps of the crystal interface.

Steady-state creep in Silicon Nitride ceramics is explained by the solution-precipitation mechanisms described above. As described in Section 2.1.2 Silicon Nitride contains an oxide grain boundary phase formed during processing from the necessary sintering aids added. The glassy grain boundary phase is the cause for the solution-precipitation creep described above. When tested in compression, Silicon Nitride follows the Norton Equation (Eq. 2.4) quite well with activation energies attributed to solution precipitation mechanism. However, when tested in

tension, cavity formation has been shown to form at the multi-grain junction and the power law formulation shown in Eq. 2.4 does not satisfactorily represent it's dependence on stress (stress exponent value is dependent on the value of applied stress), but an exponential representation is more suitable. A model has been developed to represent this type cavity formation as:[96,97]

$$\dot{\varepsilon}_C = \frac{\dot{\varepsilon}_0}{\eta} \frac{V_f^3}{(1-V_f)^2} \sigma \exp(B\sigma) \qquad \text{(Eq. 2.7)}$$

where $\dot{\varepsilon}_0$ and B are fitting parameters, and V_f is the volume fraction of the secondary glassy phase. Because viscosity is temperature dependent, $\eta \approx \eta_0 \exp(Q/RT)$, and $\dot{\varepsilon}_0$, V_f and η_0 are material dependent constants, Eq. 2.7 can be rewritten as:

$$\dot{\varepsilon}_C = A\sigma \exp(B\sigma) \exp\left(\frac{-Q}{RT}\right) \qquad \text{(Eq. 2.8)}$$

For this model, the exponential dependence of creep rate on stress results from the kinetics of the secondary phase redistribution from growing cavities. It should be noted that cavitations has also been shown to form in compression creep, however, this only occurs when the strain is in excess of 0.1%.[98] One interesting thing to note from the cavity formation model compared to diffusion based creep is that Eq. 2.8 does not have a grain size dependency. This is because the rate-limiting step for cavity formation is dependent on the physical flow of the glassy phase from the cavity. In either case the secondary phase is of much importance when trying to improve the creep resistance of Si_3N_4 ceramics, specifically the viscosity of the secondary phase.

Studies have been done in order to create more refractory grain boundary phases by adding REOs such as yttrium oxide.[82,99] These REOs can lead to higher viscosity phases and in some cases can lead to crystallization at the three grain junctions, however, some glassy phase still remains between the crystalline oxide and the Si_3N_4 phase. The thickness of this region is dependent on the composition of the sintering aid.[100] It is well known that the REOs allow for

enhanced creep resistance as compared to more traditional sintering aids such as MgO and Al_2O_3. Recent creep studies in tension using various REOs as sintering aids shows an increase in creep resistance with decrease in RE ion size (i.e. from La^{3+} to Lu^{3+}).[46] This can be attributed to an increase in viscosity with an increase in cationic field strength and thus a decrease in the RE^{3+} ions.[80,101-104] Sajalik *et al.* also stated that the Lu containing Si_3N_4 had crystalline oxide phases formed in the grain boundary regions, whereas the La containing Si_3N_4 did not. A combination of the high viscosity and crystalline phase makes Lu an attractive sintering aid for high temperature creep resistance.

The addition of nanosized SiC particulates also causes an increase in creep resistance in silicon nitride ceramics[24,29,33,37-41,46,105,106] This is an interesting situation because SiC causes refinement of the Si_3N_4 microstructure due to grain pinning, however, as shown in Eq. 2.4 creep rate is inversely proportional to grain diameter. The increase in creep resistance of Si_3N_4/SiC nanocomposites is under rigorous debate without a definitive answer. One conclusion is that the increase in creep resistance is attributed to intergranular SiC. Intragranular SiC located within the Si_3N_4 grains do not play a role in enhancing creep resistance. Two separate studies have shown that Si_3N_4/SiC nanocomposite with mostly intragranular SiC did not show any improved creep resistance compared to the monolithic Si_3N_4.[29,46] They did show an improved creep resistance when a Si_3N_4/SiC nanocomposite was fabricated with mostly intergranular SiC grains. There are two proposed mechanisms for increased creep resistance: 1)intergranular phase increases the viscosity of the glassy phase due to chemical reactions during the formation of SiC, or reactions with SiC causing a reduction in oxygen content[17,42] and 2) SiC reduces grain boundary sliding by obstructing the easy path of flow in the grain boundary glass phase by causing interlocking of the Si_3N_3 grains from direct mechanical bonding of the intergranular SiC phase (Figure 2.5).[29,41,105,106] Increase in viscosity of the glass phase has been shown when excess carbon is in the system from the SiC inclusions.[40] Excess carbon causes a carbothermal reduction of silica located in the glassy grain boundary phase by Eq. 2.1. The reduction of silica

in the glassy grain boundaries pushes the melting point to higher temperatures causing an increase in viscosity, but can also cause crystallization to occur. Increased creep resistance has also been reported where no reduction in oxide content has taken place, which implies that the developed microstructure of the intergranular SiC grains caused increased creep resistance.[46]

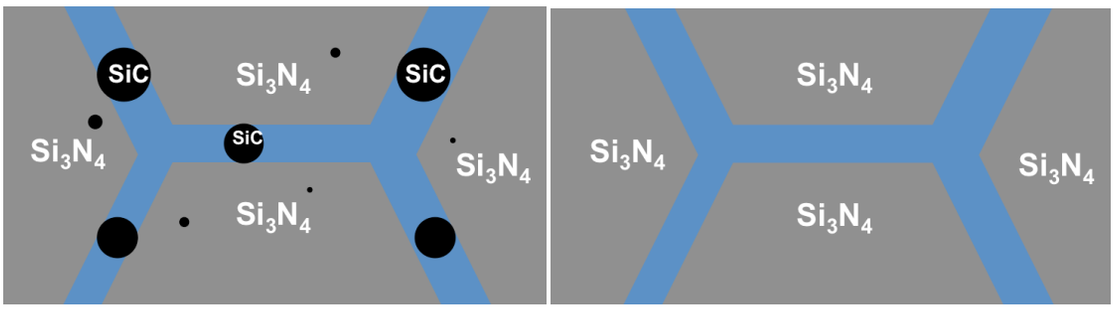

Figure 2.5 Example of intergranular SiC obstructing flow of the grain boundary phase (left) compared to just Si_3N_4 (right).

Recent reports using PDCs and FAST have shown some of the highest creep resistant Si_3N_4/SiC nanocomposites.[37] The structure of this nanocomposite is a nano-nanostructure where both the Si_3N_4 and SiC grains are on the nanoscale size length (~40 – 70 nm). This is opposite than what is expected according to the creep equation where strain rate is inversely proportional to grain size (Eq. 2.4). Although Wan *et al.* produced a dense part without the addition of sintering aids, which is likely why there is improved creep resistance.[37] Pezzotti *et. al* have also been able to show superior creep resistance without the use of a sintering aid by using hot isostatic pressing and high temperatures.[107]

In summary, from the results published up to date the most important aspects of improving the creep performance of Si_3N_4 is the chemistry of the grain boundary phase and the use of nano-sized SiC to restrict grain boundary sliding.

2.2.2 Fracture Toughness

Ceramics are inherently brittle in nature and tend to fail in a catastrophic manner in comparison to other structural materials (e.g. metals), which can plastically deform prior to failure. Many of the exceptional properties of ceramics (such as its high temperature resistance, thermal shock resistance, low density) are overshadowed by their inherent brittle behavior. This has led to rigorous studies in understanding and attempting to improve the fracture properties of brittle materials. A variety of ways have been explored to improve the fracture toughness (i.e. a materials resistance to crack propagation) of ceramics.

Fracture toughness of a material is described by its applied stress intensity factor, K_{appl}. Failure in a brittle material starts from a preexisting crack and occurs when K_{appl} exceeds a critical value K_R, known as the crack growth resistance. For an ideally pure brittle material (e.g. glass) the failure of a part can be related to the stress intensity facture by:[108]

$$K_{IC} = Y\sigma_f\sqrt{\pi a} \qquad \text{(Eq. 2.9)}$$

where K_{IC} is the critical stress intensity factor in mode I failure, Y is a so called geometric function dependent on the type of crack, type of specimen geometry, and type of loading, and a is the crack length. Mode I failure is described as an extension of a crack in uniaxial tension. Since brittle materials typically always fail in tension, Mode I failure is typically used to describe the fracture mechanics of ceramics and glass instead of Mode II (in plane shear) or Mode III (out of plane shear) (Figure 2.6).

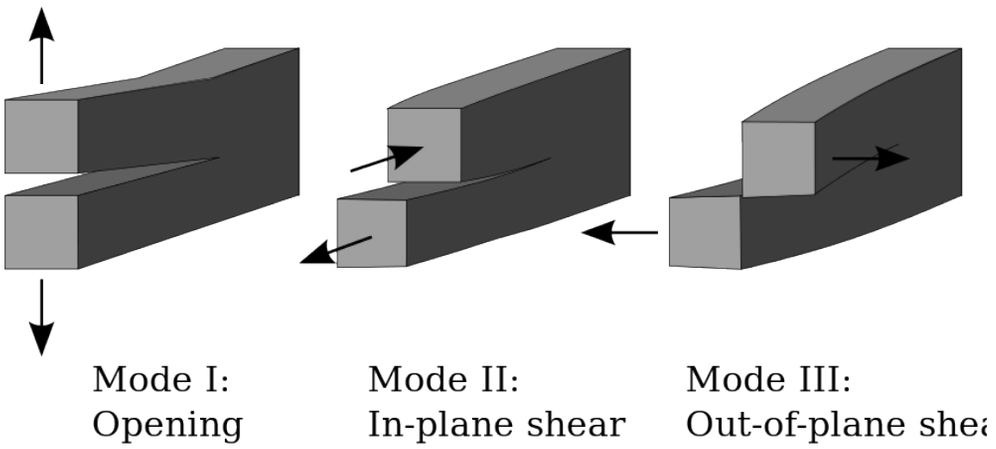

Figure 2.6 The three basic crack loading modes used in linear elastic fracture mechanics: Mode I: uniaxial tensile (opening), Mode II: In-plane shear, and Mode II: out-of-plane shear.[108]

As can be seen in Eq. 2.9 the failure of a purely brittle material can be predicted based on K_{IC} and the flaw size (i.e. the crack length a). Griffith first explained this concept (known as the Griffith flaw criteria) where the flaw size is described as a half-penny crack on the surface, or an elliptical crack within the material.[109] With this criteria improvements in processing and machining of ceramics has led to reduction of flaw and therefore high strengths.[110] However, if one considers a high strength ceramic (800 MPa) with moderate fracture toughness (K_{IC}=5 MPa$\sqrt{m}$), it requires cracks to be less than 25 μm. This extreme sensitivity to flaw size causes the need for very stringent processing protocols and machining, but also limits many applications where damage introduced in service can occur (e.g. cyclic fatigue, creep damage, thermal gradients and/or shock and impact or contact damage). Therefore, it is necessary to understand and attempt to improve the toughness of these ceramic materials.

In studying the fracture behavior of polycrystalline alumina, it was first noticed by Hubner *et al.* that the stress intensity factor, K_R, is not a constant, but in fact is dependent on the crack extension Δa.[111] The dependency $K_R=f(\Delta a)$ is known as the R-curve (Figure 2.7a). Among the mechanisms that can cause this rising R-curve behavior include: crack deflection[112],

crack bridging[113], microcracking[114], and phase transformations[115]. Together, these mechanisms have been termed as "toughening mechanisms".

Crack bridging mechanisms have been heavily researched as one of the potentials ways of improving toughness of ceramics through microstructural design.[113] In bridging mechanisms only partial crack face separation is observed (e.g. crack growing in a coarse-grained ceramic). Remaining crack-surface interactions cause so-called "bridging stresses" which act against the externally applied load (Figure 2.7b). Other ways of incorporating these "bridging stresses" involve adding a secondary discontinuous elastic reinforcing phase, such as fibers, whiskers, or platelets.

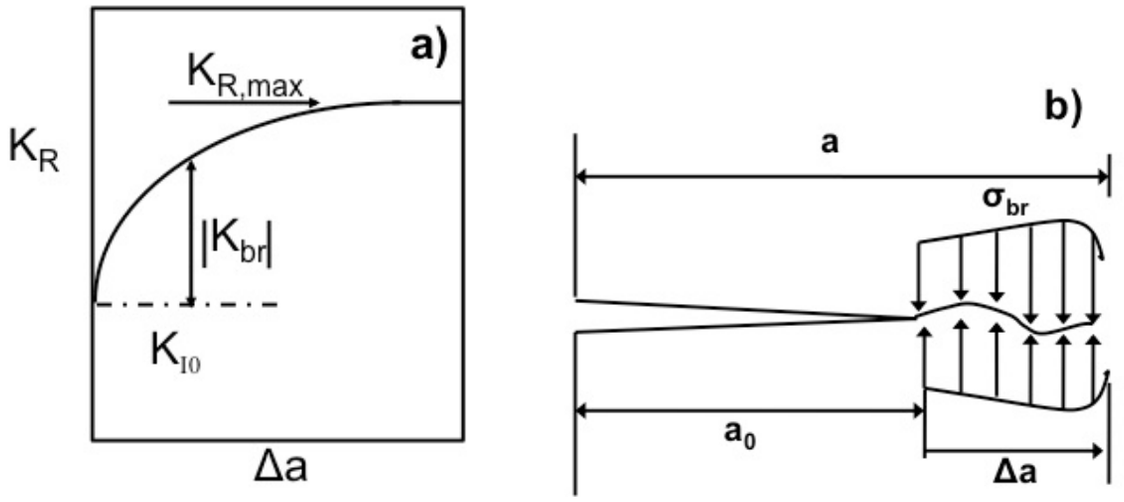

Figure 2.7 a) Schematic of an increasing crack growth resistance curve starting from the crack-tip toughness K_{I0} and exhibiting a saturation value $K_{R,max}$, b) a crack in a ceramic material exhibiting crack surface interactions described by bridging stresses.[116]

In Silicon nitride based materials, the focus has been on microstructural development of elongated β-Si_3N_4 grains, which act as a self-reinforced elastic bridging phase. These elongated grains can deflect cracks or create elastic crack bridging zones causing a resistance to crack growth and increase in toughness.[113,117] As discussed in Section 2.1.2 a large amount of research has been conducted in understanding the anisotropic growth of the β-Si_3N_4 phase. Generally

speaking the higher aspect ratio grains have shown increased toughness, which allows for a larger amount of frictional drag during pull out.

Another important aspect for improving toughness is observing the interfacial strength between the β-Si_3N_4 phase and the glassy grain boundary phase. It is necessary for the β-Si_3N_4 to debond from the matrix to allow for the necessary bridging stresses to occur (Figure 2.8). Studies have been conducted to observe the effect on the composition of the grain boundary glassy phase on the interfacial strength between the β-Si_3N_4 crystal and glass. When Al_2O_3 was used as a sintering aid, it was seen that β-SiAlON would grow epitaxially on the β-Si_3N_4 crystal. This SiAlON phase drastically increased the interfacial bonding due to the strong bonding of the Al across the glass/crystal interface. This study was important to consider the chemical bonding between the intergranular glassy phase and the β-Si_3N_4 crystal.[77,118]

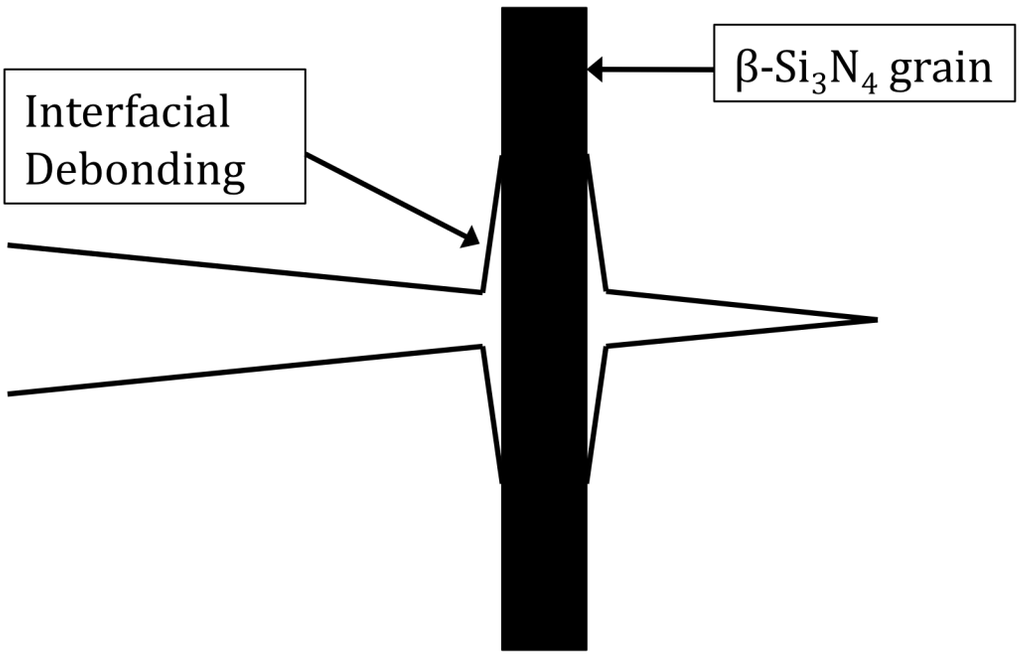

Figure 2.8 Schematic representing the necessary interfacial debonding for bridging mechanism to occur as a toughening mechanism.

Significant progress in understanding and improving the toughness of Si_3N_4 has been accomplished over the past several decades. However, until recently it has not been possible to

measure the full R-curve of these materials (Figure 2.7a). Typically R-curves have been measured by extending a crack through an externally applied force and measuring the crack length with an optical microscope. Using this technique only crack lengths >50 μm can be observed. Recent studies have allowed for the full R-curve to be measured based on compliance calculations of a very sharp starter notch. In these measurements they found that the initial part of the R-curve is rises very steeply within the first 10 μm (Figure 2.9).[119,120] They also were able to define four distinct stages of toughening for Si_3N_4. Stage I behavior is due to elastic bridges without debonding based on the interfacial strength and aspect ratio of the grains that occurs over the first 10 μm. As the crack opening increases those bridges fracture and Stage II dominates from partially debonded elastic bridges and followed by Stage III with fully debonded frictionally bridges. When the crack opening becomes large enough that all bridging mechanisms reach a steady state, Stage IV behavior is obtained.[117] This progress in observing the R-curve will allow for significant understanding and improvements of the fracture properties of Si_3N_4.

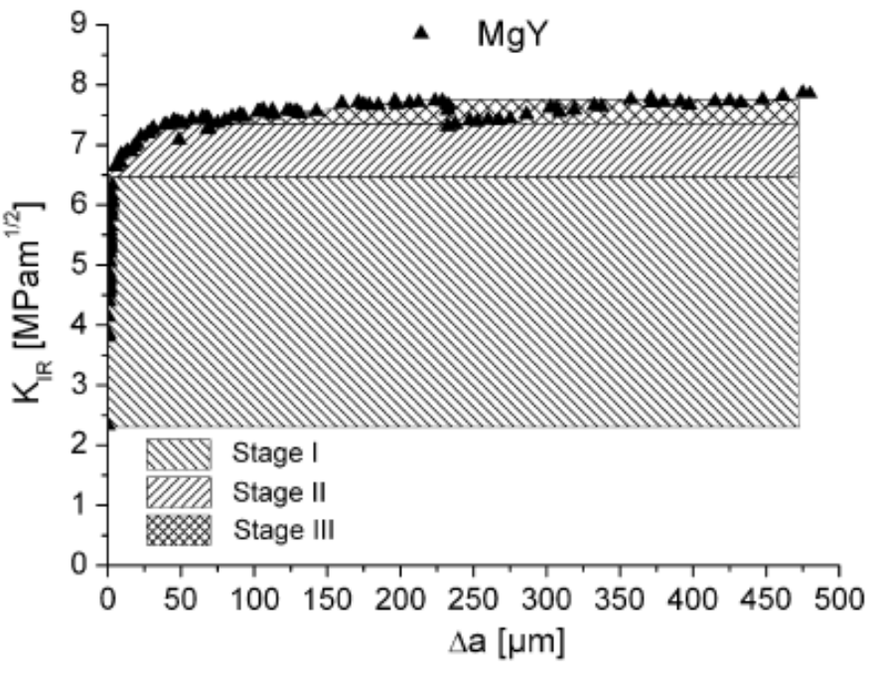

Figure 2.9 Full R-curve calculations for a Si_3N_4 with Mg-Y sintering aids.[117]

The investigations on the fracture toughness of Si_3N_4/SiC nanocomposites are limited. Typically most researchers are interested in the high temperature properties of this materials system for reasons stated in Section 2.2.1. Both improvements[45] and degradation[24,43,46] in toughness has been reported in comparison to monolithic Si_3N_4. The degradation in toughness can be attributed to the SiC particles pinning the anisotropic growth of β-Si_3N_4 grains. The change in grain boundary chemistry can also have an impact on the toughness properties, although no research has been conducted on this topic. There has not been any research into the mechanisms of toughness for these nanocomposite materials.

The high temperature toughness of this material is complicated to understand. At high temperatures there is a change in fracture mechanisms from brittle to visco-plastic when the temperatures are above the glass transition temperature (T_g) of the intergranular glassy phase.[121] It has been shown that the strength degradation of Si_3N_4 at temperatures above the T_g of the intergranular glassy phase is caused by cavitation of the intergranular phase.[122] Improvements in the cavitation creep mechanisms have been shown to improve with the addition of SiC nano-particulates due to the reduction of grain boundary sliding. These same mechanisms can potentially improve the high temperature toughness as well.

2.3 Polymer-Derived Ceramics

Polymer-Derived Ceramics (PDCs) are attractive precursors for high performance silicon based ceramics. They start as silicon based polymers that convert to a ceramic after thermal decomposition at elevated temperatures (>800˚C). This makes them a very unique material in the sense that it is possible to take advantage of polymer processing techniques to form unique shapes and parts to produce a ceramic material. Some applications of PDCs include the production of continuous fibers for ceramic matrix composites (CMCs), microelectromechanical systems (MEMS), high temperature coatings, porous foamed structures for heat shields and

filters.[123] In addition to their advantageous forming techniques, PDCs processing is the only route to produce amorphous Si-C-N, Si-O-C, or Si-C-X-N (X = Al, Ti, B) structures. These structures are able to generate unique nanostructures that give enhanced properties such as creep, electrical conductivity, and oxidation resistance.[124] In addition to the unique non-crystalline structures, these materials can crystallize nano-polycrystalline ceramics at high temperatures (>1500˚C) that would be difficult to produce with traditional ceramic powder processing techniques.

One class of PDC-polysilazanes is able to produce SiCN ceramics that crystallize into Si_3N_4/SiC composites at high temperatures (>1500˚C). This section will primarily discuss preceramic polymers that can or have been used to produce Si_3N_4/SiC nanocomposites.

2.3.1 Preceramic Polymers

There are various types of organosilicon-based polymers that are classified as preceramic polymers for the production of silicon based ceramics by the polymer-to-ceramic transformation process. Figure 2.10 displays the various types of preceramic polymers that have been synthesized. Among them, the families most researched up to date have been: poly(organosilioxanes), poly(organosilazanes) and poly(organocarbosilanes), which yield Si-O-C, Si-C-X-N, and SiC ceramics respectively. The molecular structure of the precursors has a direct influence on the resulting composition and microstructure and therefore its properties.

An ideal preceramic polymer should posses certain key properties in order to be effective for the production of ceramics:[125]

- presence of functional groups in order to gain thermosetting or curing properties
- a sufficiently high molecular weight in order to avoid volatilization of low molecular components
- polymer structure with cages or rings to reduce the volatilization of fragments from backbone cleavage
- suitable rheological properties and solubility for shaping processes.

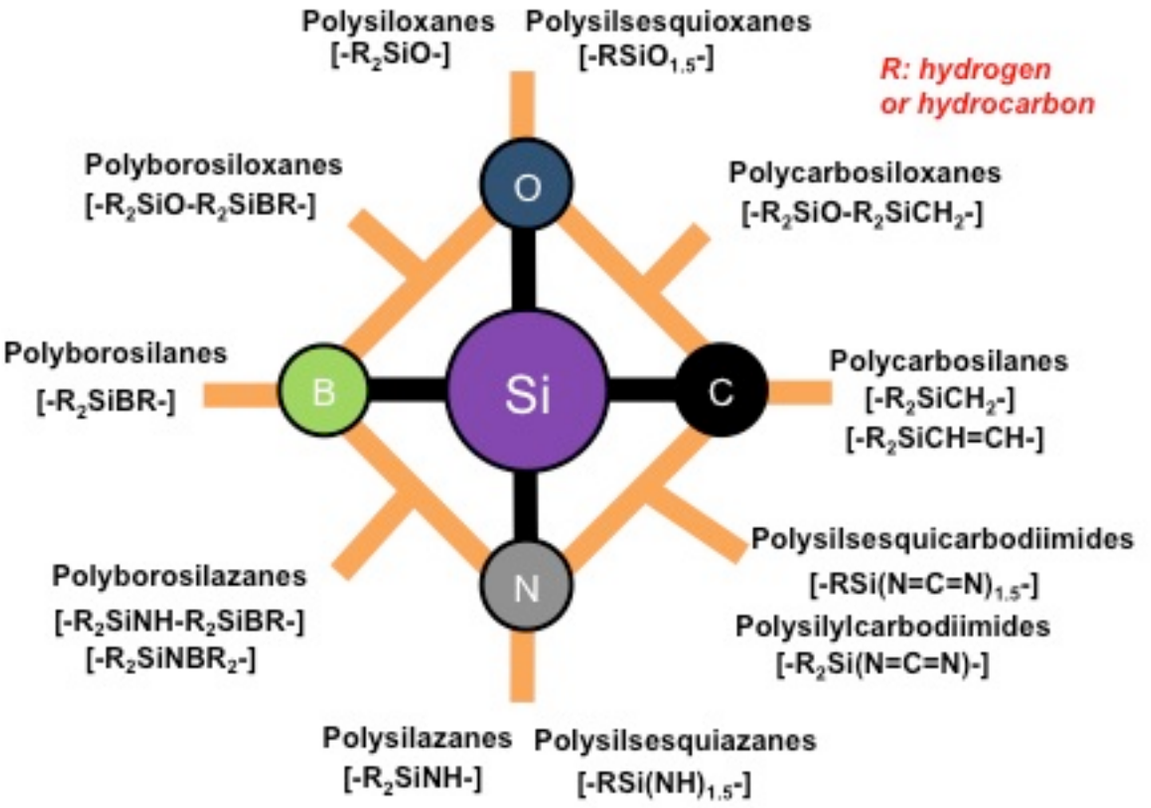

Figure 2.10 Schematic of the classifications of different types of preceramic polymers.[124]

Synthesis of these polymers can become quite complex and require skills of an experienced organic chemist. Early research on these materials was somewhat limited to organic chemists and/or collaborations between engineers and chemists. Research in this field has increased significantly with the availability of affordable commercially available preceramic polymers, which has allowed research groups that are inexperienced with synthetic organic chemistry to progress the research and development of PDCs.

Two United States based companies that produce commercially available precursors for SiC and Si_3N_4 are Starfire Systems Inc. and KiON Defense Technologies, Inc. (KDT) (formerly know as KiON Special Polymers a Clariant Company). These companies produce allyhydridopolycarbosilane (SMP-10 Starfire Systems Inc.) and Ceraset Polyureasilazane (KDT Inc.), which yield SiC and Si-C-N ceramics respectively. Figure 2.11 shows the molecular

structure of theses two materials. These polymers are attractive for this research project, as they will yield SiC (SMP-10) and Si_3N_4/SiC composites (Ceraset).

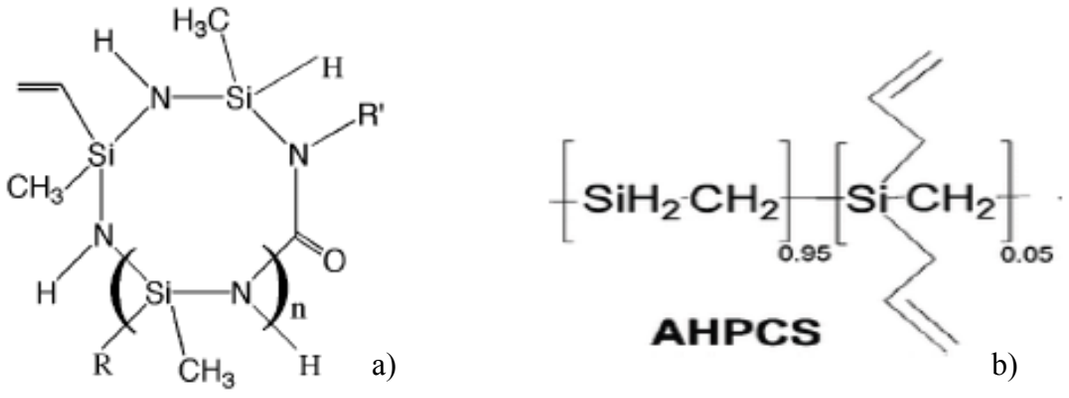

Figure 2.11 Molecular structure of a) Ceraset Polyureasilazane[126] and b) SMP-10[127].

2.3.2 Polymer to Ceramic Transformation

2.3.2.1 Crosslinking

After synthesis of a suitable preceramic polymer there are two major steps for the formation of PDCs: (1) polymer cross-linking at moderated temperatures (100 – 400 ˚C); (2) ceramization process (pyrolysis) of the cross-linked materials at elevated temperatures (800 – 1300 ˚C), which results in an inorganic amorphous materials. If desired crystallization can occur when heat-treated to even higher temperatures (>1500 ˚C)[128], which will be discussed in a later section.

The crosslinking process is a very important step in processing PDCs. During this stage the precursor becomes an organic/inorganic solid material. This transformation prevents the loss of low molecular weight components of the precursor and thus allows for a high ceramic yield during pyrolysis. This stage is also when many forming process occur (e.g. foaming, fiber forming, etc.) These crosslinked polymers will then retain their shape during the ceramization process.

There are a variety of ways to crosslink these polymers, which include: thermally, UV, and the use of chemical agents such as peroxides and catalysts.[125] In polysilazanes there are four major reactions, which can occur during the thermal cross-linking processes: transamination, dehydrocoupling (between Si-H and N-H or Si-H and Si-H groups), vinyl polymerization and hydrosilylation (Figure 2.12).[125]

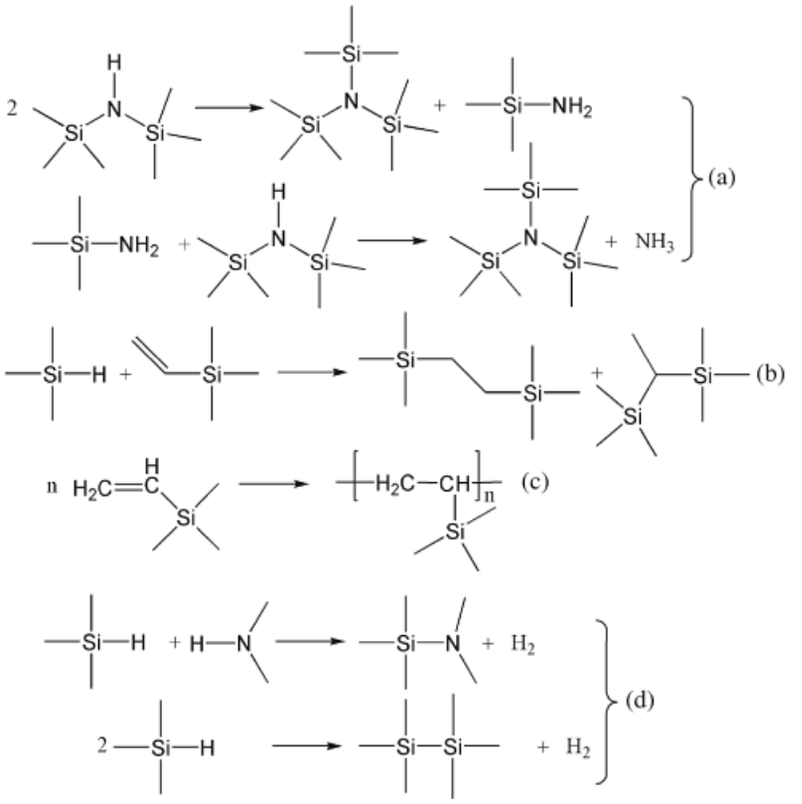

Figure 2.12 Cross-linking reactions of polysilazanes: (a) transamination; (b) hydrosilylation; (c) vinyl polymerization; (d) dehydrocoupling reactions.[125]

In Ceraset, which is a liquid precursor at room temperature, thermal crosslinking starts at temperatures >250 ˚C. Li *et al*. showed a disappearance of vinyl groups confirmed both by FTIR and Raman spectroscopy, which is associated with vinyl polymerization.[126] The liquid precursor also becomes an infusible solid at this point. At temperatures between 250 ˚C and 450 ˚C a reduction in N-H and Si-NH-Si bands can be attributed to transamination reactions. These reactions typically cause mass loss in the form of amines, ammonia or oligomeric silazanes and will result in a decrease in nitrogen content of the final ceramic material. Hydrosilylation

reactions can also occur with the presence of a catalyst and are typically very fast reactions[129,130] and can also lead to high ceramic yield.[130]

In SMP-10 crosslinking is achieved by an opening of the C=C to create a free radial and thus linking with a nearby polymer chain. This can be achieved by UV, e-beam, catalysis, or thermal treatment.[127] In both materials oxidation can play a role in crosslinking mechanisms, however, if oxygen is not ideal (as is the case for this project) then steps should be taken to avoid oxygen incorporation during this step.

2.3.2.2 Ceramization and Structure

Ceramization process of cross-linked ceramic precursors involves a heat treatment at high temperatures (800 – 1200 ˚C) where thermolysis and volatilization of remaining organic groups occurs. After pyrolysis what remains is an amorphous covalent ceramic. This complex process of converting a highly crosslinked organic polymer into an amorphous covalent ceramic is not well understood. Investigations have been performed with a combination of FTIR, TG/MS, NMR and Raman spectroscopy in order to grasp an understanding of what is occurring during this transformation process.[125]

For polycarbosilanes, in the temperature range of 500 – 800 ˚C an endothermic process occurs where the polymer transforms into inorganic material with the elimination of Si-H, Si-CH_3, and Si-CH_2-Si groups. The resulting amorphous structure is seen to have short-range order of SiC_4 groups as well as free carbon depending on the composition.[131]

For Ceraset, once sufficiently crosslinked to allow transamination reactions to be completed, it has been shown by FTIR and Raman that in the temperature range of 600 – 800 ˚C Si-H Si-CH_3, and N-H bonds are eliminated. TG/MS has shown that this is due to reactions between Si-H and N-H bonds (evolution of H_2) and reactions between Si-CH_3 and N-H bonds (evolution of methane).[126] The resulting structure is an amorphous SiCN phase and free carbon.[132] The SiCN phase has been confirmed as a mixed bond tetrahedral of Si-C_x-N_{4-x} via ^{29}Si

MAS-NMR studies.[133] The carbon phase tends to be interconnected graphite networks or can sometimes form graphite particles depending on the composition. An interesting thing to note is that not all polymer-derived SiCN ceramics display the same type of structure after pyrolysis. Polysilycarbodiimides have been shown to have phase separation of the free carbon phase and SiN_4 phase after pyrolysis with no mixed bond tetrahedral.[134] These polymers tend to be carbon rich as compared to polysilazanes.

Besides the starting precursors, reactive atmospheres have been shown to affect the polymer to ceramic transition. TG/MS studies of polycabosilanes and polysilazanes in ammonia (NH_3) atmospheres have shown to cause nucleophilic substitution of Si-H bonds with ammonia and homolytic cleavage of Si-C bonds at higher temperatures lead to substitution with ammonia.[135,136] This causes an increase in nitrogen content to the point where only Si-N bonds remain after pyrolysis.

The process involving the conversion of the high molecular weight preceramic polymers to silicon-based ceramics is quite complex. Investigations are still being conducted to understand the how the initial precursor in conjunction with the polymer ceramic transition affects the final composition and structure and thus its properties. With a greater understanding of this process one can optimize a precursors starting molecular structure in order gain the desired structure and properties needed for specific applications.

2.3.2.3 Crystallization

In the previous section the amorphous structure of SiCN ceramics was briefly discussed. When these materials are heated to very high temperatures (>1500 ˚C) in a nitrogen atmosphere they crystallize to a Si_3N_4/SiC composite.[128] The high resistance to crystallization is unusual compared to amorphous SiN or SiC. These precursors tend to crystallize at approximately 1200 and 800 ˚C respectively. Iwamoto *et al* has shown that this is due to the interconnect SiCN network. In order for Si_3N_4 or SiC to crystallize out of an amorphous phase it must have areas of

SiN_4 or SiC_4 tetrahedrals to form nuclei. As stated in the previous section SiCN PDCs form mix bonded tetrahedrals (SiC_xN_{4-x} where $x<4$) that are forced to rearrange and thus push crystallization to high temperatures.[128] These experimental observations were further verified by thermodynamic calculations by Golczewski *et al*.[137,138]

The amount of Si_3N_4 to SiC that forms is based on the composition of Si-C-N. Figure 2.10 shows a SiCN composition diagram. If the PDC composition falls within the N-SiC-Si_3N_4 triangle the material will crystallize and then go through a carbothermal reduction (Eq. 2.9).

$$C(s) + Si_3N_4(s) \rightarrow SiC + N_2(g) \qquad \text{(Eq. 2.9)}$$

The material will follow the black reaction lines shown in Figure 2.13 until it hits the Si_3N_4 – SiC tie line where all of the excess free carbon will be consumed.[139] It is known that crystallization will occur prior to carbothermal reduction based on a study by Friess *et al*.[140] If the C:Si ratio is >1 then all of the Si_3N_4 will go through a carbothermal reduction resulting in only SiC. If the composition lies within the Si_3N_4 – SiC – Si triangle than excess silicon is left in the system. The red area is the ideal region for this project, as it will produce a Si_3N_4/SiC composite with little carbothermal reactions.

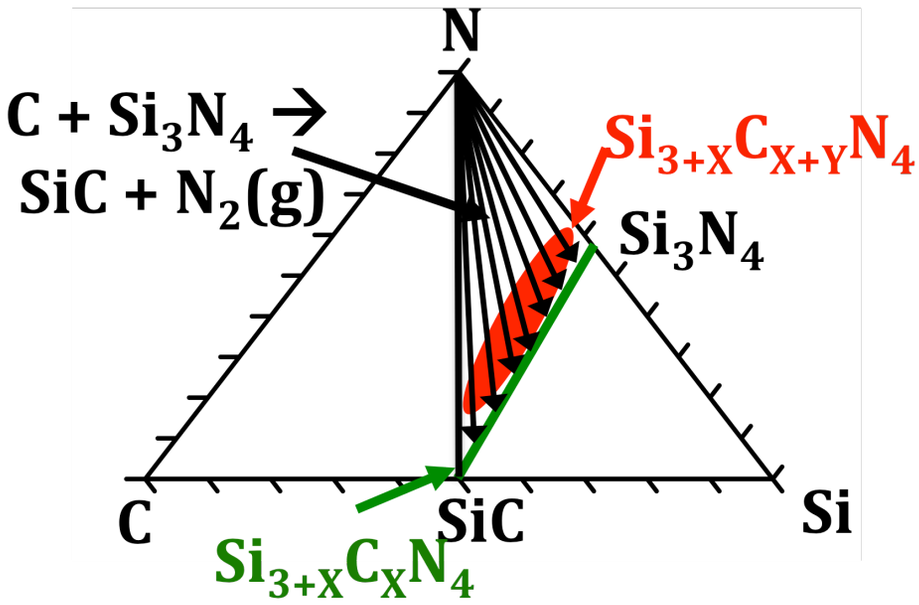

Figure 2.13 Si-C-N compositional diagram.[139]

Chapter 3

Scope of Research

The focus of this research is to optimize Si_3N_4/SiC nanocomposites for high temperature applications. The focus was on developing processing approaches for a wide range of microstructures will be developed with a range of SiC content (0 – 30 vol%) and Si_3N_4 grains of different size (0.5 – 10 μm). The quantitative microstructural images and resulting mechanical properties will be used in follow up research to develop computer simulations of these real microstructures. The simulations will be able to generate a microstructure based on desired mechanical properties. Having established processing protocols, these engineered microstructures can be reproduced and tested to validate the numeric model. The coupled experimental-numeric approach can allow be applied to other high temperature ceramic nanocomposite systems. The benefit of this process would be to significantly reduce the amount of experiments needed to optimize a ceramic microstructure. This could significantly reduce the time needed to establish processing protocols for manufacturing new and innovative structural ceramics and also reduce the costs associated with the large amount of time taken to optimize these ceramic composites.

Polymer-Derived Ceramics (PDCs) were chosen as the processing routes to produce the Si_3N_4/SiC nanocomposites. PDCs are the only processing route known to produce the nano-nano type Si_3N_4/SiC nanocompsites.[22] PDCs are also used for producing Ceramic Matrix Composites (CMCs), which are used in various high temperature applications (e.g. aerospace vehicles, nuclear fuel rods, gas turbine components, etc.) This study also investigated the effect of processing protocols of PDCs on the resulting chemistry and crystalline microstructure. A scientific study of the PDC chemistry and its effect on the resulting microstructures will aid the PDC community in understanding this chemistry-processing-microstructure relationship.

Chapter 4

Materials and Experimental Techniques

4.1 Materials

4.1.1 Preceramic Polymers

To make Si_3N_4/SiC nanocomposites from preceramic polymers it was necessary to obtain a polymer that is commercially available, has high ceramic yield, and can yield a Si_3N_4/SiC composite upon crystallization. Ceraset polyureasilazane produced by KiON Specialty Polymers A Clariant Company (now KiON Defense Technologies Inc. Huntingdon Valley, PA, USA) meets these criteria. Figure 2.11a presents the molecular structure of this polymer.

A precursor to SiC was also sought for this project. By mixing a liquid SiC precursor with a polysilazane it is possible to add additional SiC to the system.[128] Ally hydrido polycarbsilane (SMP-10, Starfire System Inc., Schenectady, NY, USA) is a commercially available liquid precursor to SiC that has a high ceramic yield. Figure 2.11b shows the molecular structure of ally hydrido polycarbosilane (SMP-10).

Both polymers are very air and moisture sensitive. As a result they were stored and handled under gettered nitrogen in a glove box (LABmaster, MBRAUN Inc., Stratham, NH, USA).

4.1.2 Ceramic Materials

Sintering aids were used for the densification of the Si_3N_4/SiC nanocomposite. Lu_2O_3 was chosen as the sintering aid of choice due to the high creep resistance seen for this sintering aid in Si_3N_4.[46] Lu_2O_3 was supplied by Stanford Materials (Irvine, CA, USA) with a 99.99% purity and average particle size of 3.93 μm.

SiC nanoparticles were used as another method of adding SiC to the composite material (Section 5.3). SiC nanoparticles were supplied by MTI Corp. (Richland, CA, USA). The SiC

nanopowder has particle size <30 nm and has a purity of 99+%. According to the manufacturer's XRD results, their product is 85% β-SiC and 15% amorphous.

4.2 Experimental Techniques

4.2.1 Thermal Gravimetric Analysis (TGA)

Thermo gravimetric analysis (TGA) (STA 409C, Netzsch, Selb, Germany) was used for determining the mass loss of the crosslinked polymer powders. This was useful in determining the adequate temperatures for polymer to ceramic conversion. For the TGA experiments, a heating rate of 2 ˚C/min was used to temperatures up to 1400 ˚C in gettered nitrogen or argon environment.

4.2.2 Crystalline Phase Identification: X-Ray Diffraction

X-Ray Diffraction (XRD (Bruker D8 FOCUS, Bruker AXS Inc., Madison, WI, USA) was used to identify and quantify the crystalline phases present in the polymer-derived. A Cu-Kα source with a 40kV accelerating voltage and 40mA was used for all the samples. Initially for general phase identification a scanning range of 10 to 90˚ 2θ at a step size of 0.02˚ 2θ and a dwell time of 1 second/step was used. For samples where phase quantification was conducted, a scanning range of 20 to 65˚ 2θ at a step size of 0.02˚ 2θ was used. A curved graphite monochromator (Cu-Monochromator, Bruker AXS Inc. Madison, WI, USA) with a diffraction angle of 26.4˚ 2θ was used to increase the resolution of the diffraction pattern for phase quantification.

Phase quantification was determined by the "Mean-Normalized-Intensity" (MNI) technique. This method has been shown to be a suitable technique for quantification of Si_3N_4/SiC composites.[141,142] The (MNI) method is based on selecting a few well-resolved peaks and then calculating the angle and structure related contributions to the integrated peak intensity.

Thus, the unknown factor in the measured intensity is directly related to the volume fraction of the component phase. The Bragg peak intensity of peak *j* and phase *i* in the Bragg-Brentano diffraction pattern can be expressed as

$$I_{ij} = \frac{C_0 (mL_p |F|^2)_{ij} \left(v_i / V_i^2 \right)}{2\mu} \qquad \text{(Eq. 4.1)}$$

where C_0 is an instrument constant, m is the multiplicity factor, L_p is the Lorentz-polarization factor, $|F|$ is the structure amplitude, v_i the volume fraction of phase i in the mixture, V_i the unit-cell of phase *i,* and μ the linear attenuation coefficient of the mixture. The integrated intensities then need to be converted to normalized intensities (I_{ij}^n) according to

$$I_{ij}^n = \frac{I_{ij}}{R_{ij}} \qquad \text{(Eq. 4.2)}$$

where

$$R_{ij} = \frac{(mL_p |F|^2)_{ij}}{V_i^2} \qquad \text{(Eq. 4.3)}$$

is the normalizing factor for line *j* of phase *i*. The volume fraction of phase *i* can than be calculated (assuming no amorphous content) by

$$v_i = \frac{\bar{I}_i^n}{\sum_p \bar{I}_p^n}. \qquad \text{(Eq. 4.4)}$$

The normalizing factors for α-Si_3N_4, β-Si_3N_4, and β-SiC are given in

Table 4.1.

Table 4.1 Normalizing factors, R_{ij}, used for MNI calculations.[141,142]

Phase	2θ (Cu-Kα)	hkl	Rij
β-SiC	35.7	111	37
	41.4	200	6.7
	60.0	220	17.1
β-Si3N4	23.4	110	4.2
	27.1	200	11.9
	33.7	101	12.4
	36.1	210	11.4
α-Si3N4	20.7	101	8.6
	23.0	110	3.7
	26.5	200	2.7
	31.1	201	8.4
	34.6	102	7.9
	35.3	210	7.9
	43.6	301	3.6

Integrated intensities were determined by profile fitting using Jade v.8.0 (Materials Data Inc., USA) software. A split Pearson-IV function was applied to the diffraction pattern measurements.

Phase analysis was performed on sintered specimens using the same parameters described above, except using a Rigaku ULTIMA IV XRD instrument.

4.2.3 Chemical Analysis: Elemental Analysis, FTIR, Raman Spectroscopy

Elemental analysis of pyrolyzed powder samples was conducted using combustion (LECO EC12 carbon determinator) for C and inert gas fusion (Leco TC436 N/O determinator) for N and O. The analysis was performed in collaboration with the Ceramics Institute of Inorganic Chemistry, Slovak Academy of Sciences, in Bratislava, Slovakia.

FTIR (Vertex 70, Bruker AXS Inc., Madison, WI, USA) measurements were performed on Ceraset that was crosslinked at 400 ˚C and milled into a fine powder. Measurements were also taken on crosslinked and powder samples heated in 10%NH_3/Ar atmosphere at 550 ˚C for 0, 1, 2, 3 and 5 hours. The powder samples were mixed with KBr (1:100 sample:KBr weight ratio) and pressed into a hand press sample holder. Samples were scanned in transmission mode from 4000 – 400 cm^{-1} at a step size of 4 cm^{-1}.

Pyrolyzed powder pellets crystallized at 1650, 1750 and 1850 ˚C in a nitrogen atmosphere were hand polished to 1600 grit SiC paper for Raman Spectroscopy. Raman Spectroscopy (Renishaw inVia Raman Microscopy, Renishaw Inc., Hoffman Estates, Il, USA) was performed at the Nanotech User Facility (NTUF) at the University of Washington. A 785 nm laser excitation source was used to cover a scan range of 3200 – 100 cm^{-1}.

4.2.4 Physical Characterization: Particle Size, Density

Particle size analysis (*Particia* LA-950v2 Particle Size Analyzer, Horiba Scientific, Edison, NJ, USA) was performed on both milled crosslinked and pyrolyzed powder. Crosslinked and milled powders were prepared by sonicating in isopropyl alcohol to disperse any agglomerates. Pyrolyzed powders were prepared by adding the particles to DI water that contained a few drops of a polyelectrolyte (Darvan-C) to help disperse the particles for analysis.

Archimedes method was used for density measurements of sintered Si_3N_4/SiC composites. ASTM C373-88 was used for measuring and calculating the density of the composites.

4.2.5 Microstructural Characterization

Scanning Electron Microscopy (SEM)

Field Emission (FE)-SEM was used to observe microstructural features of dense Si_3N_4/SiC nanocomposites. JSM-7000F (JEOL-USA, Inc. Peabody, MA, USA) was used on Preliminary Consolidation studies (Section 6.1) samples in both secondary (SEI) and backscattered (BEI) electron imaging modes. The samples were cross-sectioned with a low speed diamond saw and mounted in a resin. The samples were then ground with diamond bonded pads (70, 15 and 6 μm) and then polished on polishing pads with 3, 1, and 0.1 μm diamond suspensions. After polishing some samples were removed from the epoxy mounts and plasma etched in a CF_4/10%O_2 atmosphere. This process causes the Si_3N_4 to etch at a much faster rate than the SiC and glassy grain boundary phases leading to a phase contrast in SEI mode.

Hitachi S4800 (Hitachi High Technologies America, Inc.) FE-SEM was used for microstructural characterization of hot pressed (Section 6.2) and field assisted sintered (Section 6.3) samples using both SEI and BEI imaging. Sample preparation procedures were the same as stated above.

X-ray Energy Dispersive Spectroscopy (EDS) mapping was conducted using a JSM-7100F (JEOL-USA, Inc. Peabody, MA, USA) FE-SEM equipped with a JEOL 129eV resolution silicon drift detector (SDD). Hot pressed samples were prepared using the Hitachi nanoDUE'T double beam microscope – NB5000 equipped with a Focused Ion Beam (FIB) with a Ga^+ ion source. Samples were approximately 100 nm thick. The FIB samples were advantageous over bulk samples in that it limits the interaction volume of the measured X-rays.

Transmission Electron Microscopy (TEM)

TEM investigations were conducted on the hot pressed (Section 6.2) and field assisted sintered (Section 6.3) samples. Samples were prepared by slicing a thin cross section (~0.5 mm thick) followed by grinding and polishing until the samples was ~100 μm thick. The samples were then dimpled to ~10 μm followed by Argon ion milling at an energy of 4keV and an angle of 4˚ until the center of the sample was perforated. The edges of the perforated samples were

electron transparent and used for TEM analysis. A Phillips Technai FEG-STEM with 200keV emission source and equipped with EDS detector and a Gatan Image Filter (GIF) camera for Energy Electron Loss Spectroscopy and Energy Filtered TEM (EFTEM) was used for analyzing prepared samples. A FEI Technai 30 TEM with 300keV emission source was used for High Resolution TEM (HRTEM) imaging.

4.2.6 Mechanical Testing: Hardness, Fracture Toughness

Hardness testing was performed on the hot pressed (Section 6.2) and field assisted sintered (Section 6.3) samples. Samples where cross-sectioned and polished similar to the procedures for SEM sample preparation stated above. Vickers indenter was used to indent samples at 9.81 N according to ASTM 1307-08. Hardness values (*HV*) were calculated using:

$$HV = 0.0018544\left(P/d^2\right) \qquad \text{(Eq. 4.5)}$$

where P is the indentation load and d is the average of the measured diagonals of each indent.[143] An average *HV* value was calculated for ~10 indents per samples.

Fracture toughness testing was performed on the hot pressed (Section 6.2) samples using the Single Edge V-Notch Beam (SEVNB).[144] Bend bar specimens with dimensions of 3 mm x 4 mm x 25 mm were machined from the hot pressed samples. A starter notch was first introduced using a 0.38 mm thick diamond blade perpendicular to the 3 mm face. A razor blade with diamond paste was then used to make a sharp V-Notch. A home built automated system was used with the razor blade to make the sharp V-Notch (Figure 4.1). The depth of the V-Notch was ~2.6 mm with a root notch radius of ~6 μm. Figure 4.2 shows an example of a specimen prepared. The specimens were tested in 4-pt. flexure with loading and supporting spans of 10 mm and 20 mm respectively. Specimens were loaded at a rate of 0.05 mm/min until failure. The

maximum value recorder was used for K_{IC} calculations. Two specimens per series were tested and average reported. The K_{IC} values were computed using the formula[144]

$$K_{IC} = \frac{3P_f(S_1 - S_2)\alpha^{1/2}Y}{2BW^{3/2}(1-\alpha)^{3/2}} \quad \text{(Eq. 4.6)}$$

$$Y = 1.9877 - 1.326\alpha - \left[\left(3.49 - 0.68\alpha + 1.35\alpha^2\right)\frac{\alpha(1-\alpha)}{(1+\alpha)^2}\right] \quad \text{(Eq. 4.7)}$$

where P_f was the maximum load, S_1 and S_2 are the supporting and loading spans respectively, $\alpha = a/W$ where a is the length of the notch and W is depth, B is the width of the specimen and Y is a geometric facture based on the geometry of the specimen given by Eq. 4.7.

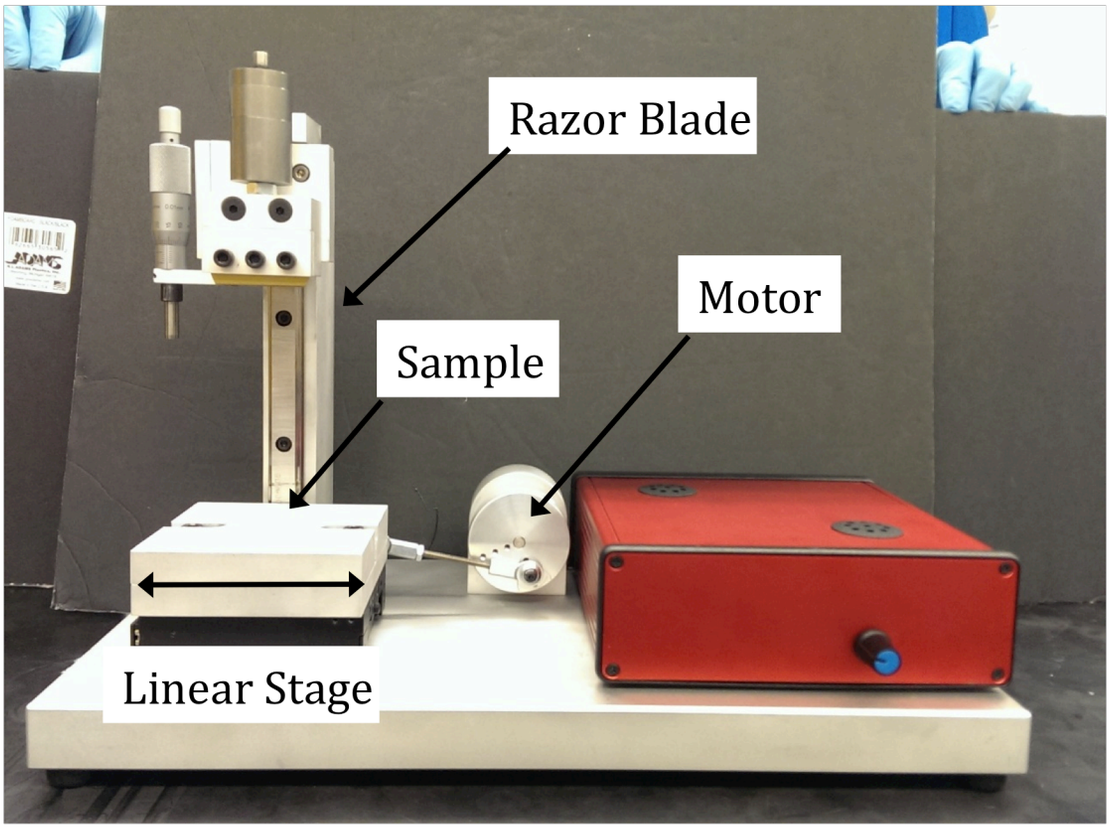

Figure 4.1 Apparatus for make SEVNB samples.

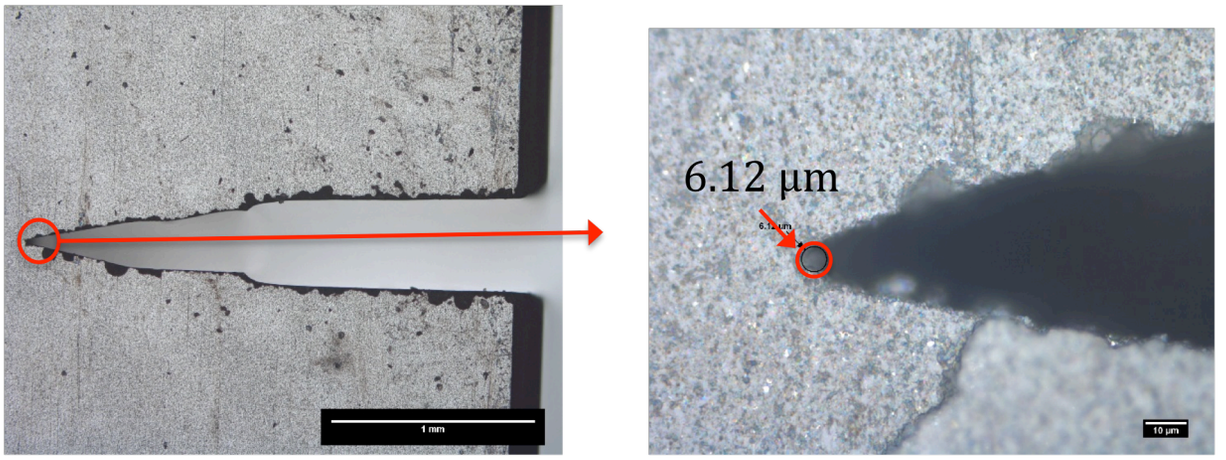

Figure 4.2 Example of SEVNB prepared using the razor blade apparatus.

4.2.7 Dilatometer Testing

Netzsch Dil 402C dilatometer was used to measure the coefficient of thermal expansion (CTE) as a function of temperature for two hot pressed specimens (Section 6.2). Sample dimensions of 3 mm x 4 mm x 25 mm were used in the dilatometer and heated at a rate of 1.5 ˚C/min to 1400 ˚C. Expansion data was fitted with a 9^{th} order polynomial and the first derivative was taken to show the CTE data vs. temperature.

Chapter 5

Results on the Processing and Characterization Controlled Volume Fraction Si_3N_4/SiC from Preceramic Polymers

5.1 Processing Procedure for Controlled Volume Fraction Si_3N_4/SiC from Preceramic Polymers

The first stage of this project was to develop processing protocols of preceramic polymers that results in controlled volume fraction Si_3N_4/SiC composites. A number of techniques were explored to either control the composition of the resulting polymer derived SiCN ceramic or the use of ceramic additives (i.e.. SiC particles) which will be outlined later in this section. Controlling the composition of the SiCN ceramic would have direct control of the resulting Si_3N_4/SiC composite as outlined in Section 2.3.2 and would provide a single source powder where both the Si_3N_4 and SiC grains would grow *in-situ*.

The process flow diagram displayed in Figure 5.1 was used for an exploratory trial and error approach to develop processing protocols to make ceramic powders from preceramic polymers with controlled volume fraction Si_3N_4/SiC. Three approaches were taken to obtain this goal, which will be outlined in this section.

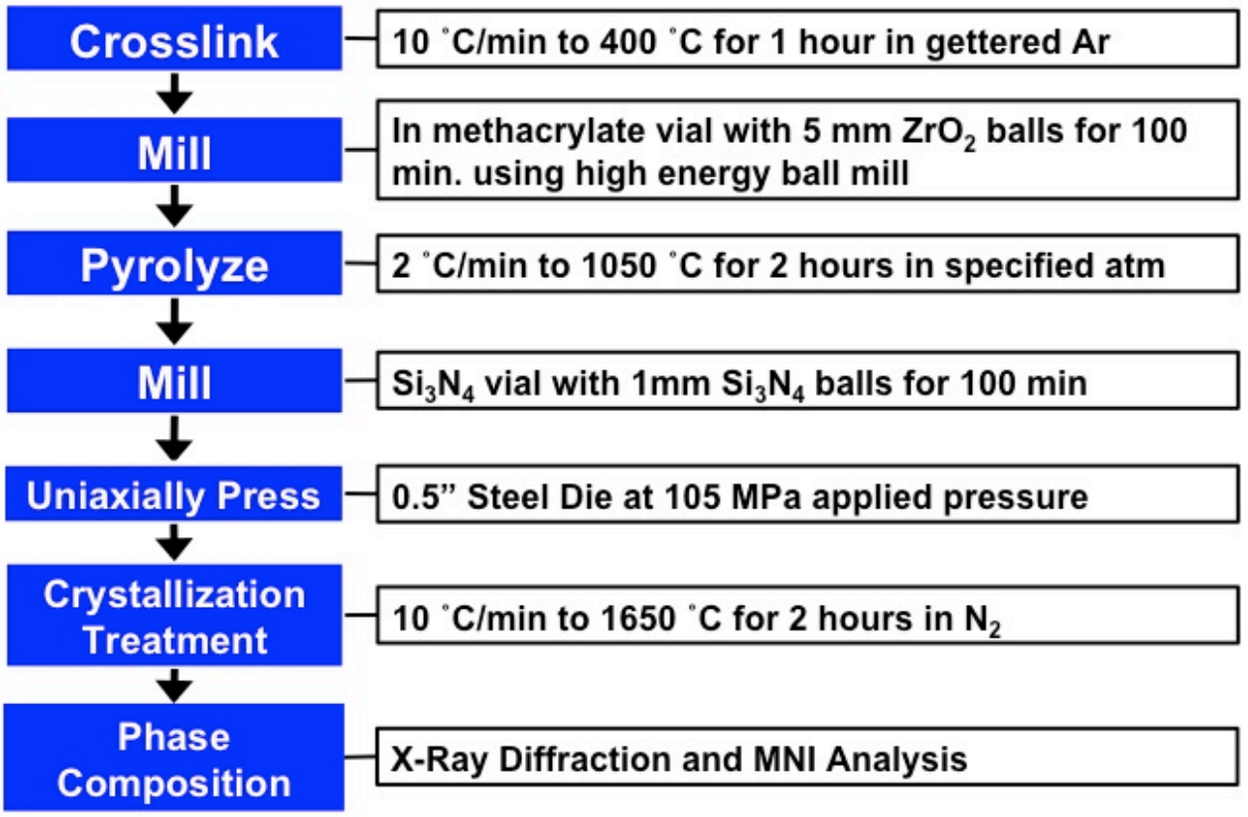

Figure 5.1 Flow chart for processing and characterization of controlled volume fraction SiC from polymer derived ceramics.

5.2 Mixing Preceramic Polymers

Ceraset (polyureasilazane) and SMP-10 (allyl hydrido polycarbosilane) were chosen as preceramic polymers to explore for this project as outlined in Section 4.1.1. According to the literature Ceraset yields a SiCN PDC, which crystallizes into a Si_3N_4/SiC composite at temperatures >1500 ˚C.[21,126] SMP-10 yields SiC upon crystallization. Mixing the two polymers at various ratios was postulated to produce Si_3N_4/SiC composites of controlled stoichiometry. The two polymers have low viscosities and are visually miscible when mixed together. Ceraset and SMP-10 were mixed at weight ratios of 90:10, 80:20, 60:40, 50:50, 40:60, and 20:80 Ceraset:SMP-10.

TGA of crosslinked and milled Ceraset and SMP-10 was performed in order to determine optimal pyrolysis temperatures. TGA results of crosslinked Ceraset and SMP-10 powders are

shown in Figure 5.2. Both show no further mass loss after 800 ˚C. For all further experiments a heating rate of 2˚C/min to 1050 ˚C for 2 hours was chosen to ensure that the polymers were fully decomposed and converted to ceramics.

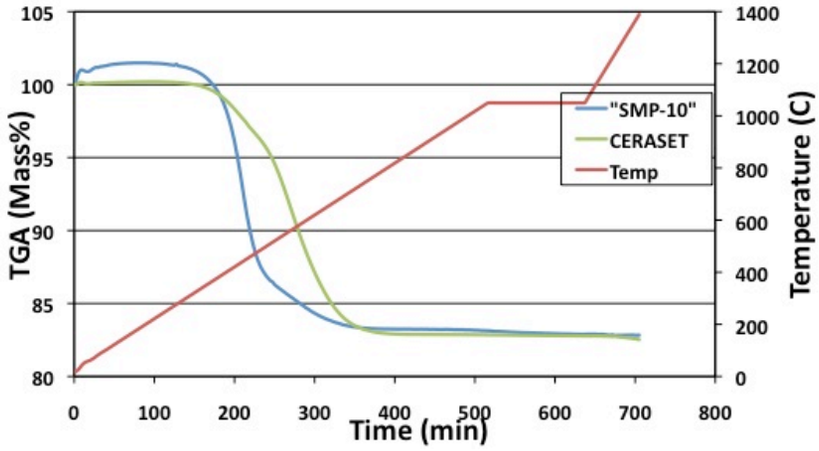

Figure 5.2 TGA results of crosslinked SMP-10 and Ceraset powders under gettered Argon.

XRD results (Figure 5.3) reveals that the Ceraset and SMP-10 polymers remain amorphous at 1050 ˚C. When heated treated to 1650 ˚C in nitrogen Ceraset yields a α-Si_3N_4/β-SiC composite and SMP-10 yields β-SiC. The mixed material (60:40 Ceraset:SMP-10 weight ratio) was heat treated in gettered nitrogen and still remains amorphous at 1050 ˚C. At 1650 ˚C 2H-SiC precipitates out of the PDC. This phase is clearly identified over the other common polymorphs of SiC (6H and 4H) by the 50° 2θ peak. This peak is only associated with 2H-SiC whereas the other identified 2H peaks overlap with 6H(α) and 4H-SiC. At a polymer weight ratio of 60:40 Ceraset:SMP-10, there is no observable diffraction peaks associated with Si_3N_4. Figure 5.4 shows XRD results of Ceraset, SMP-10 and all of the mixes. The 20:80, 40:60, and 60:40 (Ceraset:SMP-10) mixes all show similar XRD patterns with the emergence of the 2H-SiC phase and no observable Si_3N_4 peaks. In the 80:20 and 90:10 mixes β-Si_3N_4 forms but α-Si_3N_4 is not present. It is likely that the PDC composition has a C:Si ratio >1 for the 60:40, 40:60, and 20:80 mixes because only SiC is observable in their diffraction patterns (see Figure 2.13). Since the exact compositions of Ceraset and SMP-10 are proprietary, the exact C:Si ratio is not known.

Figure 5.4 also shows that when Ceraset is pyrolyzed under NH_3 atmosphere, it yields only α-Si_3N_4 with no detectable SiC. The same results occur with SMP-10 (Figure 5.4).

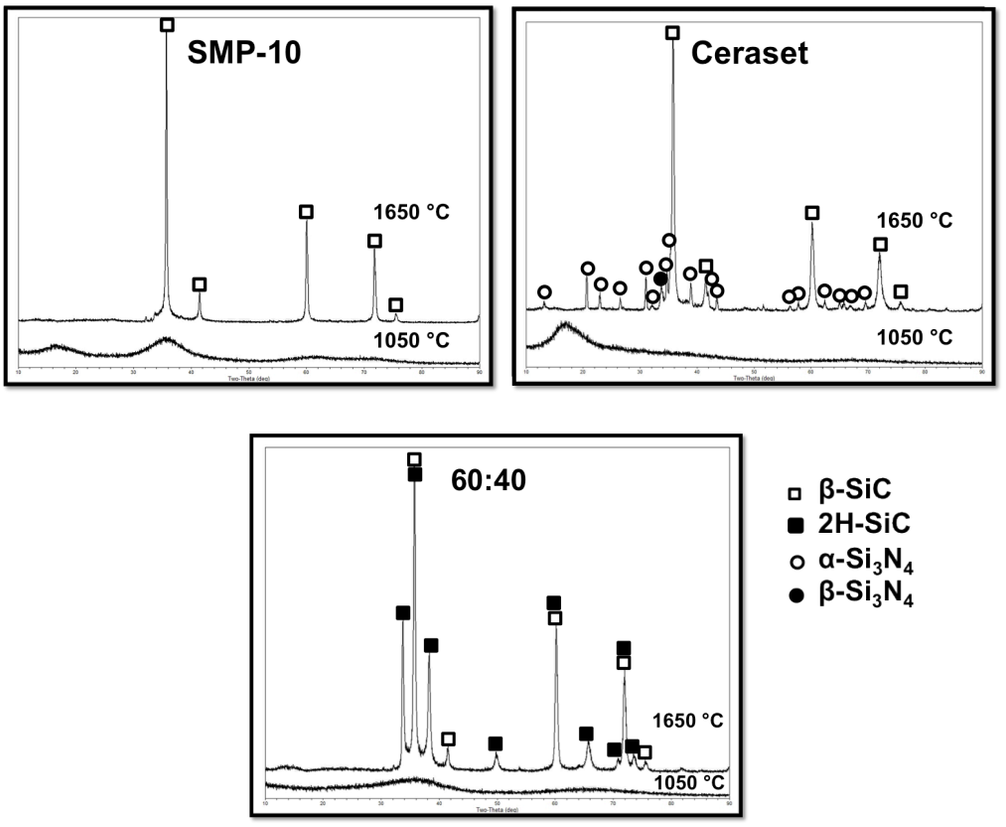

Figure 5.3 XRD of SMP-10, Ceraset and the 60:40 mix heat treated to 1050 and 1650 ˚C under gettered nitrogen.

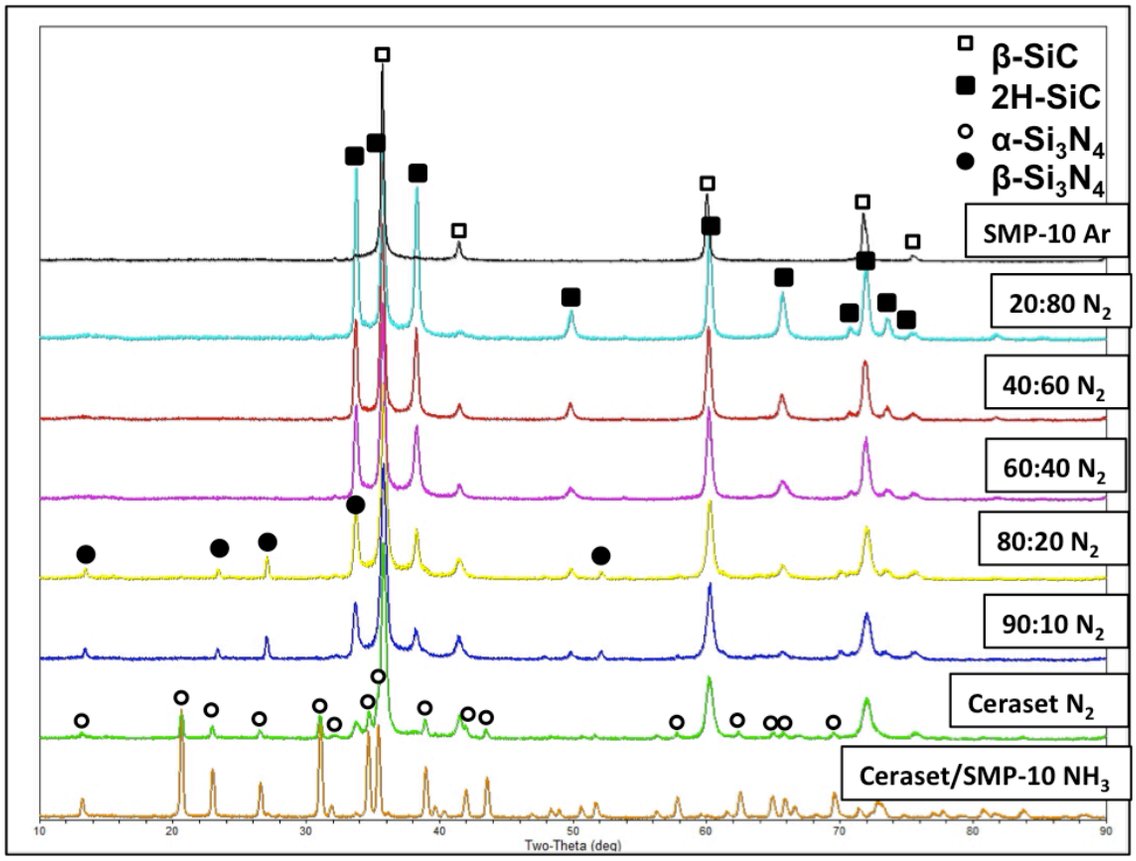

Figure 5.4 XRD of different mixes of SMP-10 and Ceraset pyrolyzed under gettered N_2 and Ceraset pyrolyzed under NH_3.

Elemental analysis for the Ceraset pyrolyzed in NH_3, the 80:20, 50:50, 20:80 mixes pyrolyzed in nitrogen and SMP-10 pyrolyzed in argon atmosphere are shown in

Table 5.1. All of the samples were pyrolyzed at 1050 ˚C. The results are plotted on a Si-C-N (oxygen is neglected) compositional diagram in *Figure 5.5*. The 20:80 mix has a C:Si ratio >1, which correlates to the unobserved Si_3N_4 in the XRD pattern. The 80:20 mixture also shows the expected results where the C:Si ratio is <1, which correlates with the observed Si_3N_4. However, the 50:50 mix does not follow this trend. The C:Si ratio for the 50:50 mix is <1 but there is no observed Si_3N_4. Based on its composition, the 50:50 mix should have similar amounts of Si_3N_4 as the 80:20 mix. The explanation for this behavior is not clear.

Table 5.1 Atomic % and elemental formula of pyrolyzed PDCs (for mixes the ratios are Ceraset:SMP-10 by weight) pyrolyzed at 1050 ˚C.

Sample ID	**Si**	**C**	**N**	**O**	**Formula normalized to Si**
20:80 N_2	42.81	45.20	6.62	5.37	$Si_{1.00}C_{1.05}N_{0.15}O_{0.13}$
50:50 N_2	44.29	35.42	16.68	3.61	$Si_{1.00}C_{0.80}N_{0.38}O_{0.08}$
80:20 N_2	40.71	32.20	24.25	2.83	$Si_{1.00}C_{0.79}N_{0.59}O_{0.07}$
SMP-10 Ar	45.62	48.54	0.11	5.73	$Si_{1.00}C_{1.06}N_{0.002}O_{0.13}$
Ceraset_NH_3	42.56	1.39	51.46	4.59	$Si_{1.00}C_{0.03}N_{1.21}O_{0.11}$

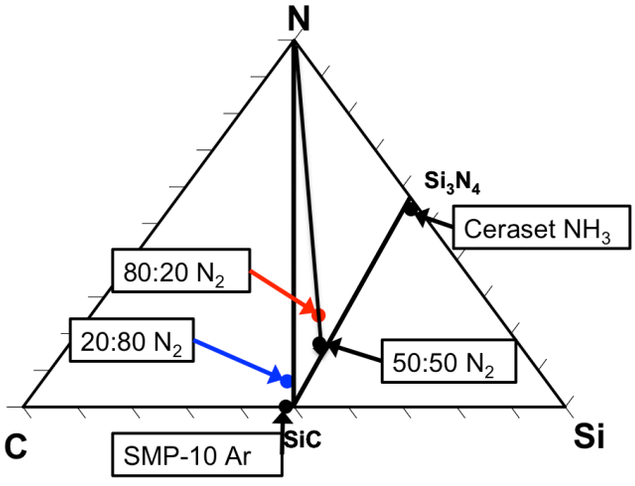

Figure 5.5 PDC composition plotted on a Si-C-N ternary diagram (data from Table 5.1).

The results show it is possible to tailor the volume fraction of SiC:Si_3N_4 of Ceraset by just mixing different amounts of SMP-10 with the Ceraset. This process only allows the addition of SiC, therefore, the amount of Si_3N_4 is limited to the amount produced from the Ceraset

polymer. From quantitative XRD, Ceraset pyrolyzed pyrolyzed at 1050 ˚C and crystallized at 1650 ˚C under nitrogen consists of ~75 volume % SiC. This research project is interested in tailoring the volume fraction of SiC between 0 – 30%. Pure Si_3N_4 can be obtained by pyrolysis of Ceraset under NH_3 atmosphere. It is possible to tailor the nitrogen content and thus the volume fraction of SiC through a controlled NH_3 pyrolysis. This process will be discussed in Section 5.4. Previous studies have shown it is possible to tailor the carbon content of the PDCs with controlled ammonia pyrolysis.[62,64]

5.3 Addition of SiC nanoparticles

As stated in the previous section, when Ceraset is pyrolyzed in a 100%NH_3 atmosphere, it yields only Si_3N_4. Another approach to obtaining controlled volume fraction SiC is by adding SiC nanoparticles directly to the liquid polymer prior to crosslinking, and then pyrolyzing in a 100%NH_3 atmosphere. This would be an easy way to extrinsically add SiC to the composite system.

SiC nanoparticles were added to Ceraset at a 7.75 and 14.38 wt. % in order to yield 10 and 20 vol% SiC. The weight% additions were based on the 75 mass% yield of Ceraset after crosslinking and pyrolysis.[126] The XRD results of the SiC nanoparticle additions to Ceraset pyrolyzed at 1050 ˚C under NH_3 and crystallized at 1650 ˚C under nitrogen are shown in Figure 5.6. These results show the presence of both α-Si_3N_4 and a shoulder peak at 35.7 ˚2θ where β-SiC exists. Quantitative XRD analysis yielded volume fraction SiC values of 6.4 and 10 for the 7.75 and 14.38wt% samples respectively. It was expected that the 7.75 and 14.38 wt% addition samples would yield 10 and 20 vol% SiC. The reason this does not correlate with the quantitative results is because the SiC nanoparticles were 15% amorphous as mentioned by the supplier. This information is pertinent due to the fact that quantitative XRD techniques assume that all materials are crystalline. It is safe to assume that these materials yield 10 and 20 vol% SiC based on the added amount of SiC weight addition calculations.

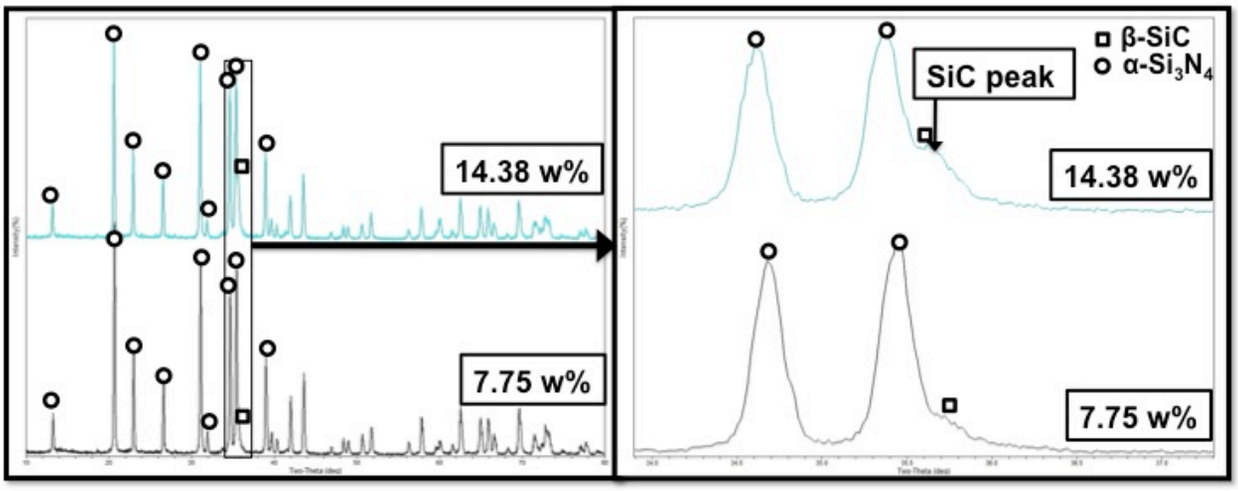

Figure 5.6 XRD results of SiC nanoparticle additions to Ceraset pyrolyzed under NH_3 atmosphere at 1050 ˚C and crystallized at 1650 ˚C under nitrogen.

Si_3N_4/SiC composites with controlled volume fractions of SiC can now be processed through the addition of SiC nanoparticles to Ceraset and pyrolyzed under NH_3 atmosphere. However, the size of SiC cannot be smaller than the added particles and its location cannot be controlled. Thus, there is interest in producing controlled volume fraction SiC from a single source PDC, where both the Si_3N_4 and SiC grains grow *in situ* during the sintering stages. The next section describes an alternative approach to address this problem.

5.4 Controlled Ammonia Pyrolysis

5.4.1 Development of Processing Protocols

According to the literature it is possible to control the carbon content in a resulting polysilazane derived ceramic by switching the atmospheric gas from argon to ammonia at specific temperatures and times.[139] Following up on Galusek *et al.* results, they stated that pyrolysis under a 100% NH_3 atmosphere or a 10% NH_3 (Argon balance) atmosphere will yield a 100% Si_3N_4 ceramic. This experiment was repeated utilizing Ceraset. Figure 5.7 shows the results of this experiment. Unlike Galusek *et. al.*[139], the quantitative XRD results show that Ceraset produces a 25v% SiC composite under a 10%NH_3 atmosphere. This is likely due to high

carbon content of Ceraset (polyureasilazane) compared to the poly(hydridomethyl)silazane used by Galusek *et al*, which has a much lower carbon content.[139] The high carbon content of Ceraset gives a broader range to tailor the stoichiometry of the resulting PDC.

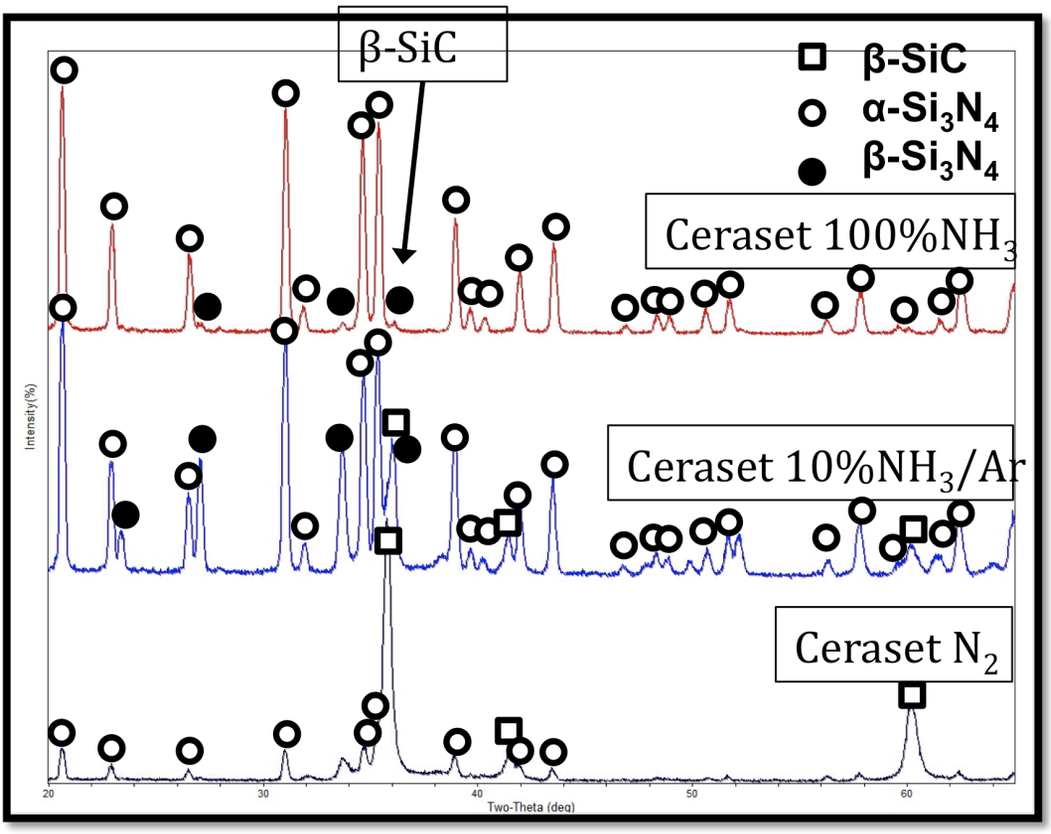

Figure 5.7 XRD of Ceraset pyrolyzed under N_2 (bottom), 10%NH_3/Ar *(middle), and 100%NH_3 (top) atmosphere at 1050 ˚C and crystallized at 1650 ˚C under nitrogen.*

During pyrolysis in an ammonia atmosphere, NH_3 reacts with the crosslinked polymer through a substitution reaction. The current theory based on TG-MS results of polysilazanes heated in an ammonia atmosphere states that there is nucleophilic substitution in the case of Si-H bonds, whereas homolytic cleavages of Si-C bonds occur in the case of carbon substituents.[136] The substitution process can be controlled by switching the atmospheric gas from NH_3 to Argon, thus essentially quenching the reaction. The next set of experiments utilizes this controlled NH_3 pyrolysis. An example of the heating profile is displayed in Figure 5.8, where the gas is switched from NH_3 to Argon at specific temperatures (T_S) and specific times (t_S). After there

heat treatments, all powders were heat treated at 1650 ˚C in nitrogen atmosphere to crystallize the ceramic.

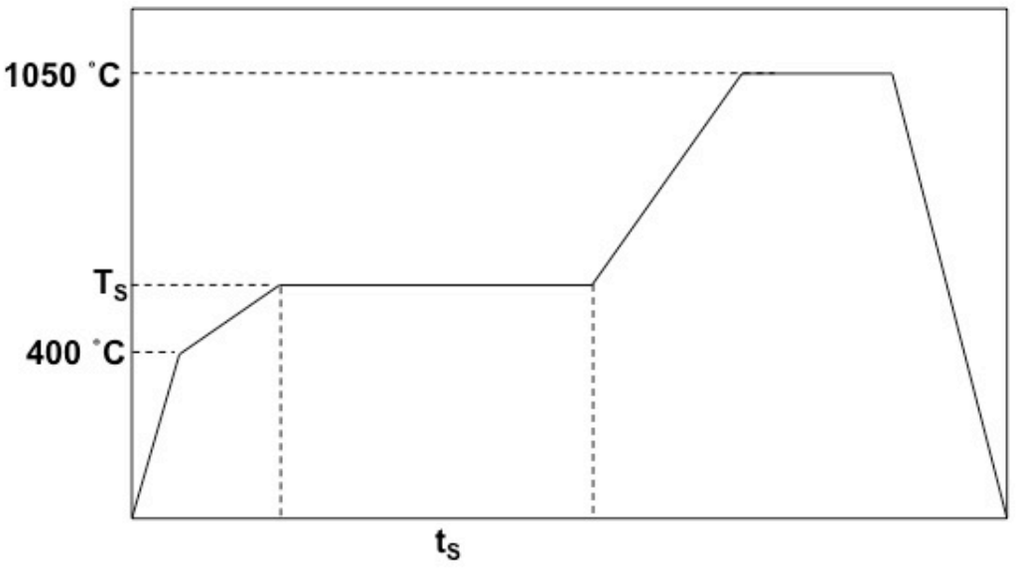

Figure 5.8 Heating profile for controlled NH_3 pyrolysis where the gas is switched from NH_3 to Argon at specific temperatures (T_S) and times (t_S).

For consistency each experiment was conducted using 5 g of crosslinked Ceraset powder. The crosslinked powder was pyrolyzed in a 100% NH_3 atmosphere where the atmosphere was switched to Argon at T_S of 560, 580, 600 and 620 ˚C with no holding times (i.e. $t_s = 0$). Figure 5.9 shows the resulting volume fraction SiC of the crystallized powders. SiC content of PDCs changed drastically from 32v% at T_S = 560 ˚C to 0v% at T_S = 600 ˚C. This is a very narrow range to tailor the SiC content. The temperature sensitivity can be displayed visually in Figure 5.10, which shows a 100% NH_3 600˚C pyrolysis run when the tube furnaces had a temperature gradient prior to experiments conducted in Figure 5.9. The stoichiometric difference is visually seen with high carbon content as black and low carbon content as white. The next set of experiments varied switching time (t_S) with a constant switching temperature (T_S).

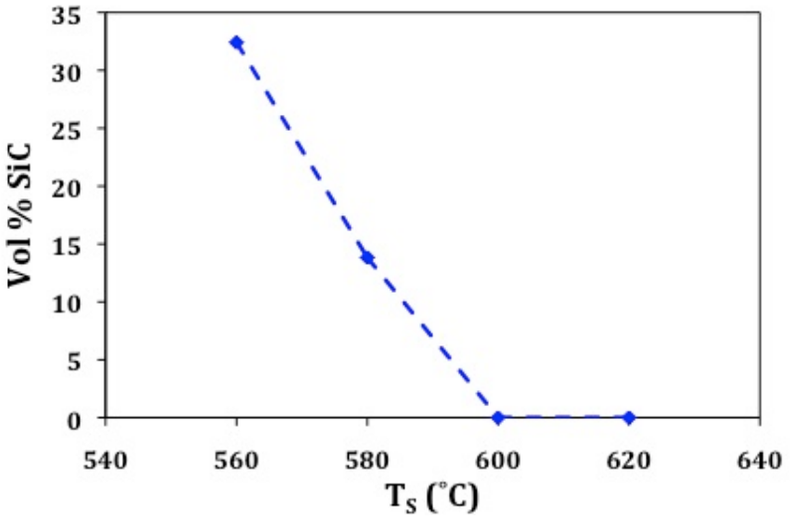

Figure 5.9 Volume fraction SiC as a function of the switching temperature (T_S) where the atmosphere was switched from 100% NH_3 to Argon.

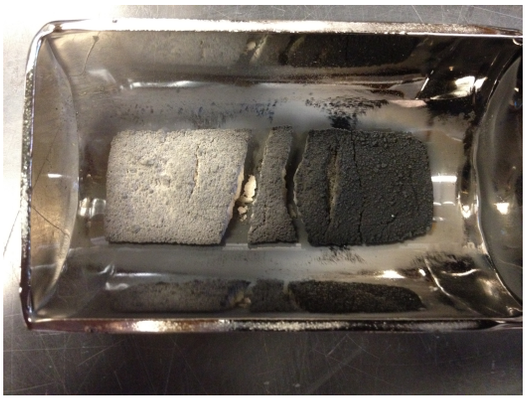

Figure 5.10 Image of 100%$NH_3$600˚C pyrolysis when the tube furnace had a measurable temperature variation.

A series of time experiments were explored to determine optimal processing protocols to produce controlled volume fraction SiC samples. First crosslinked Ceraset powders were held at 570 ˚C under both 100% NH_3 and 10% NH_3 atmospheres for times of 10 minutes, 1 and 5 hours where the gas is then switched to Argon. These results are displayed in Figure 5.11. The 570 ˚C samples showed that time can also vary the resulting SiC content of the composites, with the highest SiC content achieved being 21vol% with the 10% $NH_3$570˚C_1h sample. Our goal is to produce SiC content between 0 – 30 vol% SiC. By reducing the switching temperature (T_S) to

550 ˚C in a 10%NH_3 atmosphere and switching times (t_S) of 1, 1.33, 1.5, 2, 3, and 5 h it was possible to achieve this goal as seen in Figure 5.11.

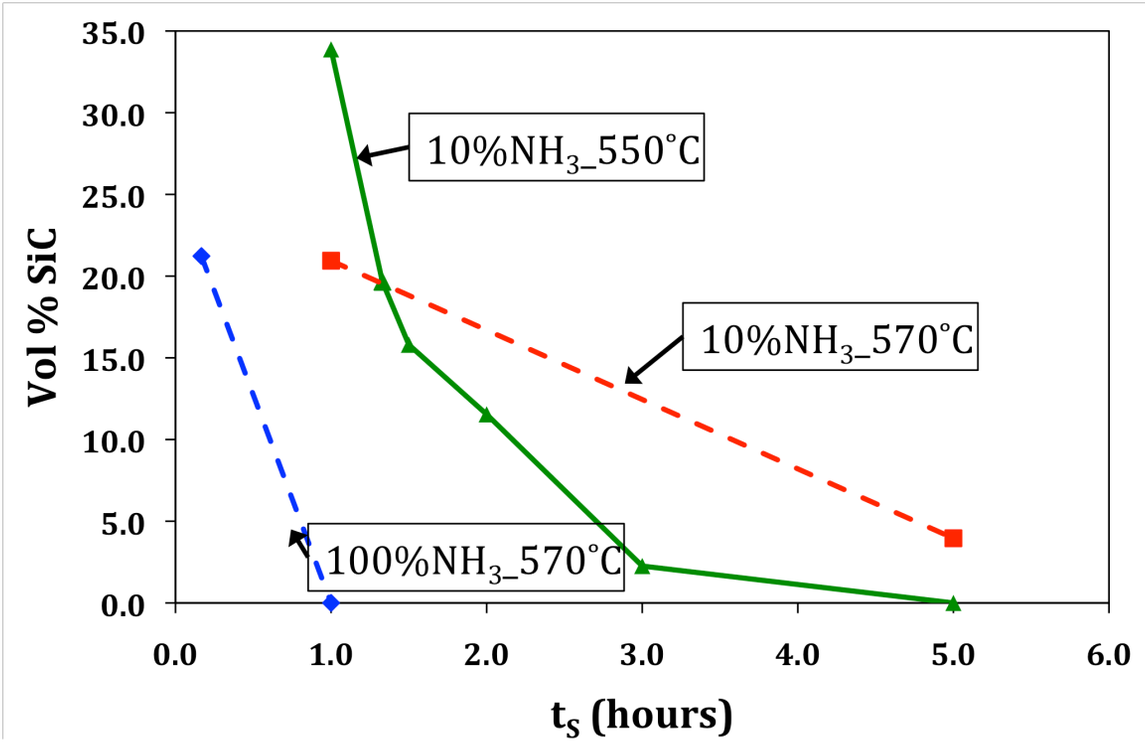

Figure 5.11 Resulting vol% SiC based on switching times (t_S). The vol% SiC was measured on samples that were crystallized at 1650 ˚C in nitrogen atmosphere.

Crystallite size was measured from the XRD patterns of the 10$NH_3$550˚C series. Table 5.2 shows the results of the crystallite size measurements. One interesting observation is that the β-SiC crystallite size remains approximately the same (< 40nm) for all of the samples.

Table 5.2 Crystallite size measurements of the 10$NH_3$550˚C series after heat treatment at 1650 ˚C in nitrogen atmosphere.

Sample ID	Phase	Volume %	Crystallite Size (nm)
10NH_3_550C_1hr	β- SiC	33.9	32
	β – Si_3N_4	13.1	292
	α - Si_3N_4	53.0	550
10NH_3_550C_1.5hr	β- SiC	15.8	38
	β – Si_3N_4	12.9	87
	α - Si_3N_4	71.3	687
10NH_3_550C_2hr	β- SiC	11.5	34
	β – Si_3N_4	11.8	130
	α - Si_3N_4	76.7	750
10NH_3_550C_3hr	β- SiC	2.3	93
	β – Si_3N_4	13.3	908
	α - Si_3N_4	84.4	1178
10NH_3_550C_5hr	β- SiC	0.0	
	β – Si_3N_4	0.0	
	α - Si_3N_4	100.0	>1000

5.4.2 Characterization of Polymer to Ceramic Transition

A series of FTIR experiments were performed in order to obtain a better understanding of the reaction mechanisms occurring during the controlled NH_3 treatment. FTIR was conducted on Ceraset crosslinked in an Argon atmosphere. The crosslinked powder was then heated in a 10NH_3/Ar balance atmosphere to 550 ˚C for 0, 1, 2, 3 and 5 hours and cooled immediately. Figure 5.12 shows the results of the FTIR experiments. The argon crosslinked Ceraset is similar to that observed in the literature.[126] Upon heating in a 10%NH_3 atmosphere there is a significant decrease in the Si-H band and over time a decrease in the Si-CH_3 and the C-H alkyl bands. There is also an increase in the N-H band. These results match with the literature theory that there are substitution reactions occurring at the Si-H and Si-C sites.[136] However, it is difficult to determine if the disappearance of the Si-H, Si-CH_3, and C-H bands are due to substitution reactions with NH_3 or due to thermal decomposition as these bands tend to disappear with increasing temperature.[126] Figure 5.13 shows FTIR results comparing crosslinked Ceraset

powder that was heated to 550 ˚C for 1 hour in Ar. The results show that the Si-H peak is present in the Ar550˚C1h sample but not in the 10%$NH_3$550˚C1h sample. There is also a decrease in Si-CH_3 and C-H alkyl bands as well as an increase in N-H band. This would confirm that observation made in Figure 5.12 are likely due to NH_3 substitution reactions rather than thermal decomposition.

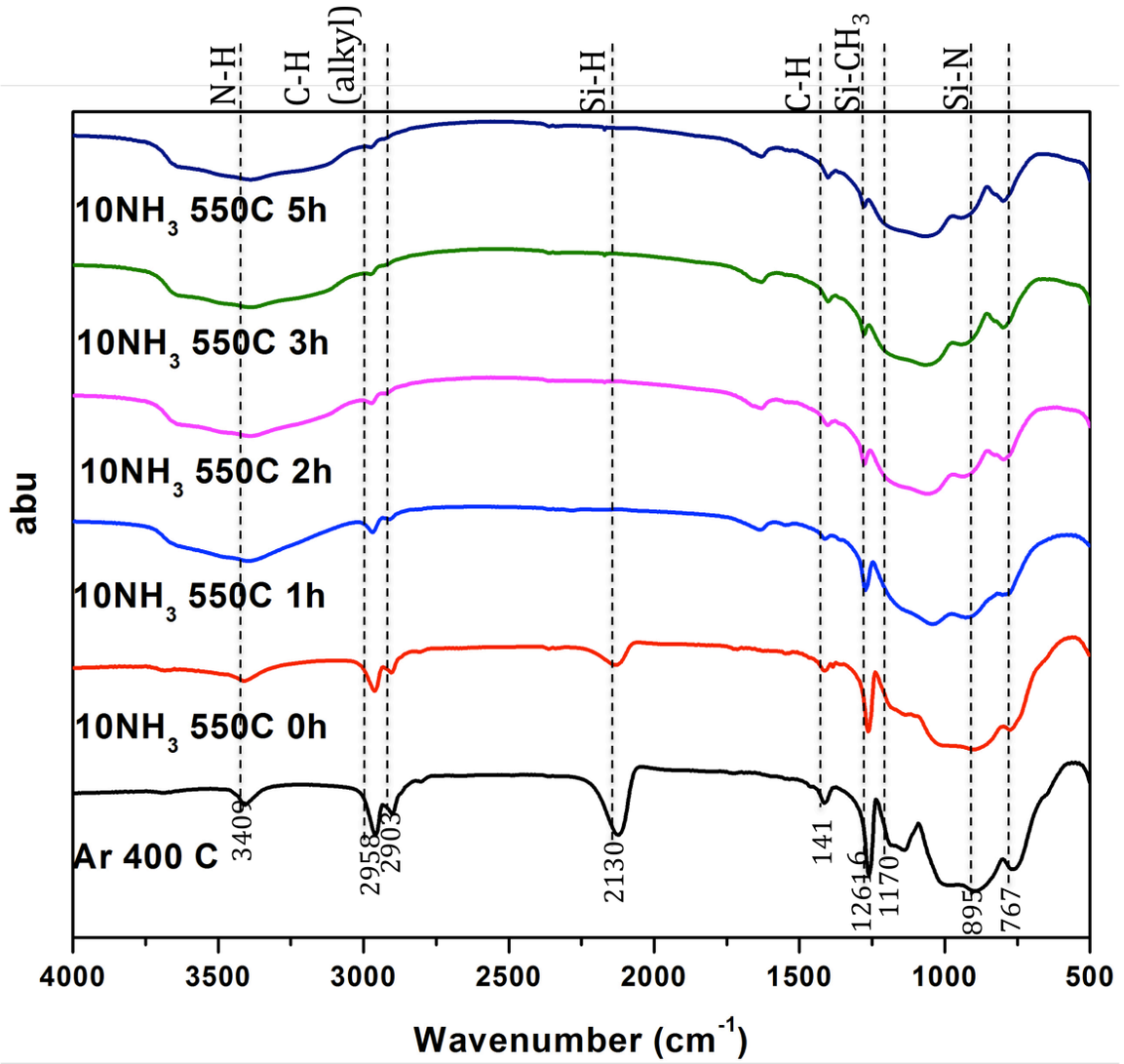

Figure 5.12 FTIR of crosslinked Ceraset powder heated in a 10%NH_3 atmosphere for 0, 1, 2, 3, and 5 hours.

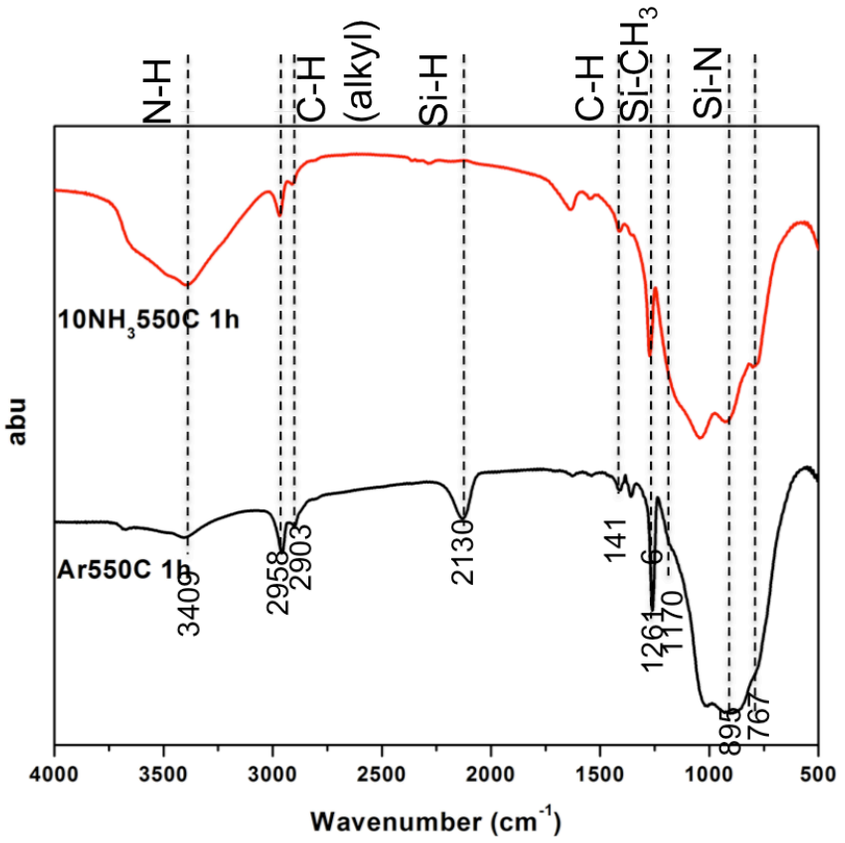

Figure 5.13 FTIR of crosslinked Ceraset powder heated in Argon and 10NH_3 atmosphere for 1 hour.

Raman spectroscopy was conducted on the 10$NH_3$550˚C series. The pyrolyzed powders were pressed into a pellet and heated to 1650, 1750, and 1850 ˚C for 2 hours under flowing N_2. The samples were embedded in a loosely packed bed of Si_3N_4 powder to ensure that decomposition of the Si_3N_4 did not occur according to Eq. 2.9. As described in Section 2.3.2, the amorphous SiCN pyrolyzed PDC should go through carbothermal reduction and consume all of the free carbon phase. Figure 5.14 shows a free carbon phase present up to 1750 ˚C. Two peaks labeled D and G represent the free carbon phase. The D band represents a disordered carbon phase whereas the G represents an ordered carbon phase. In this case the G band is indicative of a graphite phase. Generally the free carbon phase is not present above 1600 ˚C for polysilazanes where the Si:C ratio <1.[145,146] At 1850 ˚C the free carbon phase is no longer present in these samples.

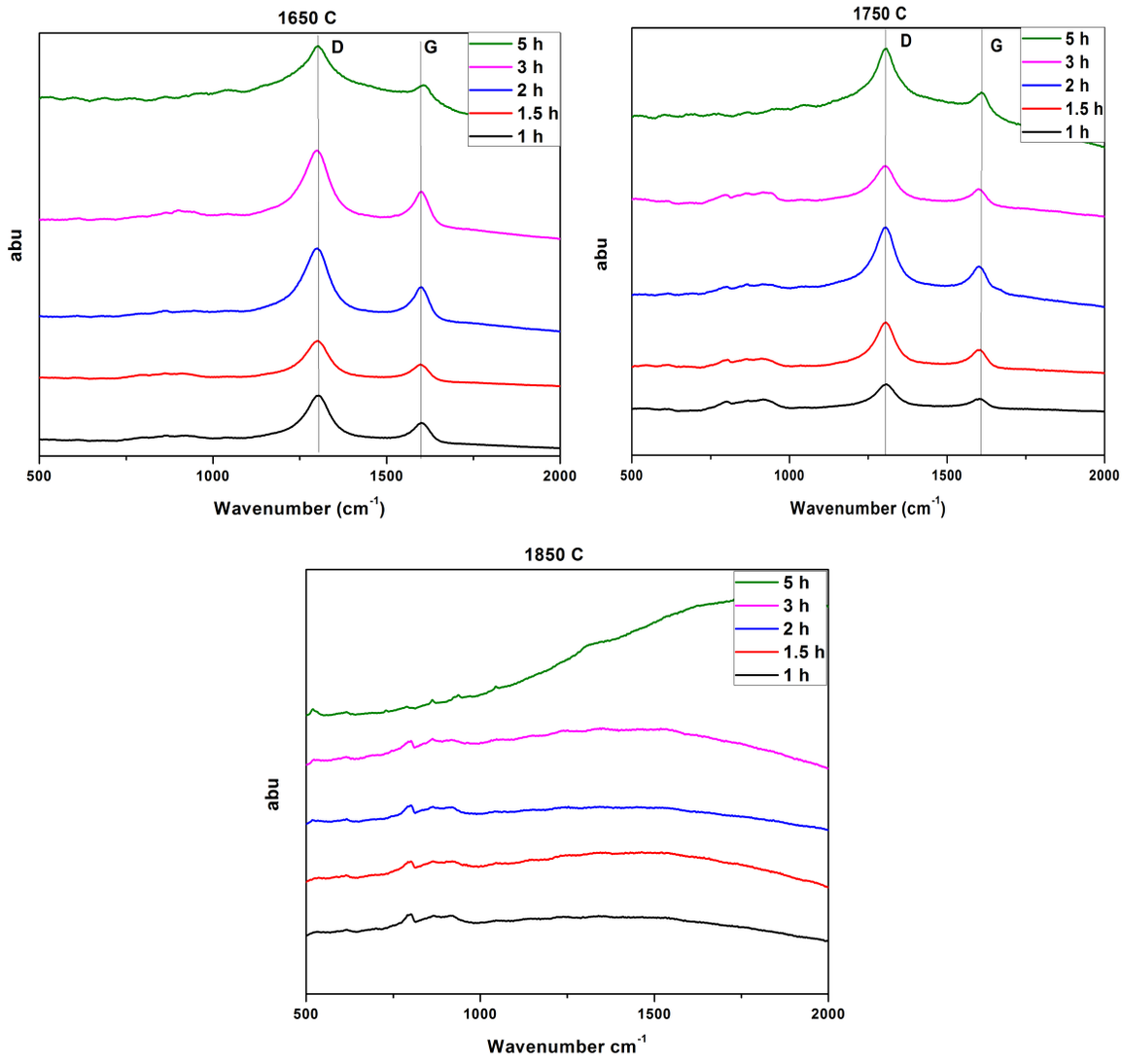

Figure 5.14 Raman spectroscopy of the 10NH$_3$550˚C series pyrolyzed at 1050 ˚C than crystallized at 1650, 1750, and 1850 ˚C in nitrogen atmosphere.

5.4.3 Scale-Up Process

The controlled ammonia process, described above, was developed using only 5 g of crosslinked Ceraset powder, which yielded ~3.8 g of pyrolyzed powder. Large quantities of powders are necessary for processing large sintered parts for mechanical testing. Since the furnace runs range from 12 – 16 hours per run only 1 furnace run could be operated in a day. It would take ~26 straight days to produce ~100g of powder for one concentration of SiC. This would take an enormous amount of time and resources to produce 5 series of varying SiC content. Utilizing a larger crucible was not an option as there was concern that there would be a

reaction gradient from the top to the bottom of the powder bed since the NH_3 would be passing over the powders. This called for new design to make larger quantities of powder.

A rotary tube furnace was selected as the proper technique for scaling up this reaction process, as it would allow for the crosslinked powder to be evenly mixed as the NH_3 gas flowed through the tube. Since a rotary tube furnace was not available, one was built using existing tube furnaces in the laboratory. Figure 5.15a and 5.15b shows the design of the quartz tube blown for the rotary furnace. The 3 in. diameter portion of the tube had 1 in. blades fused to the inside to allow for adequate mixing as the as the tube rotated. A quartz filter was fused to the inside diameter of the 2 in tube where it tapers to the 3 in diameter tube. This was to prevent any of the crosslinked powder from flowing down the exhaust end of the tube during the reaction process. A gear was mounted to the 2 in diameter portion of the tube and placed on a gear motor, which was secured to the laboratory table, to allow the tube to rotate during the furnace runs (Figure 5.15c).

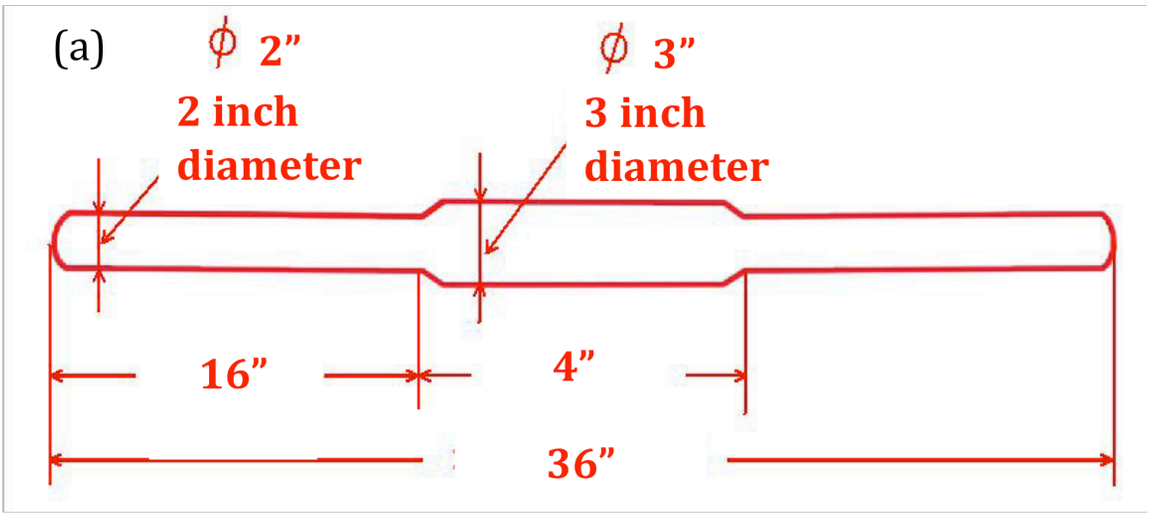

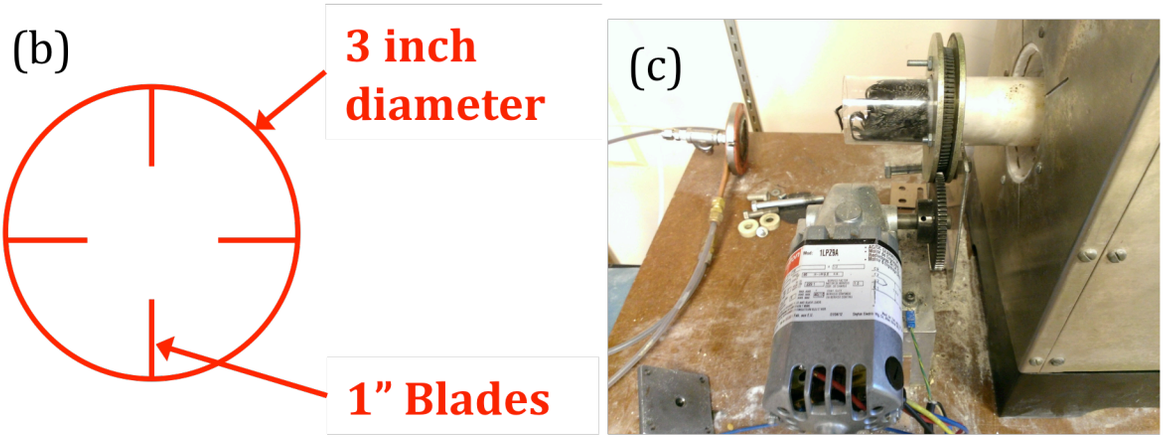

Figure 5.15 Design for Rotary tube furnace, which shows (a) the dimensions of the quartz glass piece, (b) cross section of the quartz glass showing the blades used for mixing and (c) image of the quartz piece connected to a gear motor to allow for the quartz piece to rotate during the furnace run.

The rotary furnace design utilized 45 g batches, which yielded ~30 g of pyrolyzed ceramic powder. Initially, the processing parameters established previously were used with the rotary furnace to produce the large batch powders (10%NH_3 gas at 550 ˚C for varying time). However, the 10%NH_3 gas yielded very high SiC (>50 vol. %) even at very long holding times (>5 hr). The low concentration of NH_3 in the atmosphere was not sufficient for an efficient reaction with the large quantities of powders used in the rotary furnace design. Using a 100% NH_3 atmosphere yielded lower SiC content needed with this project. For each batch, a small quantity of the resulting pyrolyzed ceramic powders was heat-treated in a nitrogen atmosphere to 1650 ˚C for 2 hours and quantified via XRD. Table 5.3 shows the resulting SiC content for each batch. As seen in Table 5.3, there is some batch-to-batch variation in the amount of SiC. This is most likely due to variation in gas flow rate, tumbling of the powder and temperature variation. However, each match was thoroughly mixed after the reaction so it is believed that the SiC content is representative of the entire batch. The batches were mixed in order to yield ~100 g of pyrolyzed powders for SiC contents of approximately 5, 10, 20 and 30 vol. %. A 0% SiC series was achieved by pyrolyzing 45 g batches of crosslinked Ceraset powders in 100% NH_3 atmosphere to 1050 ˚C without switching the gas Argon. At the end of this process large

quantities SiCN ceramic powders were produced that yielded approximately 0, 5, 10, 20 and 30 vol% SiC. These 5 sets of powders were used to process dense Si_3N_4/SiC nanocomposites as discussed in Sections 6.2 and 6.3.

Table 5.3 Various batches using the rotary tube furnace design which shows the holding time at 550 ˚C in NH_3 and the resulting vol.% SiC.

Time (min)	vol % SiC/batch	mass (g)	vol% SiC total
30	35.8	30	32.4
30	33	14	
30	30.8	30	
30	30.3	30	
18	40	14	19.3
60	17.5	14	
60	16.9	30	
60	16.3	30	
60	15	30	
100	12.5	30	10.1
120	11.5	30	
120	8.3	30	
120	8	30	
120	7.3	30	5.2
180	6.6	14	
180	6.3	14	
180	4	30	
180	3.3	30	

5.5 Milling

A Spex Mixer/Mill 8000M (Spex SamplePrep, Metuchen, NJ, USA) high energy ball mill was used for all milling experiments. All vials stated throughout this section were sealed within a Nitrogen pure glove box to reduce oxidation of the samples. Initially a ZrO_2 vial with two 0.5" ZrO_2 balls (Spex 8005 Zirconia grinding set) was used to dry mill the crosslinked Ceraset polymers for 20 min into a fine powder followed by dry milling the pyrolyzed Ceraset for 10 hours. A preliminary FAST sample clearly shows the ZrO_2 contamination (Figure 5.16). Further milling experiments were performed using a methacrylate vial (Spex 8006).

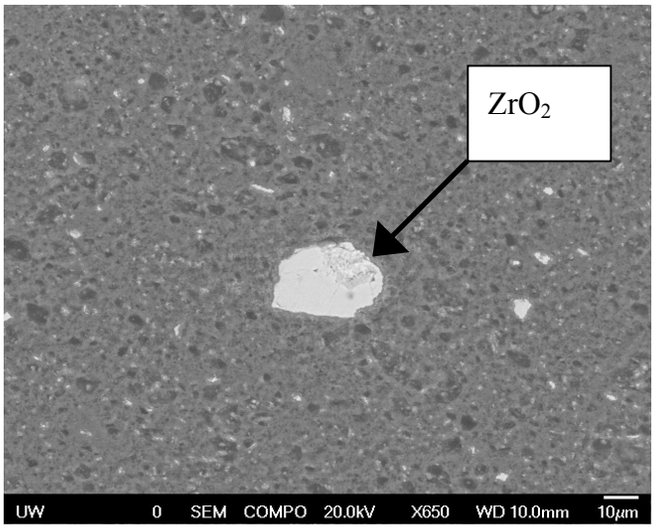

Figure 5.16 FAST sample of Ceraset milled in ZrO_2 vial with 2-0.5" ZrO2 balls.

Crosslinked Ceraset/SMP-10 was milled with a methacrylate vial and 5 mm ZrO_2 balls at a 4:1 ball:charge ratio for 100 min. The crosslinked powders were pyrolyzed and dry milled in a methacrylate vial with 2-0.5" Si_3N_4 balls for 10 hours. This milling technique was used for SMP-10, 80:20, 50:50, 20:80 and CerasetNH_3 samples (See Section 5.2 for Sample ID information). These samples were use for the first series of FAST runs (See Section 6.1.2). Figure 5.17 shows a very broad distribution of particle sizes with a D50 = 1.2 μm. Increasing the milling time to 24 hours reduced the average particle size (D50 = 0.67), however, there still remained a broad distribution with many particles >1 μm.

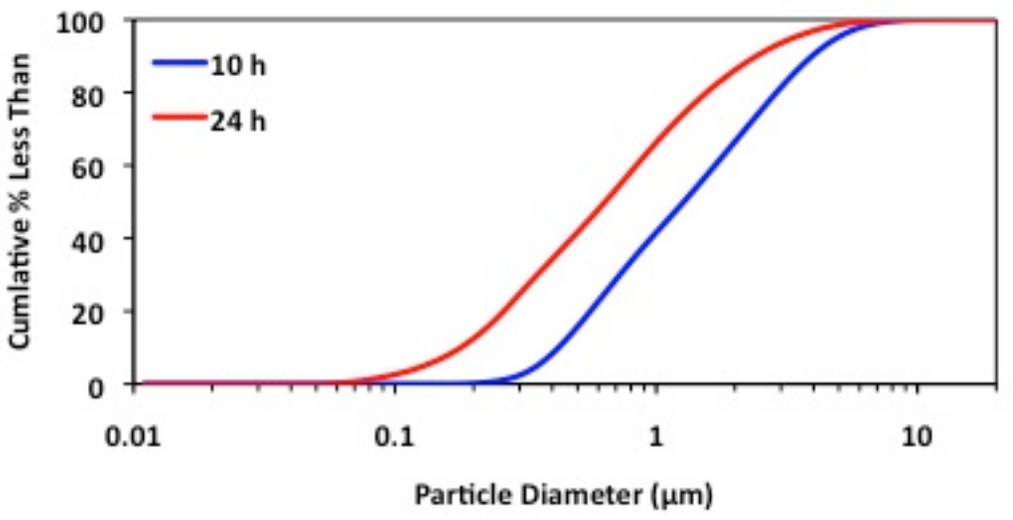

Figure 5.17 PSA of pyrolyzed 80:20 dry milled in a methacrylate vial with 2-0.5" Si_3N_4 balls for specified times.

Focused was then placed on the size of the crosslinked polymer powders and their affect on the pyrolyzed particle size and distribution. Crosslinked Ceraset was dry milled in a methacrylate vial with 5 mm ZrO_2 balls at a 4:1 ball:charge ratio for 15 min., 5, 10, 15, and 24 hours. Figure 5.18 shows the reduction of particle size of the crosslinked powders with increasing milling time. The 24 hour milled sample was pyrolyzed at 1050 ˚C for 2 hours and then it particle size measured. The results show (Figure 5.19) a very broad particle size distribution with a D50 = 2.96 µm. One goal was for the pyrolyzed powders to be sub-micron.

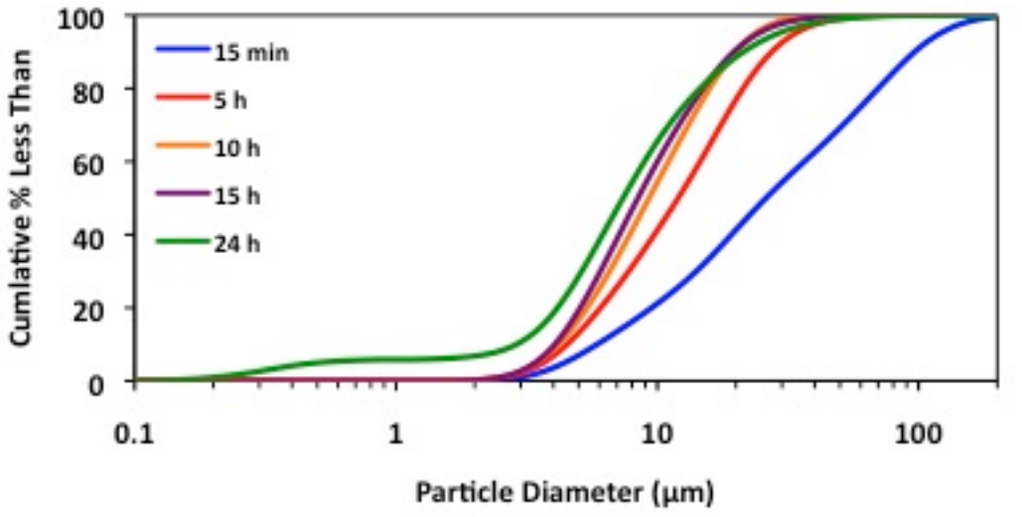

Figure 5.18 Crosslinked Ceraset dry milled in a methacrylate vial with 5mm ZrO_2 balls at a 4:1 ball:charge ratio for various times.

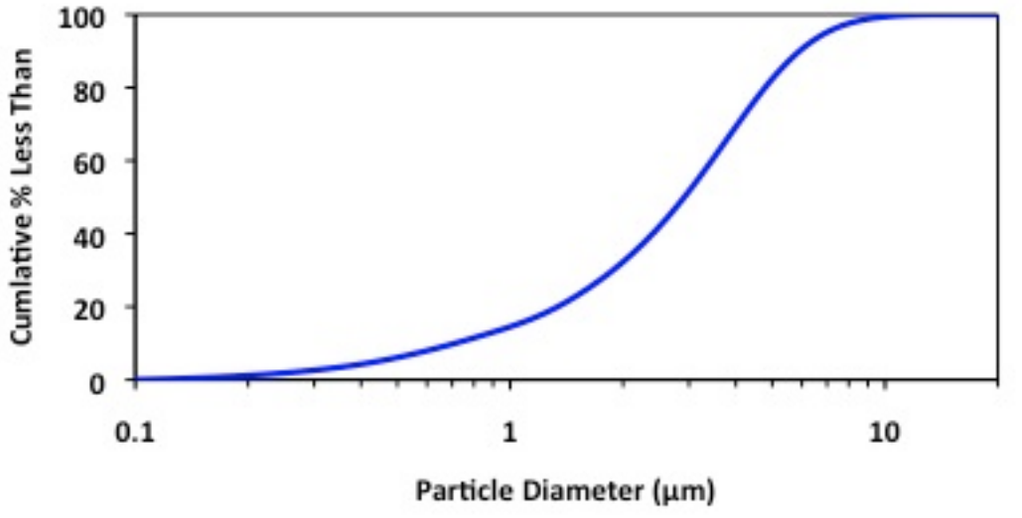

Figure 5.19 PSA of crosslinked Ceraset that was milled 24 hours and pyrolyzed.

A second approach was used to reduce the particle size of the crosslinked powders. The crosslinked Ceraset that was high energy ball milled for 24 hours was dry roller ball milled with 5 mm Al_2O_3 cylinders at a media:charge ratio of 50:1 for 48 hours. The PSA (Figure 5.20) shows a bimodal distribution of particles, however, it was possible to reduce half of the particles to less than 1 µm. The roller ball milled crosslinked powders were pyrolyzed and their particle

size measured (Figure 5.21). The particle size distribution is still very broad and the average particle size (D50 = 2.27 µm) is not much lower than that of Figure 5.19 (D50 = 2.96 µm).

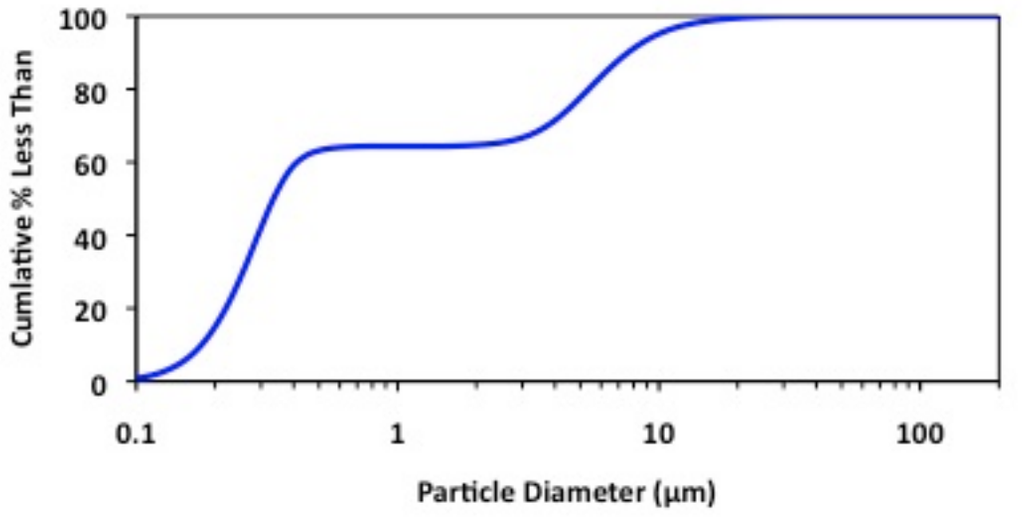

Figure 5.20 PSA of crosslinked powder Ceraset that was roller ball milled with 5mm Al_2O_3 cylinders at a media:charge ratio of 50:1 for 48 hours.

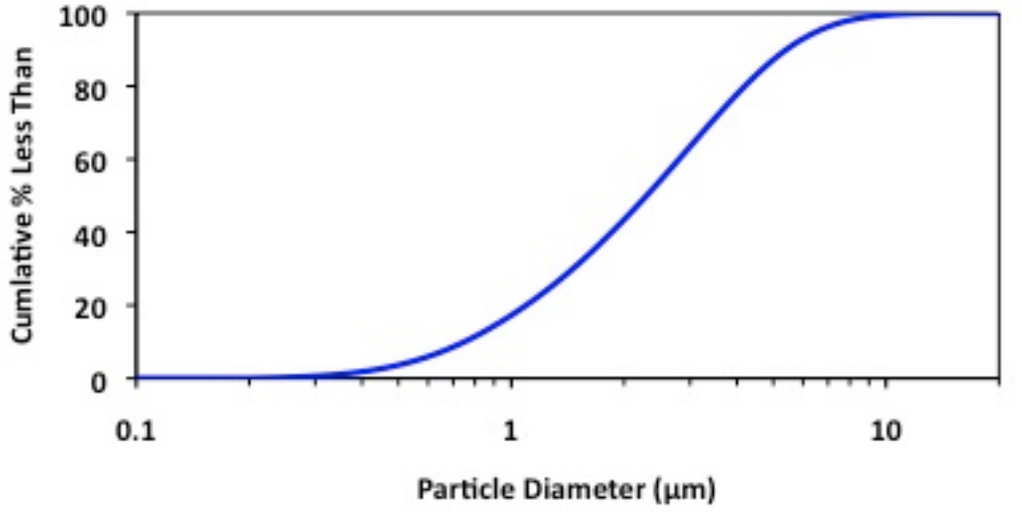

Figure 5.21 PSA of crosslinked Ceraset that was roller ball milled for 48 hours and pyrolyzed.

From these experiments, it was concluded that the size of the crosslinked powders has little affect on the size of the pyrolyzed powders, therefore, the primary focus was shifted to

milling the pyrolyzed powders. The crosslinked Ceraset was dry milled in a methacrylate vial with 5 mm ZrO_2 balls at a 4:1 ball:charge weight ratio for 100 min. This milling procedure was chosen because the particle size of the crosslinked powders was relatively small (D50 = 10.01 μm) and the particle size and distribution is consistent from batch to batch (Figure 5.22). Milling studies were then conducted on these powders that were pyrolyzed at 1050 ˚C under argon.

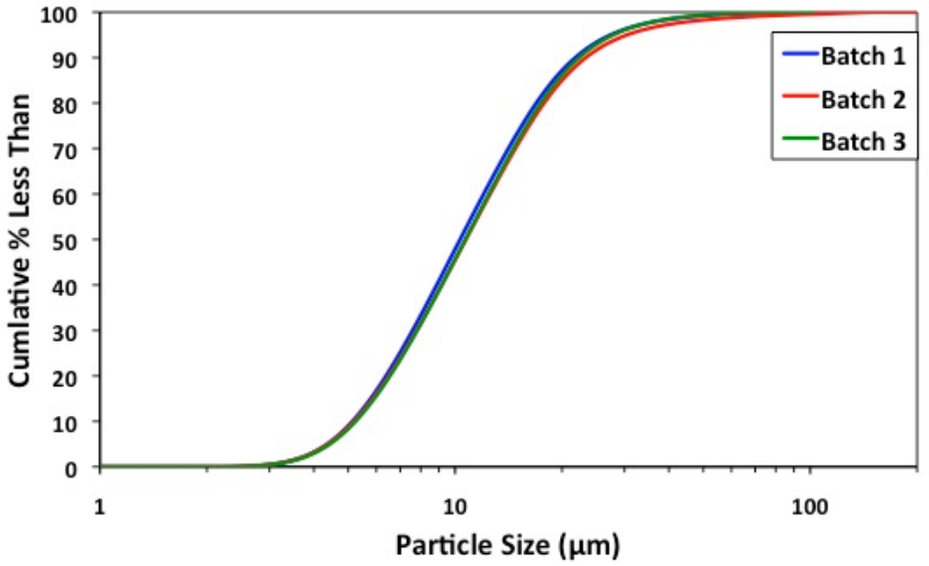

Figure 5.22 Three batches of crosslinked Ceraset milled in a methacrylate vial with 5 mm ZrO_2 balls at a 4:1 ball:charge weight ratio for 100 min.

A Si_3N_4 vial (Spex 8008) was used in an attempt to increase milling efficiency over the methacrylate vial. Initially dry milling 5 g of pyrolyzed powder with 2-0.5" balls was used, however the powder caked to the walls of the vial. Next 5 g of pyrolyzed powder was milled in the Si_3N_4 vial with 2-0.5" Si_3N_4 balls and hexane as a liquid medium. Milling was conducted over 24 hours. When the 0.5" Si_3N_4 balls were removed the surfaces appeared extremely rough causing a fair amount of contamination to occur. This is because in a Spex Mixer/Mill there are extremely high contact forces between the balls. These contact forces are much higher than that needed to crush the particles.[147] Reducing the size of the media will reduce the contact force. Also, with a decrease in media size there is an increase in the amount of media within the vial,

therefore, there are more contacts per revolution increasing the efficiency of the milling cycle.[148] Efficient milling of sub-micron Si_3N_4 powders has been shown with attrition milling using small diameter media (1 -2 mm).[149]

Pyrolyzed Ceraset powders were milled in a Si_3N_4 vial with 1 mm diameter Si_3N_4 balls at a 2:1 ball:charge weight ratio in hexane at various times. Figure 5.23 shows that with a milling time of 25 hours a sub micron powder with a narrow particle size distribution can be achieved.

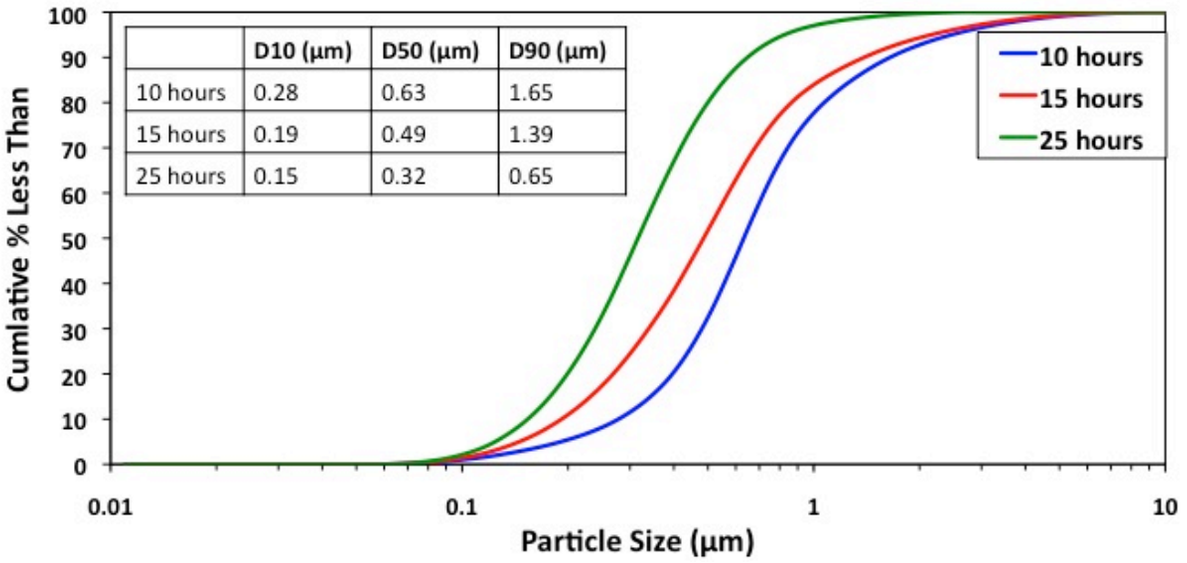

Figure 5.23 PSA of pyrolyzed Ceraset milled in a Si_3N_4 vial with 1 mm Si_3N_4 balls at a 2:1 ball:charge weight ratio in hexane at various times.

The Spex Mill is able to produce sub micron particles sizes of the pyrolyzed powders; however, it is limited to very small batches (max 10 g) due to the size of the Silicon Nitride Vial. The 100 g batches of SiCN powders produced in the previous section were milled using an attrition mill. 8 wt% Lu_2O_3 was added to each series prior to milling. The powders were milled in a Teflon coated steel pot with hexane and 5 mm Si_3N_4 balls at a 5:1 ball:powder weight ratio. Si_3N_4 attritor arms were used to mill the powders at 400 rpm for 2 hours. Table 5.4 shows the resulting average particle size for each batch. This process was selected since it produced large quantities of powders of the desired size.

Table 5.4 Particle size of the attrition milled SiCN powders.

Vol.% SiC	Average Particle Size (μm)
0	0.63
5	0.64
10	0.73
20	0.68
30	0.65

Chapter 6

Results of Processing and Characterization on Dense Si_3N_4/SiC Nanocomposites

6.1 Preliminary Consolidation Studies

6.1.1 Pressureless Sintering Studies

Pressureless sintering was first explored in an attempt to generate dense nanocomposites since this is the most versatile consolidation route. A pyrolyzed 50:50 and SMP-10 samples was milled with a methacrylate vial with 2 0.5" Si_3N_4 balls for 10 hours. The powders were then pressed into a pellet in a 0.5" diameter steel die at 100 MPa pressure. The pellets were heat treated at 5 ˚C/min to 1650 ˚C for 2 hours in a flowing N_2 (50:50) and Argon (SMP-10) atmospheres. Table 6.1 shows very low densities of the pressureless sintered samples and Figure 6.1 shows SEM images of the porous microstructures. This is very low temperature and pressure than is typically seen for sintered Si_3N_4 materials, which is why these samples were so porous.[46,63,73,150]

Table 6.1 Densities of pressureless sintered samples. Relative density is based % theoretical density of β-SiC (3.21 g/cc).

Sample ID	**Density g/cm^3**	**Relative Density %**
SMP-10 Ar	1.76	55
50:50 N_2	1.51	47

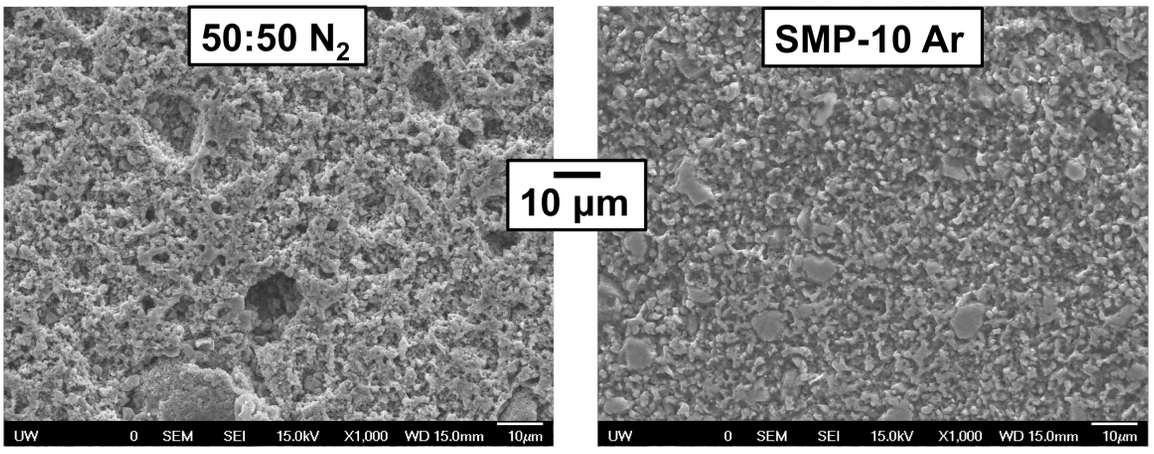

Figure 6.1 SEM of pressureless sintered 50:50 (left) and SMP-10 (right).

6.1.2 Field Assisted Sintering (FAST)

Prof. Eugene Olevsky's group at San Diego State University conducted Field Assisted Sintering (FAST) (DR. SINTER LAB SERIES, FUJI ELECTRONIC INDUSTRIAL CO., LTD., Japan) for all samples presented in this section. The first series included samples of mixed polymers (Section 5.2) and Ceraset pyrolyzed in ammonia atmosphere. Pyrolyzed SMP-10, 20:80, 50:50, 80:20, and Ceraset NH_3 powders were ball milled in a methacrylate vial with 2-0.5" Si_3N_4 balls for 10 hours. The resulting powders were placed in a 15 mm diameter graphite die and field assisted sintered at 100 ˚C/min to 1600 ˚C for 30 min with an applied pressure of 63 MPa. Some samples were sintered under a N_2 atmosphere, however, this caused complications to the equipment during sintering. The remaining samples were sintered in a Vacuum environment. The resulting densities of the samples were very low in the 60 – 70% relative density range (Table 6.2). Figure 6.2 shows a polished and etched image of the porous microstructures observed from the process. The reason for the low densities is attributed to the large particle sizes which reduces the driving forces for sintering.[59] Also, no sintering aids were used which are need for densifying Si_3N_4 materials.[63] The initial experiments were an attempt to repeat literature data where a dense Si_3N_4/SiC nanocomposites was made without the use of sintering aids.[36]

Table 6.2 Density measurements of FAST samples.

Sample ID	Conditions	Density g/cm^3	Relative Density %
50:50_01	N_2	1.89	59
Ceraset_NH_3_02	N_2	1.99	62
20:80_01	Vacuum	2.29	72
20:80_02	Vacuum	2.26	71
80:20_01	N_2 failed at 1600 °C	1.97	62
80:20_02	Vacuum	1.86	58
80:20_03	Vacuum	1.95	61
SMP-10_02	N_2	2.21	69
SMP-10_03	N_2	2.15	67

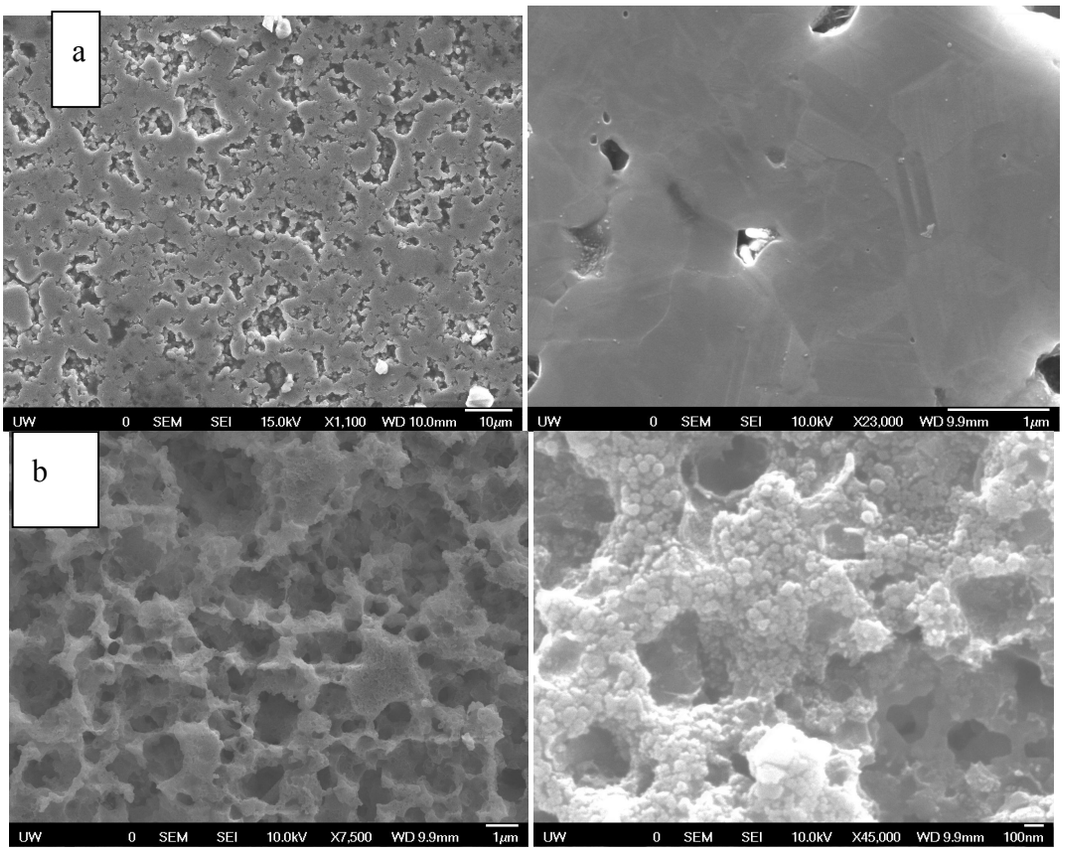

Figure 6.2 Polished and plasma etch SEI image of the field assisted sintered 80:20 (a) and CerasetNH_3 (b) samples.

The second set of FAST samples were made from Ceraset that is pyrolyzed in a 10%NH_3 atmosphere to yield a 25v%SiC composite (SiCN25v%SiC) and Ceraset mixed with 7.74 wt.% SiC nanoparticles and pyrolyzed in a 100%NH_3 atmosphere to yield a 10 v% SiC composite (SiCnp10v%SiC). These pyrolyzed samples were milled in a Si_3N_4 vial with 1 mm Si_3N_4 balls at a 2:1 ball:charge weight ratio in hexane for 10 hours. 7.4wt% Lu_2O_3 was added as a sintering aid to the pyrolyzed powders prior to milling. The resulting powders were placed in a 15 mm diameter graphite die and sintered at 100 ˚C/min to 1500 ˚C and then 50 ˚C/min to 1700 ˚C for 30 min with an applied pressure of 63 MPa under vacuum. The densities were much greater (>90% TD) than the previous set of samples. This is due to a combination of the smaller particle size and the addition of Lu_2O_3 as a sintering aid. Figure 6.3 displays the microstructure of the SiCN25v%SiC sample. Figure 6.3a displays a plasma etched sample where the depressed phase is the Si_3N_4 phase and the raised phase is the SiC phase. This image is difficult to distinguish the individual grains of the Si_3N_4 and SiC grains, which makes it difficult to quantify the microstructure. Figure 6.3b shows a polished specimen that was imaged in BEI mode. The grain boundaries are clearly observable, however, the Si_3N_4 and SiC cannot phases cannot be distinguished because of their similar atomic number. The microstructure shows extremely fine grain size (<0.5 μm).

Table 6.3 Densities of the second set of FAST samples.

Sample ID	Density (g/cm^3)	Relative Density (%)
SiCN25v%SiC	3.01	94.1
SiCnp10v%SiC	3.12	97.5

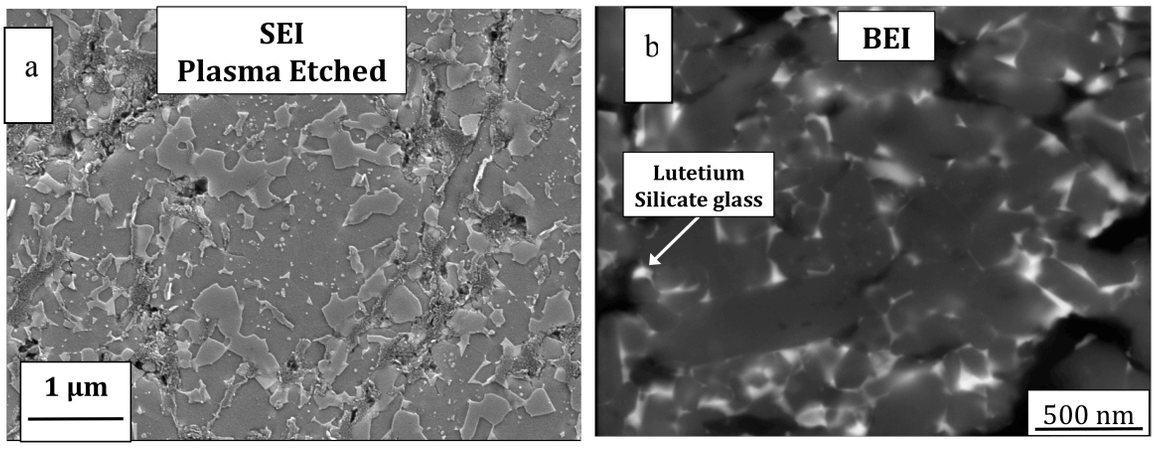

Figure 6.3 Microstructure of SiCN25v%SiC sample polished and plasma etched and imaged in SEI mode (a) and polished and imaged in BEI mode(b). Right image courtesy of Prof. Art Heuer Case Western University.

The microstructures of the SiCnp10%SiC sample (Figure 6.4) are much different than that above. There are fibers interconnected throughout the network. These fibers can be associated with Si_2N_2O phase as confirmed by XRD (Figure 6.5). It is unknown why these fibers have formed, however, it is speculated that it has to do with SiC nanoparticles because these fibers do not occur in the SiCN25v%SiC sample.

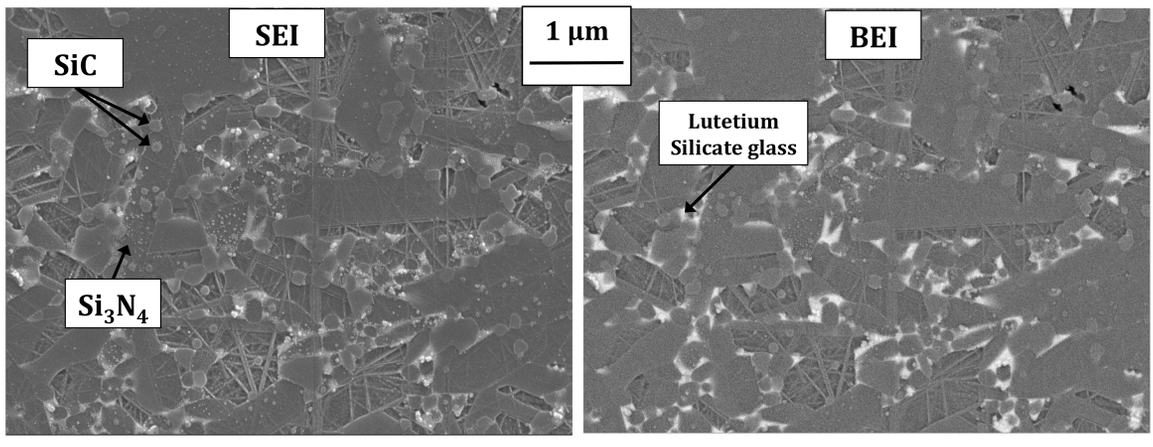

Figure 6.4 Polished and plasma etched SiCnp10v%SiC sample in SEI (a) and BEI (b) mode.

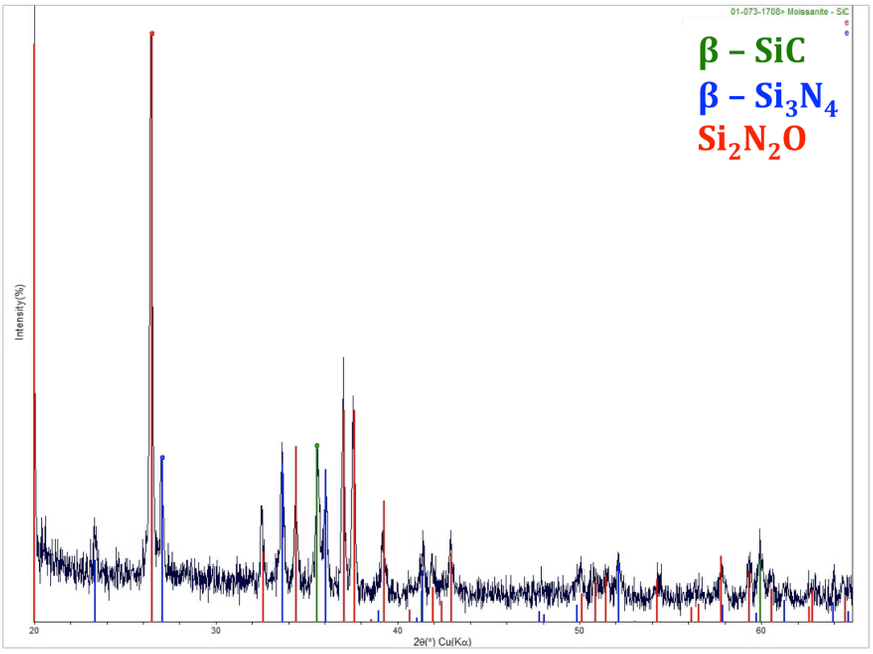

Figure 6.5 XRD of SiCnp10v%SiC sample.

The linear displacements of the previous set of FAST samples were recorded during densification. One thing that can be noted from this data (Figure 6.6) is that there is insignificant amount of densification during the dwell time. Future samples will not need such a long hold time.

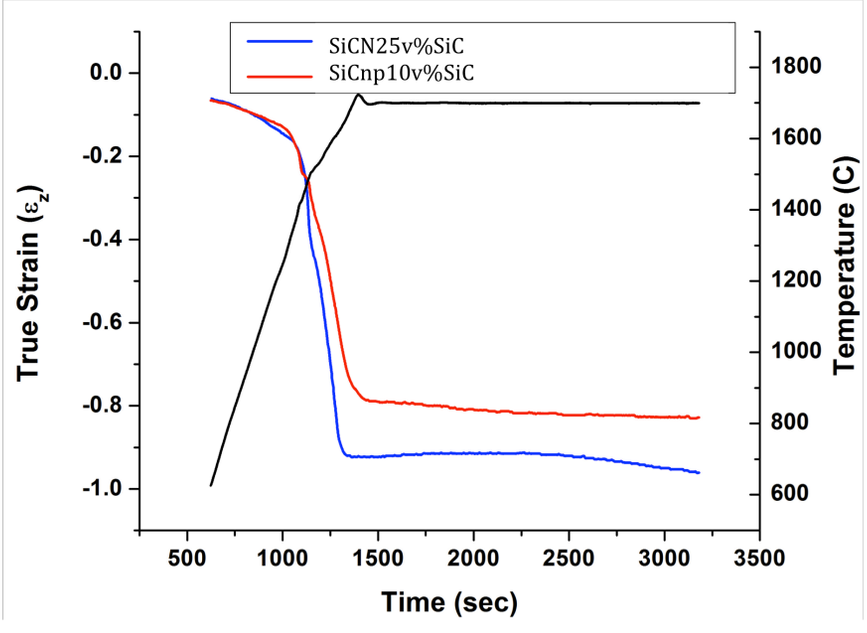

Figure 6.6 True Strain data for densification of SiCN25v%SiC and SiCnp10v%SiC.

6.1.3 Gas Pressure Sintering

Gas Pressure Sintering is another technique to try and generate a dense microstructure. Ceraset was pyrolyzed in a 100%NH_3 atmosphere to yield Si_3N_4. The pyrolyzed sample was mixed with 7.4wt% Lu_2O_3 and mill in a Si_3N_4 with 1 mm Si_3N_4 balls at a 2:1 ball:charge ratio in hexane for 24 hours. The powder was uniaxially pressed in a 0.5" steel die at 100 MPa. The pressed pellet was then placed in a graphite crucible that was covered with loosely pack Si_3N_4 and covered with loosely pack Si_3N_4 to avoid decomposition of the sample. The temperature and pressure profile is displayed in Figure 6.7. After sintering the sample was cracked. This is likely due to the uniaxial pressing of the pellet as cold isostatic pressing is preferred. Because of the large cracking the density of the sample was relatively low (82% TD). The microstructure of the sample (Figure 6.8) shows long elongated Si_3N_4 similar to that in the literature.[113] GPS can be used to generate dense microstructures with large elongated grains compared to FAST, which contains small equiaxed grains. Comparing these two types of microstructures is one of the goals of this project.

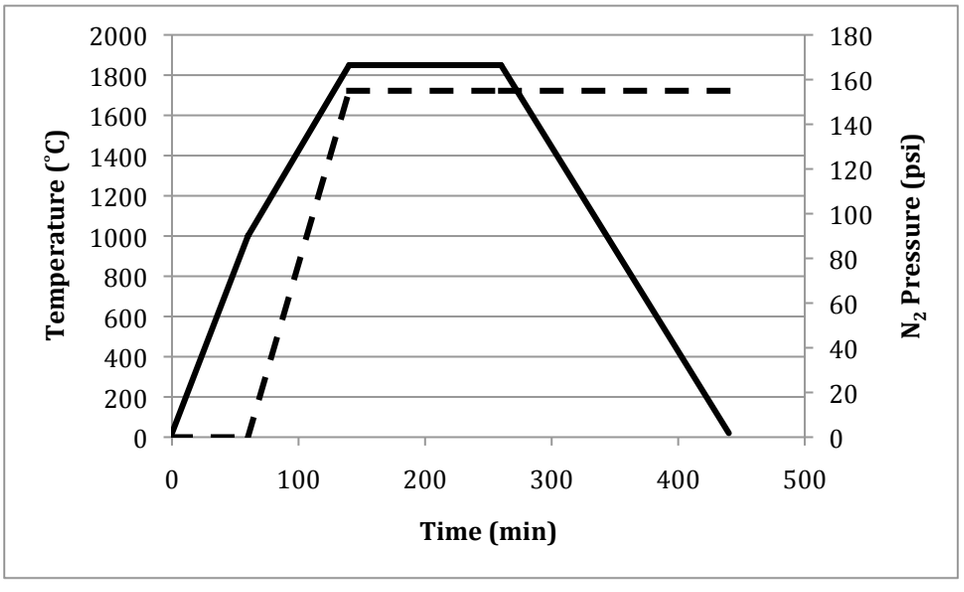

Figure 6.7 Temperature and pressure profile for GPS run.

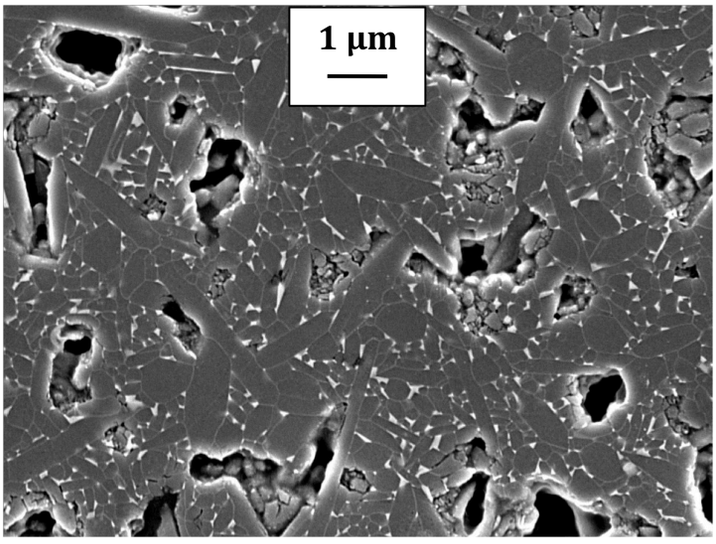

Figure 6.8 SEM image of polished and etched GPS sample.

6.2 Hot Pressing

The SiCN powders produced in Section 5.4.3, which yielded SiC content of 0, 5, 10, 20, and 30 vol.% and were attrition milled with 8 wt.% Lu_2O_3 and hot pressed to yield dense Si_3N_4/SiC nanocomposites. Powders were placed in a 20 mm diameter dies and hot pressed at 1770 ˚C with a load of 30 MPa and 0.15 MPa pressure of nitrogen during the 1 hour dwell time. Figure 6.9 shows the sintering profile for the hot pressed samples. The sample IDs for these samples are defined as HP0, HP5, HP10, HP20 and HP30 referring to the hot pressed samples with 0, 5, 10, 20 and 30 vol.% SiC. The densities of the resulting hot pressed samples are shown in Table 6.4 These samples are assumed to be near full density as they are larger than the densities of Si_3N_4 (3.184 g/cc) and β-SiC (3.21 g/cc). The reason densities are larger is due to the high density of Lu_2O_3 (9.42 g/cc). The theoretical densities cannot be calculated since the initial oxygen content of the SiCN powders was not known and reactions can occur between the free carbon and oxide phases.[42]

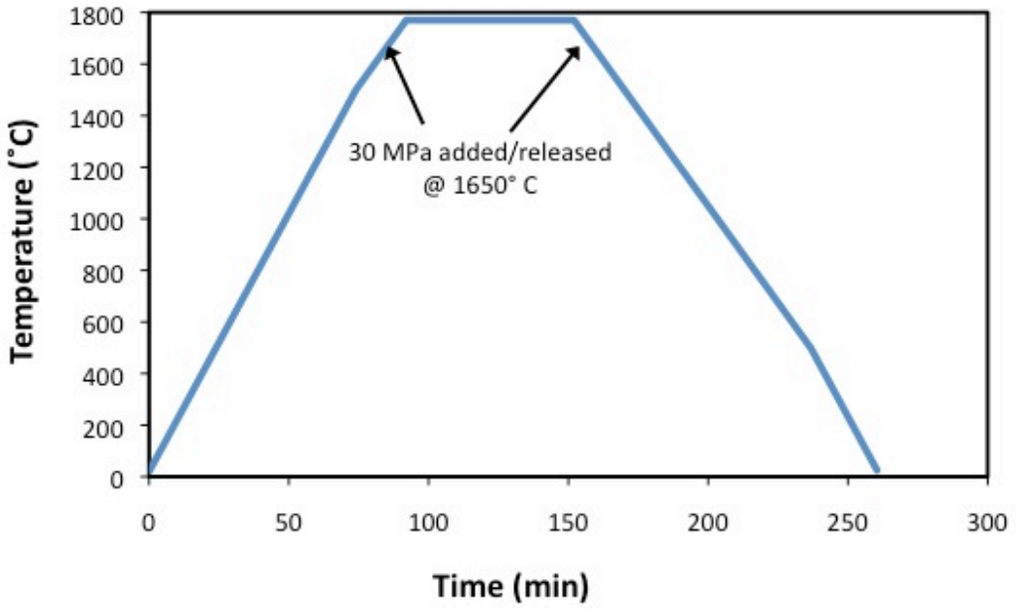

Figure 6.9 Sintering profile for Hot Pressed samples.

XRD results of the hot pressed samples are displayed in Figure 6.10. All five series show that the Si_3N_4 phase has completely transformed to the β-Si_3N_4 phase. Another interesting observation is the crystalline oxide phases that are present. HP0 has two oxide phases present: Sinoite (Si_2N_2O) and $Lu_2Si_2O_7$, whereas the remaining hot pressed samples (HP5, HP10, HP20 and HP30) all show a $Lu_4Si_2O_7N_4$ phase.

Table 6.4 Density measurements for Hot Pressed samples.

Sample ID	Density g/cm^3
HP0	3.32
HP5	3.31
HP10	3.29
HP20	3.26
HP30	3.25

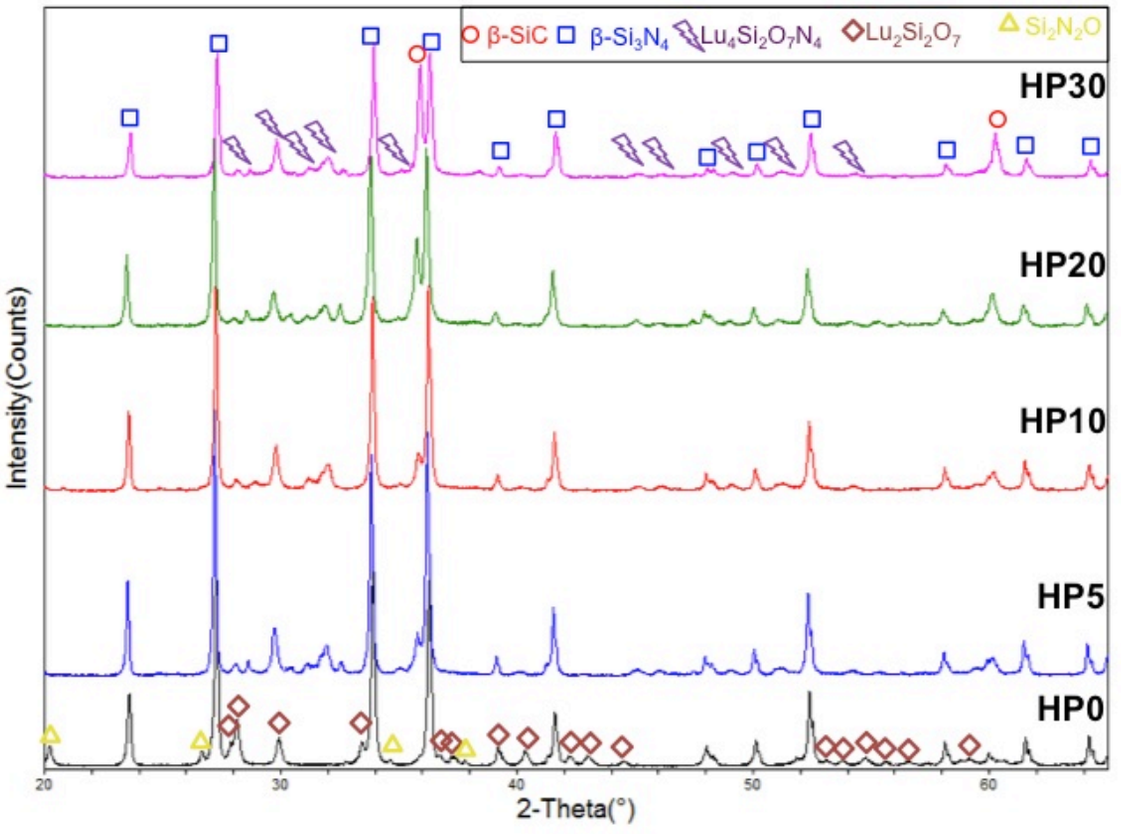

Figure 6.10 XRD of Hot Pressed samples.

As discussed in the previous section, it can be difficult to characterize the microstructural features of these nanocomposites in the SEM imaging modes. EDS mapping can also be problematic due to the large interaction volume from where characteristic X-Ray signals are obtained (Figure 6.11a). It can be difficult to distinguish the small SiC grains (<100 nm) when measuring characteristic X-Rays over a micron below the surface. By preparing a thin foil TEM sample (~50 nm thick) it is possible to eliminate the large interaction volume of the characteristic X-Rays (Figure 6.11b).[151] Figure 6.12 shows a C, N, O map of HP20 prepared by a FIB. The results clearly show C, N and O rich regions, which are indicative of SiC, Si_3N_4 and the lutetium silicate intergranular phases respectively. It is still difficult to distinguish individual grains for grain size analysis. Even at high magnification (Figure 6.13), EDS mapping has difficultly

distinguishing the individual grains. For example, in observing the carbon rich regions, it can be seen from the BEI image that there are many equiaxed grains. There is no way of discerning if all of the grains in this region are SiC or if some are Si_3N_4. All that is certain is that this is a carbon rich region and that there are likely many intergranular SiC grains located there.

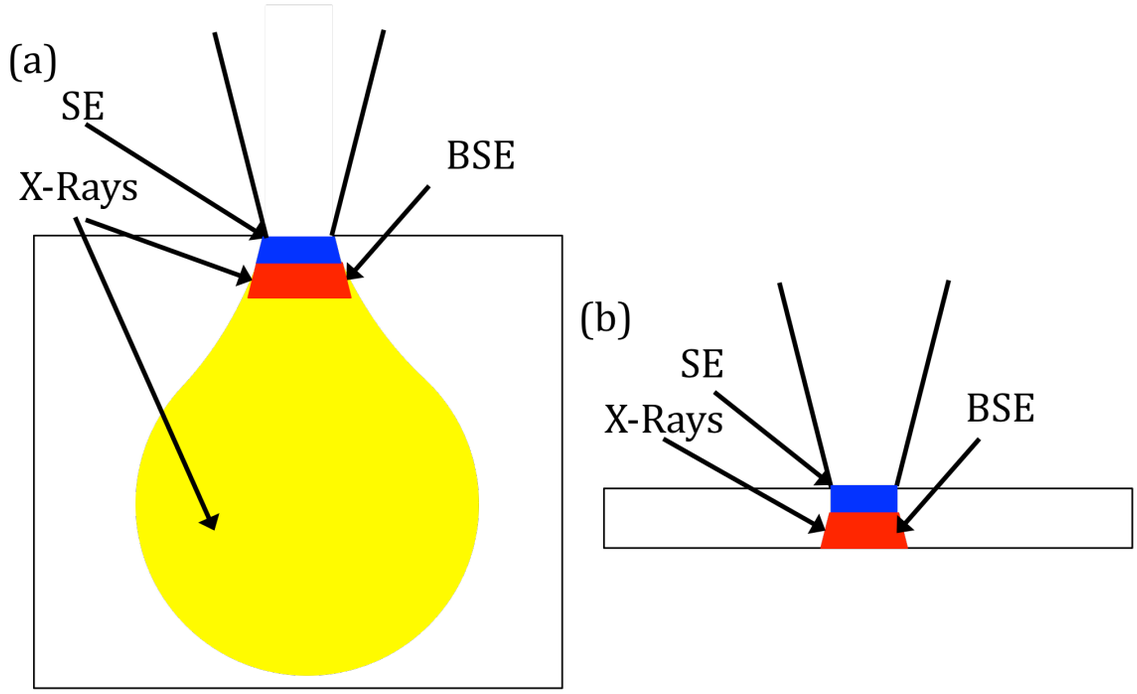

Figure 6.11 Schematic comparison of the X-Ray excitation regions of a (a) SEM bulk specimen and (b) TEM thin specimen.

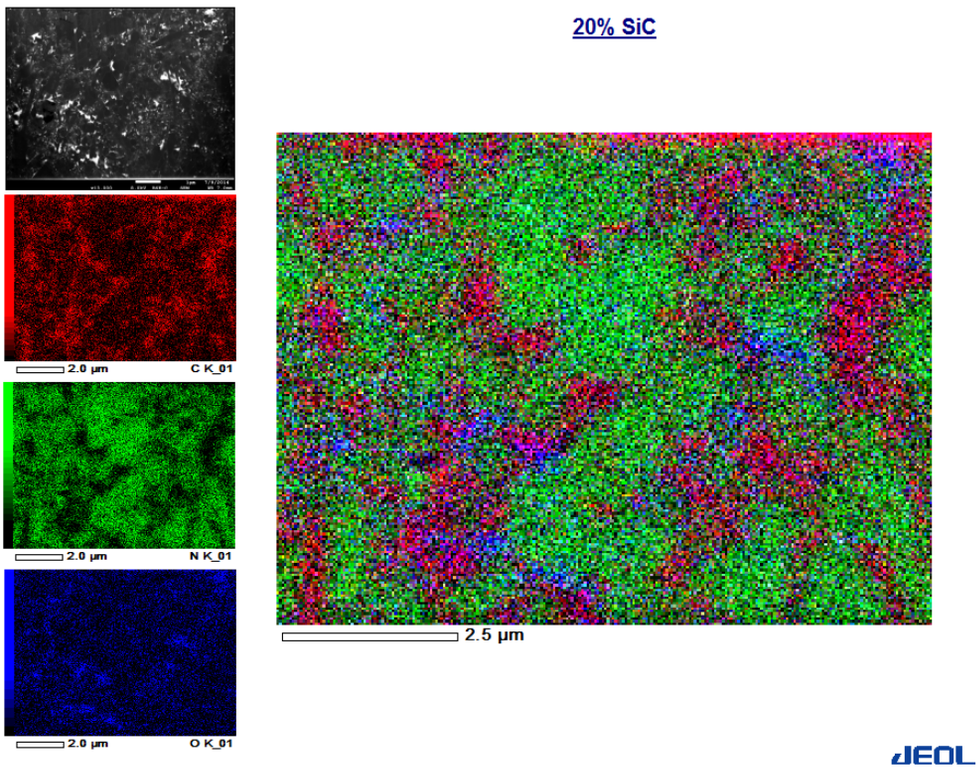

Figure 6.12 EDS Map of HP20 prepared by FIB. Left images from top to bottom are: BEI image, C map, N map, and O map. Right image is an RGB overlay of C,N and O.

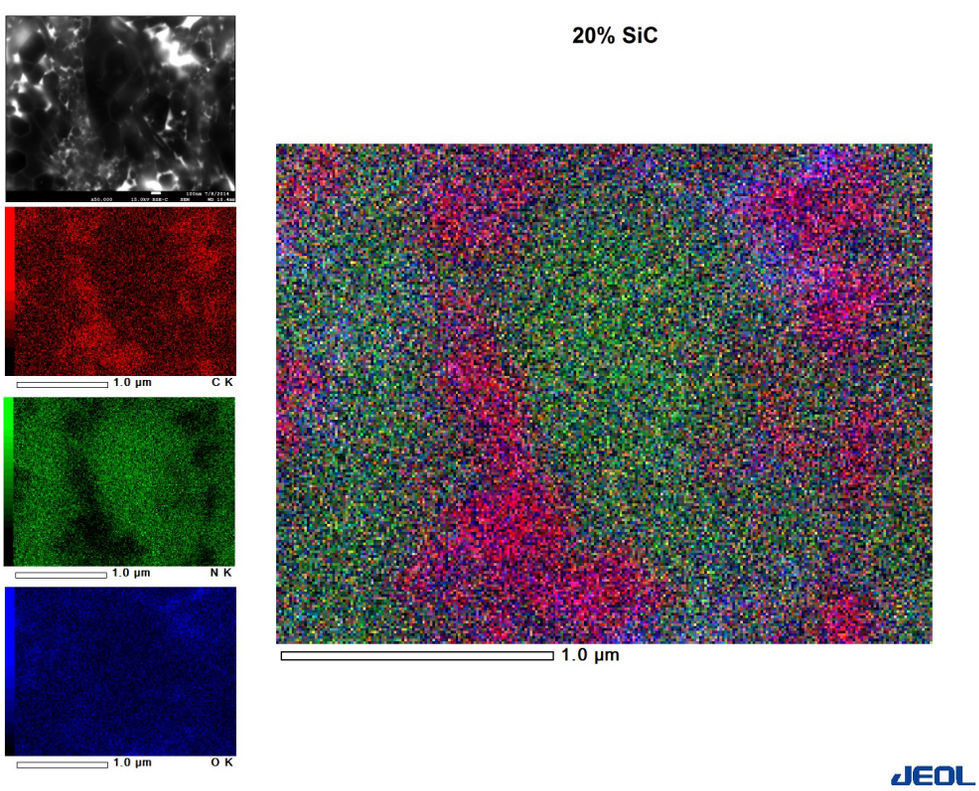

Figure 6.13 Higher magnification EDS map of HP20. Left images from top to bottom are: BEI image, C map, N map, and O map. Right image is an RGB overlay of C,N and O.

Using the EDS mapping and the BEI images it can be concluded that there are 5 distinct microstructural features that should be characterized (Figure 6.14):

1. Intra-granular SiC Grains (size and distribution, number density)
2. Inter-granular SiC Grains (size and distribution, number density)
3. Si_3N_4 Grains (grains size and aspect ratio)
4. Thin Lutetium Silicate Grain Boundaries (thickness, do all boundaries have liquid phase)
5. Lutetium Silicate glassy "pockets" (Volume fraction, size and distribution)

The Intra-granular SiC phase is difficult to see in Figure 6.14, but the red arrows for feature 1 point to very light white dots within the black Si_3N_4 grains. Previous reports have shown that many times an amorphous oxide phase remains at the Intra-granular SiC and Si_3N_4 interface.[11,24] This is why it is possible to observe these light white particles as they have a lutetium silicate phase at the interface. TEM images shown later in this section will confirm the presence of Intra-granular SiC. These five microstructural features can be quantitatively characterized with a combination of SEM and TEM techniques, which include: STEM EELS to observe and quantify features 1 and 2 in the list above, plasma etching followed by SEI imaging for feature No. 3, HRTEM for feature No. 4, and BEI imaging for feature No. 5.

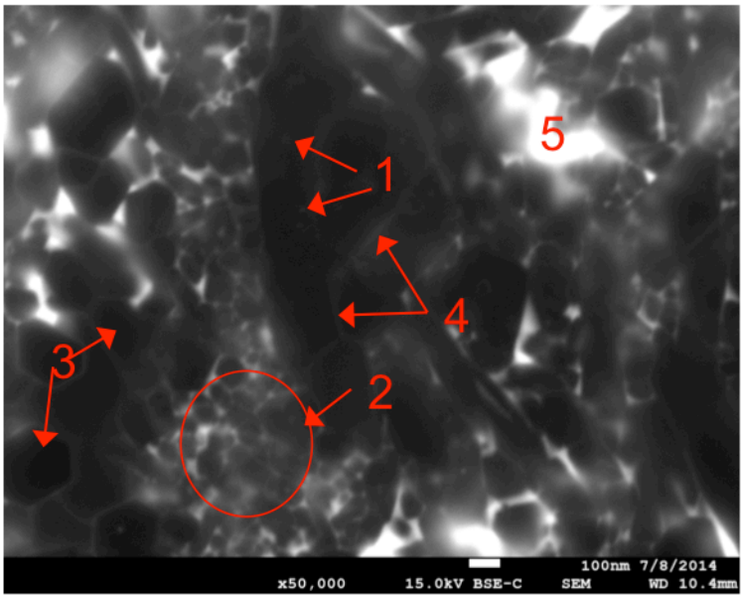

Figure 6.14 BEI image of HP20 showing 5 distinct microstructural features. 1) Intra-granular SiC, 2) Inter-granular SiC, 3) Si_3N_4, 4) Lutetium Silicate Grain Boundary, 5) Lutetium Silicate Glassy "pools".

Figure 6.15 are the SEI images of the polished and plasma etched samples. During plasma etching the Si_3N_4 phase etches much faster than the SiC and the grain boundary phases. The dark grains represent the Si3N4 phase, the gray regions are the SiC phase and the white regions are the lutetium silicate phases. The Si_3N_4 phase of these images are quite clear with the human eye; however, due to the complex nature of these images, it is very difficult to process these images for grain size analysis. Even HP0, which has good contrast, was difficult to try and perform grain size analysis. Figure 6.16 shows a binary image of HP0 processed with ImageJ (U. S. National Institutes of Health, Bethesda, Maryland, USA, http://imagej.nih.gov/ij/). In order to process grain size analysis, each individual grain cannot connect to its neighboring grain. As can be seen it would be necessary to outline each individual grain by hand or use a more powerful image processing program in order to perform grain size analysis. Even through quantitative analysis of the Si_3N_4 is not possible for this current report, qualitatively it can be seen that there is a change in grain size and morphology with increasing SiC content. HP0 has a mixture of large acicular grains along with fine equiaxed grains, which is typical among hot pressed Si_3N_4 ceramics. With the addition of SiC, the microstructure becomes refined displaying finer grain sizes. The acicular β-Si_3N_4 are still present, however, they do not appear to be as frequent. The finer grain microstructures are due to the grain boundary pinning of Si_3N_4 growing into clusters of SiC grains and halting its grain growth. As the SiC content increases from HP5 to HP20 there is a decrease in the amount of acicular grains visible for HP30, no acicular grains are observed. Also in HP30, the SiC phase has percolated through the structure.

The lutetium silicate "pockets" can easily be imaged using BEI mode. Backscatter electrons imaging shows contrast in composition base on the atomic number of the species in the material. Lutetium has a much larger atomic number (74) than C(6), N(7), O(8) or Si(14) and can be easily detected in BEI mode. Figure 6.17 shows the BEI images of the hot pressed

samples. The contrast and brightness of these images were stretched to get a black and white image and also to hide the thin grain boundary regions so that only grain boundary "pocket" regions are imaged.

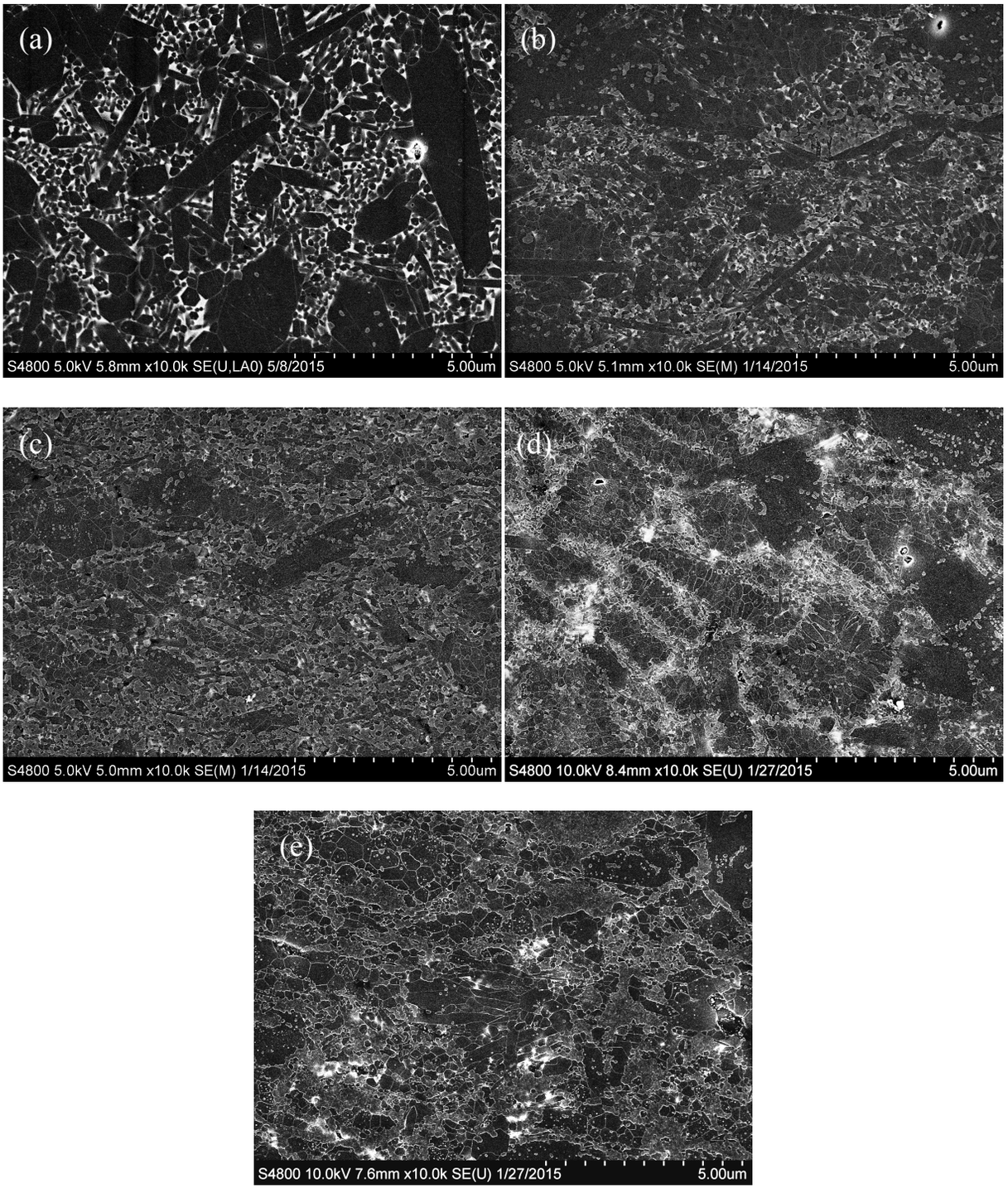

Figure 6.15 SEI images of plasma etched (CF_4/O_2 gas) a) HP0, b) HP5, c) HP10, d) HP20, and e) HP30.

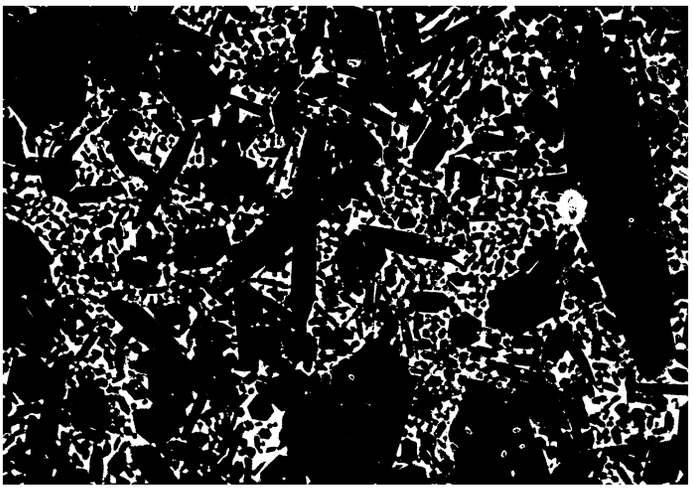

Figure 6.16 Binary image of HP0.

Based on the binary image analysis of the BEI images, the area fraction of the oxide phases were calculated for each series. Areas that measured <0.002 μm^2 were excluded. Figure 6.18 shows the calculated area fraction of the grain boundary phase "pockets" vs. vol. % SiC. There is a clear decrease in area fraction of the lutetium silicate phases with an increase in SiC content, which plateaus to a minimum area fraction of ~2% at 10 vol.% SiC. This is an indication that there is a reduction in the intergranular oxide phase with an increase in SiC content. Another indication that there is a reduction in the intergranular oxide phase is the change in crystalline phase observed from the XRD patterns (Figure 6.10). As stated previously, HP0 has crystalline phases of Si_2N_2O and $Lu_2Si_2O_7$ and the remaining samples that contain SiC have $Lu_4Si_2O_7N_4$. This indicates that there is an increase in the Lu:Si ratio, which can be caused by a reduction in the silicon content.

Because there appears to be a decrease of the intergranular phase, it is necessary to consider the reactions that can occur, which would lead to a consumption of the intergranular phase. Herrmann *et al.* considered potential gasses that can form at the temperatures and pressures and temperatures that Si_3N_4/SiC composite ceramics are processed.[43] The main gasses that can form are CO and SiO. In considering these gases and SiO_2 as the active component, the principal chemical reactions can be described by:

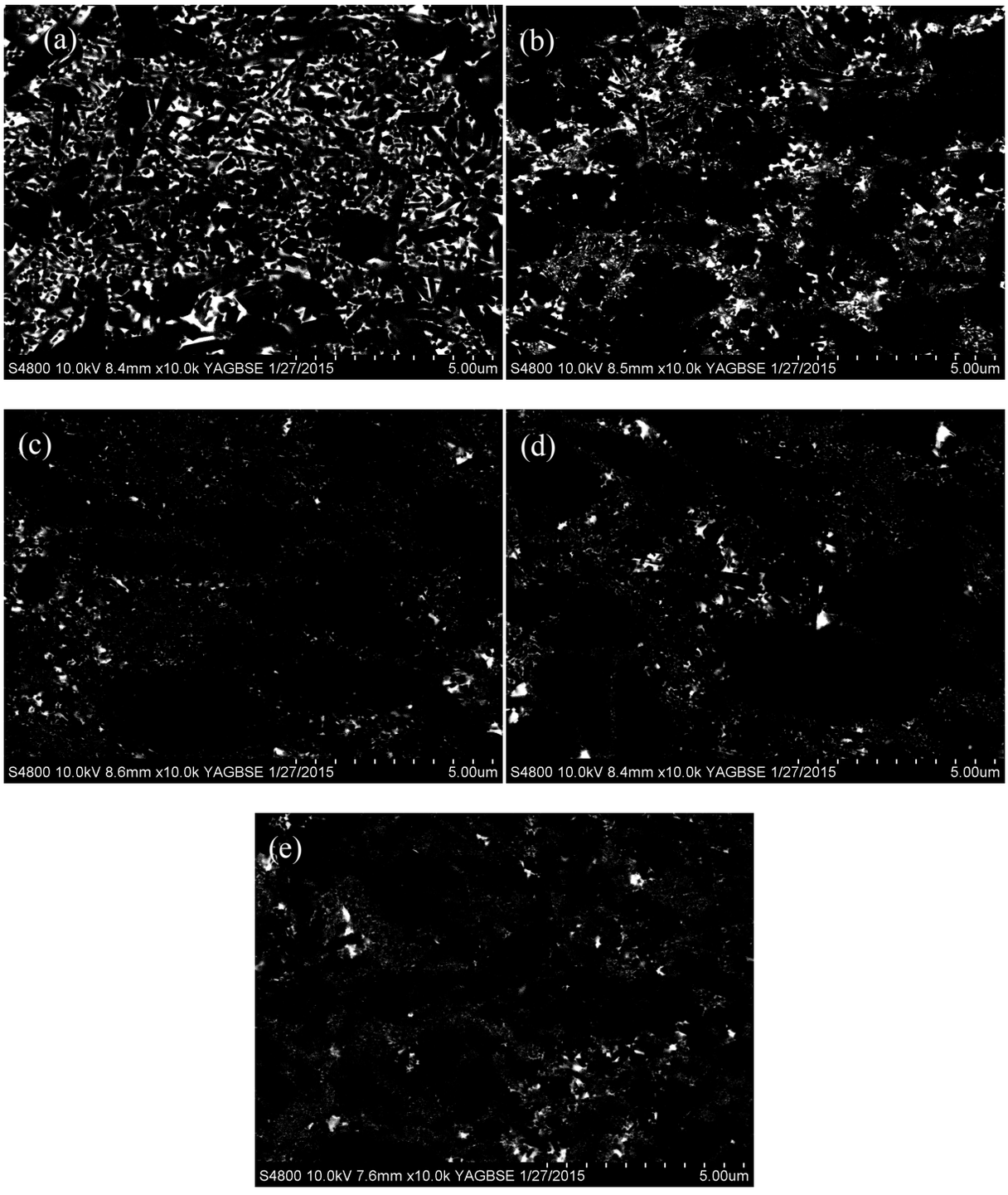

Figure 6.17 BEI images of a) HP0, b) HP5, c) HP10, d) HP20, and e) HP30.

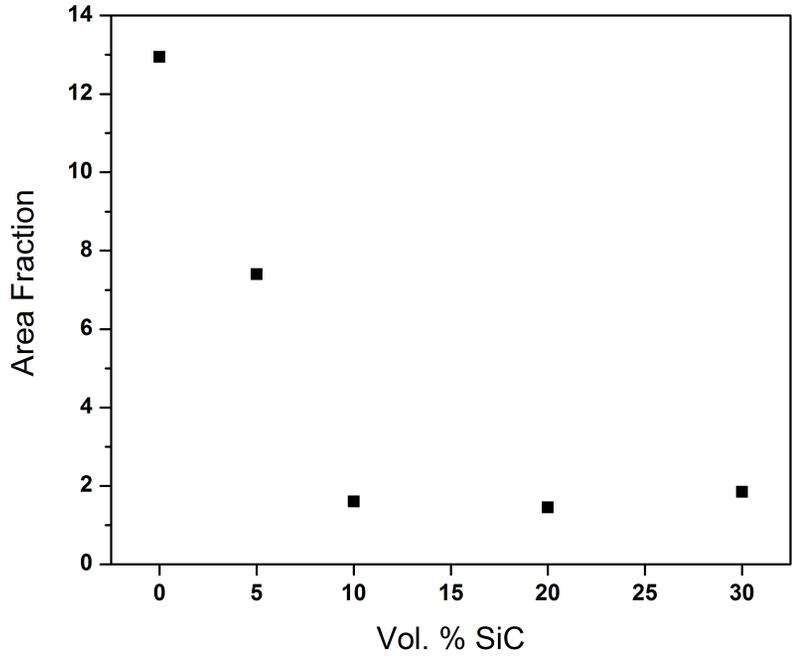

Figure 6.18 Area fraction of oxide phase for varying vol.% of SiC of the Hot Pressed samples.

$$2SiC(s) + SiO_2(l) + 2N_2(g) \rightarrow Si_3N_4(s) + 2CO(g) \quad \text{Eq. 6.1}$$

$$Si_3N_4(s) + 3SiO_2(l) \rightarrow 6SiO(g) + 2N_2(g) \quad \text{Eq. 6.2}$$

$$SiC(s) + 2SiO_2(l) \rightarrow 3SiO(g) + CO(g) \quad \text{Eq. 6.3}$$

These reactions can result in a consumption of the glass phase during processing which would lead to a higher Lu:Si ratio. However, Herrmann *et al.* explained that at the temperatures and pressures that the nanocomposites are processed at that these reactions are minimal. Also, if these reactions were dominant towards the consumption of glass phase than the HP0 sample would also likely have formed the $Lu_4Si_2O_7N_4$ phase. The other alternative is that the glass phase is reacting with free carbon through a carbothermal reduction

$$SiO_2(s,l) + 3C(s) \rightarrow SiC(s) + CO(g) \quad \text{(Eq. 6.4)}$$

It was mentioned in Section 2.3 that free carbon would react with Si_3N_4 to form SiC (Eq. 2.9); however, it is likely that Eq. 6.4 is occurring as well. This would explain the decrease in the

intergranular phase as well the increase in Lu:Si ratio of the intergranular phase. The increase in carbon content of the SiCN powders causes an increase in the amount of free carbon phase resulting in more consumption of the intergranular glassy phase. The consumption of SiO_2 in the intergranular phase would lead to an increase in the Lu:Si ratio, which would cause the formation of the $Lu_4Si_2O_7N_4$ phase. Elemental analysis of the powders and sintered specimens could confirm these deductions. A decrease in oxygen content after processing would indicate a consumption of the intergranular phase. It would also indicate if there is a difference in oxygen content (thus a difference in SiO_2) of the SiCN powders prior to hot pressing.

Besides the area fraction of the intergranular phase, the size of the lutetium silicate "pockets" was calculated. Figure 6.19 shows a normal distribution chart of the lutetium silicate "pockets" acquired from the BEI images. No clear distinction between the 5 samples is noted. One note is that the majority of the lutetium silicate "pockets" are $<0.1\ \mu m^2$. It should be noted that the intergranular phase analysis was conducted on 2 BEI images per series ($\sim 234\ \mu m^2$). The larger lutetium silicate pockets ($>0.1\ \mu m^2$) are of more interest as these large pockets can act as flaw sites as well as areas where flow can occur during high temperature testing. As shown in Figure 6.19, there are very few of these large "pockets" but "pockets" as large as $0.5\ \mu m^2$ were observed. Additional images should be acquired to have more quantitative information on the large ($>0.1\ \mu m^2$) lutetium silicate "pockets".

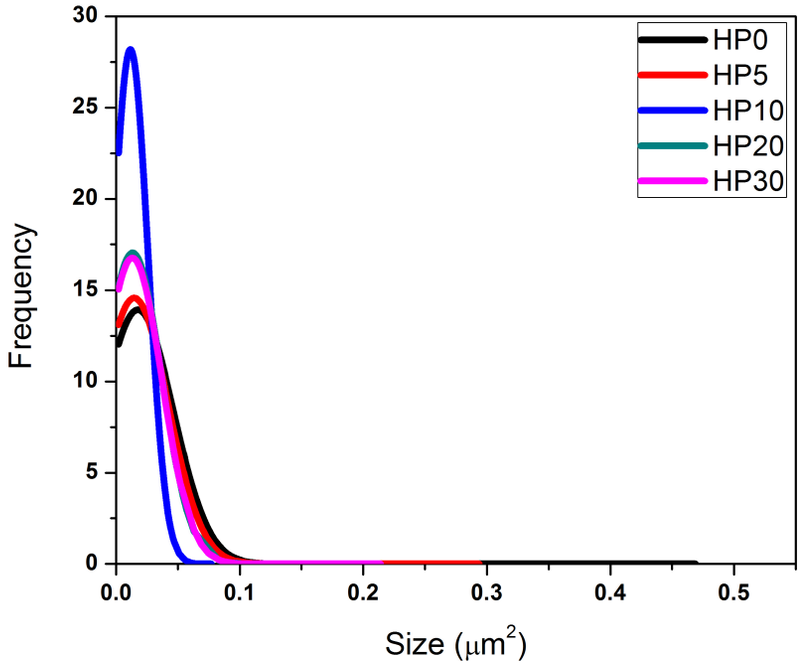

Figure 6.19 Normal distributions of the size of oxide pockets of the various Hot Pressed samples.

SEM imaging has revealed two of the microstructural features (Si_3N_4 grains and lutetium silicate "pockets) that need to be investigated. These imaging techniques have difficulty distinguishing the SiC grains. STEM-EELS is an ideal technique for distinguishing these SiC grains as it has booth high spatial and energy resolution. Figure 6.20 shows STEM images of the SiC containing hot pressed samples. STEM imaging shows an excellent high-resolution image that clearly views each individual grain in the image; however, it is still not possible to distinguish between the Si_3N_4 and SiC grains.

With the aid of a GIF camera an EELS spectrum can be acquired from a STEM image. EELS measure the change in kinetic energy of an electron after it has inelastically interacted with a specimen. This allows for very high-energy resolution (~1eV), which can give chemical as well as structural (type of bonding) information of the material. The combination of the high spatial and energy resolution can distinguish between the Si_3N_4 and SiC grains.

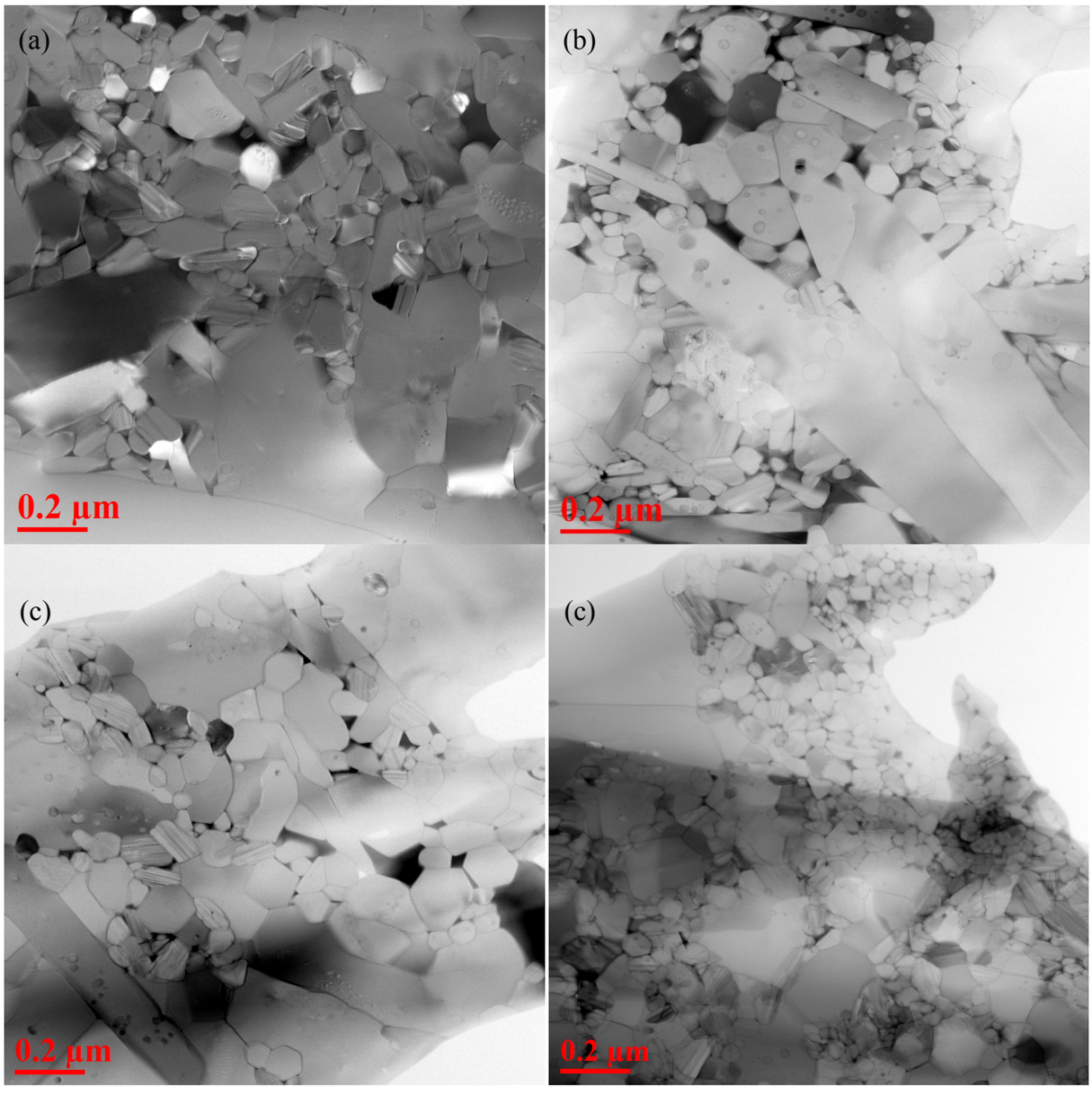

Figure 6.20 STEM images of (a) HP5, (b) HP10, (c) HP20 and (d) HP30.

Figure 6.21 shows an example of distinguishing SiC grains using STEM-EELS. The EELS spectrum (right) corresponds to the particles in the STEM image (left) that the arrows point to. The top two spectrums are examples of intra-granular SiC, which are represented by small circles within the larger grains. The spectrum clearly shows both carbon (284 eV) and nitrogen (402 eV) peaks for the small (~10 nm) intra-granular grains. This is because the electron beam passes through the sample, which is ~50 nm thick, therefore, both carbon and nitrogen energy loss electrons are measured. The bottom spectrum is an example of an inter-

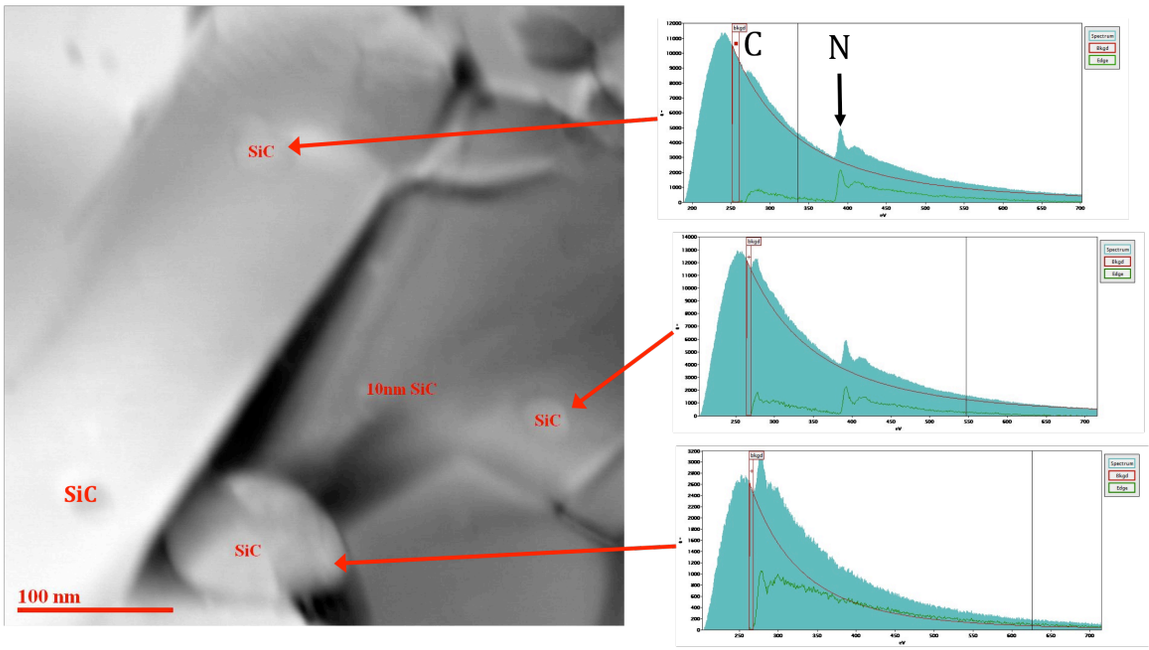

Figure 6.21 STEM image of HP0 (left) with representative EELS spectrum (right) of intra- and inter-granular SiC.

granular, which only shows the carbon peak. The silicon peak does appear because the silicon jump ratio occurs at 99 eV and the spectrums above show an energy loss range of 220 – 700 eV.

Another technique to image the SiC grains is by using Energy-Filtered TEM (EFTEM) imaging. This technique also utilizes the energy loss electrons; however, rather than acquiring a spectrum from a signal a probe point, EFTEM acquires specified energy loss electrons from an area, essentially creating an elemental map. Figure 6.22 and Figure 6.23 show EFTEM maps of an intra-granular (Figure 6.22) and an inter-granular (Figure 6.23) SiC grains. These images show a nice visual representation of the different phases present in these nanocomposites; although, this technique is not efficient for quantifying the grain size distribution. The EFTEM images shown are the lowest magnifications that can be taken in EFTEM mode. Also these images take many hours to acquire. The use of STEM-EELS can be used to identify enough SiC grains and their location for a statistical analysis of their size distribution.

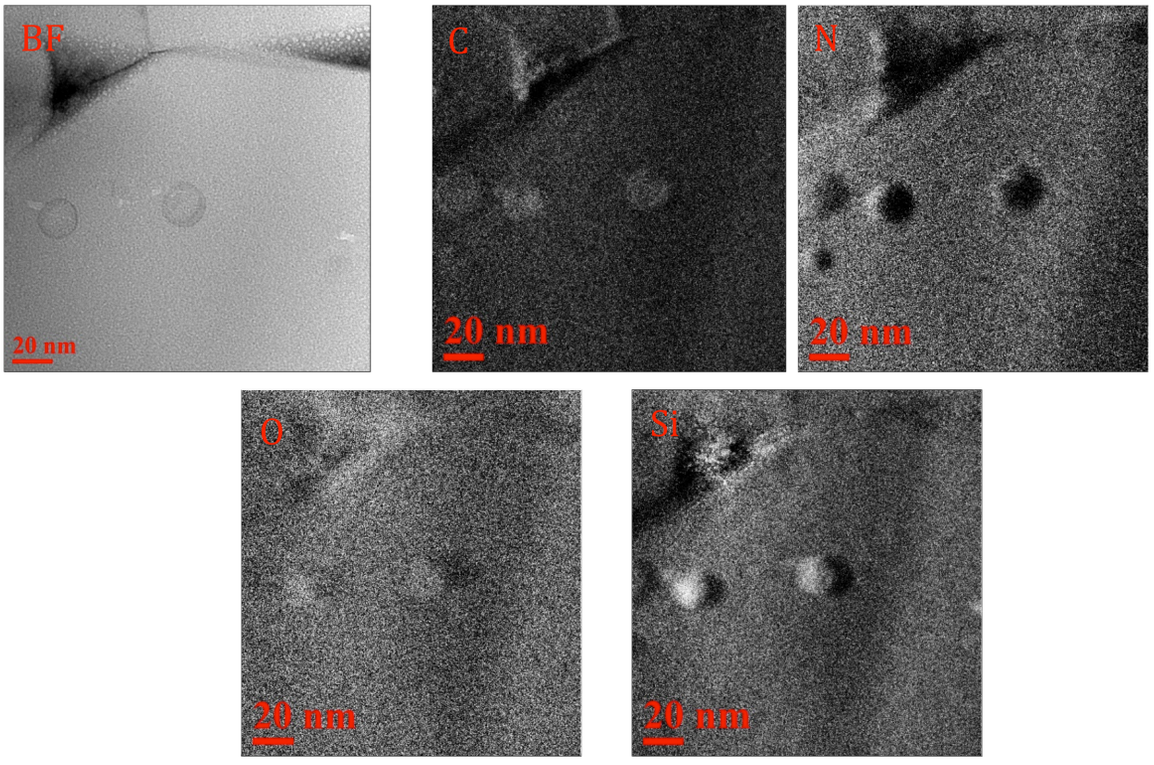

Figure 6.22, EFTEM image of intra-granular SiC displaying bright field image (BF), carbon map (C), nitrogen map (N), oxygen map (O) and silicon map (Si).

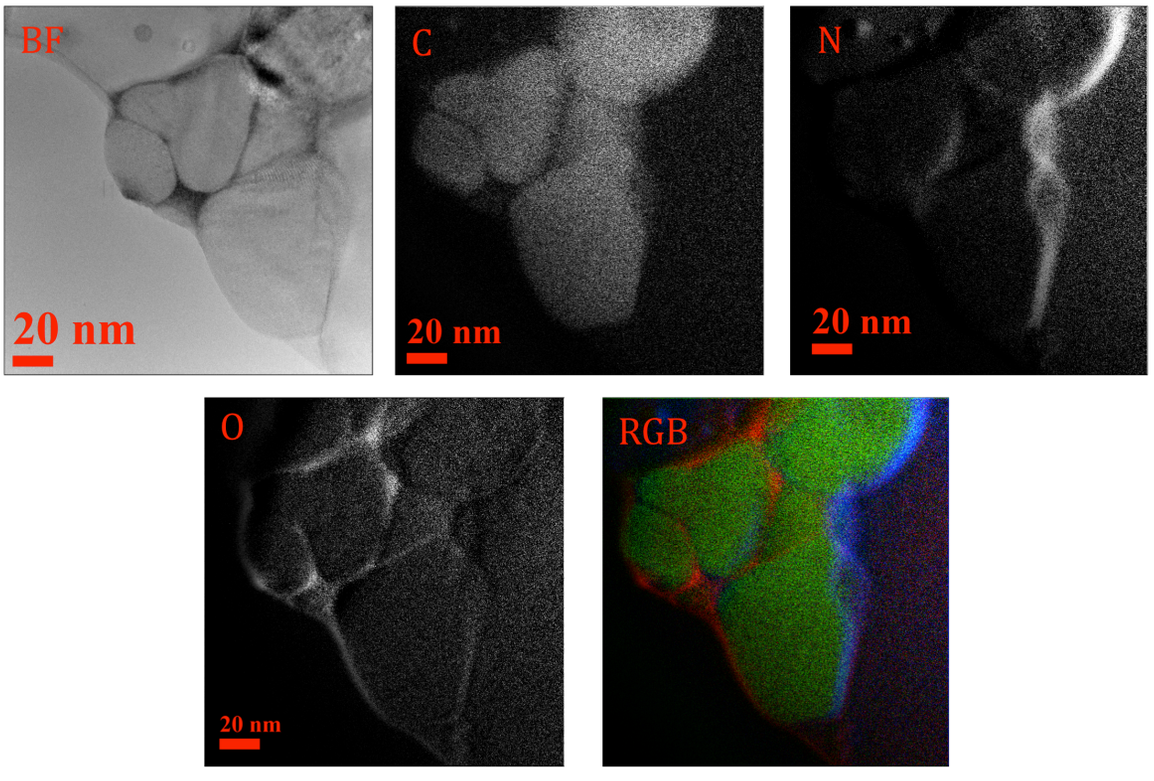

Figure 6.23 EFTEM image of inter-granular SiC displaying bright field image (BF), carbon map (C), nitrogen map (N), oxygen map (O), and a red, blue green overlay of oxygen, nitrogen and carbon respectively (RGB).

Figure 6.24 describes the process in which the SiC grain size analysis was performed. A low magnification image (upper left) was taken and used for marking the SiC grains. This image was broken down into 9 frames where high magnification images were take for each frame (upper right). For each frame the beam was manually moved around the sample looking for carbon peaks from the EELS spectrum (bottom) to identify each SiC grain. After identifying the SiC grains, post-image analysis software was used to measure each individual grain by drawing a line over each grain.

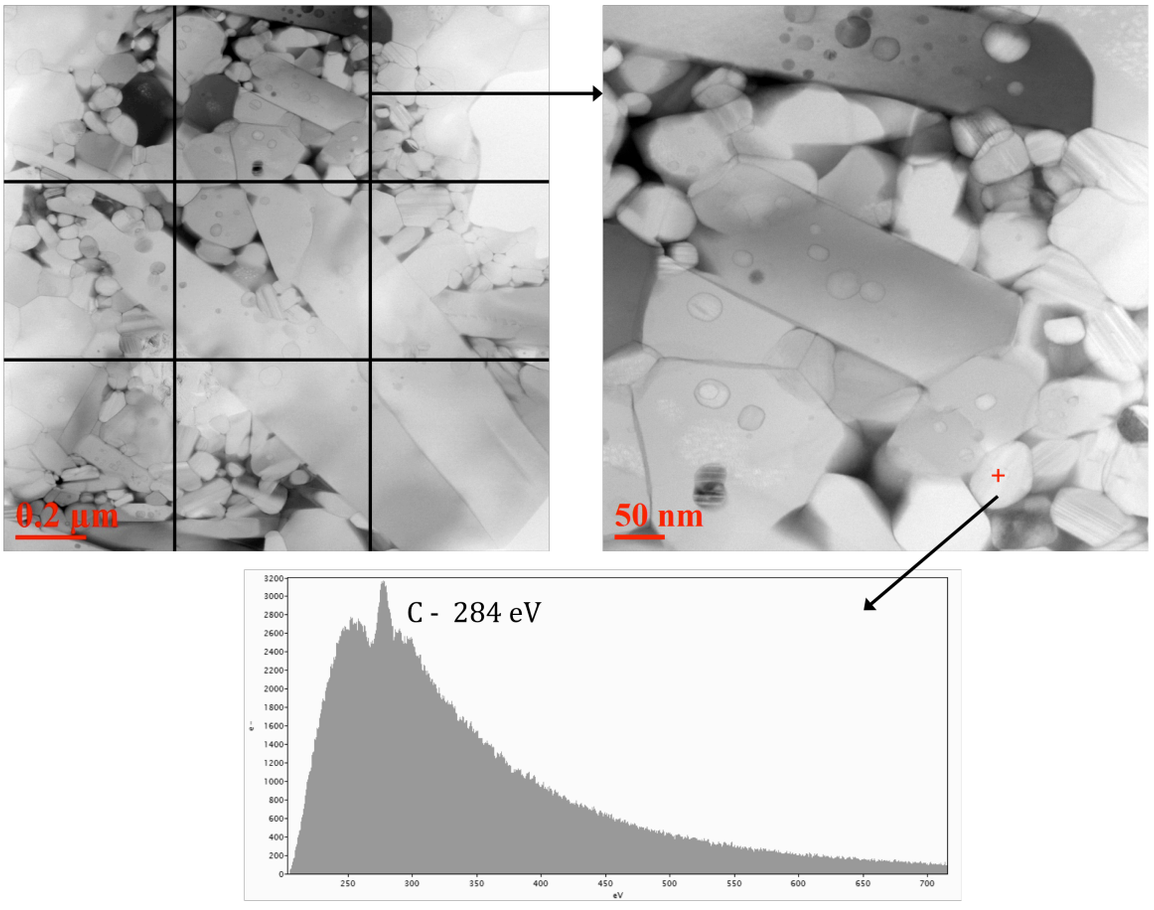

Figure 6.24 Representation of the process to acquire quantitative SiC grain size analysis. (Upper left) STEM image of area to be analyzed, which is then broken down into 9 frames to zoom in. (Upper right) STEM image of zoomed in frame from left image where the beam can be moved around the image (represented by red + sign) and the EELS spectrum is observed.

The results for the SiC grain size analysis are displayed in Figure 6.25. The intragranular phase for all of the hot pressed samples are finer than the inter-granular phase. The intra-granular

SiC also has a narrow distribution. This intuitively makes sense as the intra-granular phase forms due to Si_3N_4 grains growing around the SiC particles; therefore, the SiC grains become isolated and are unable to achieve any grain growth. The inter-granular grains seem to have a trend where there is a decrease in grain size with increasing SiC content. It is unclear why this trend occurs. In addition to grains size distribution, the intra/inter-granular count ratio is displayed in Table 6.5. For HP5, HP10 and HP20 there are more counts of the intra-granular, but for HP30 there are a larger amount of inter-granular grains. This is due to the percolation of the SiC network of HP30. There are fewer isolated grains for the Si_3N_4 to grow around but instead grain growth is halted due to grain boundary pinning against the interconnected SiC phase.

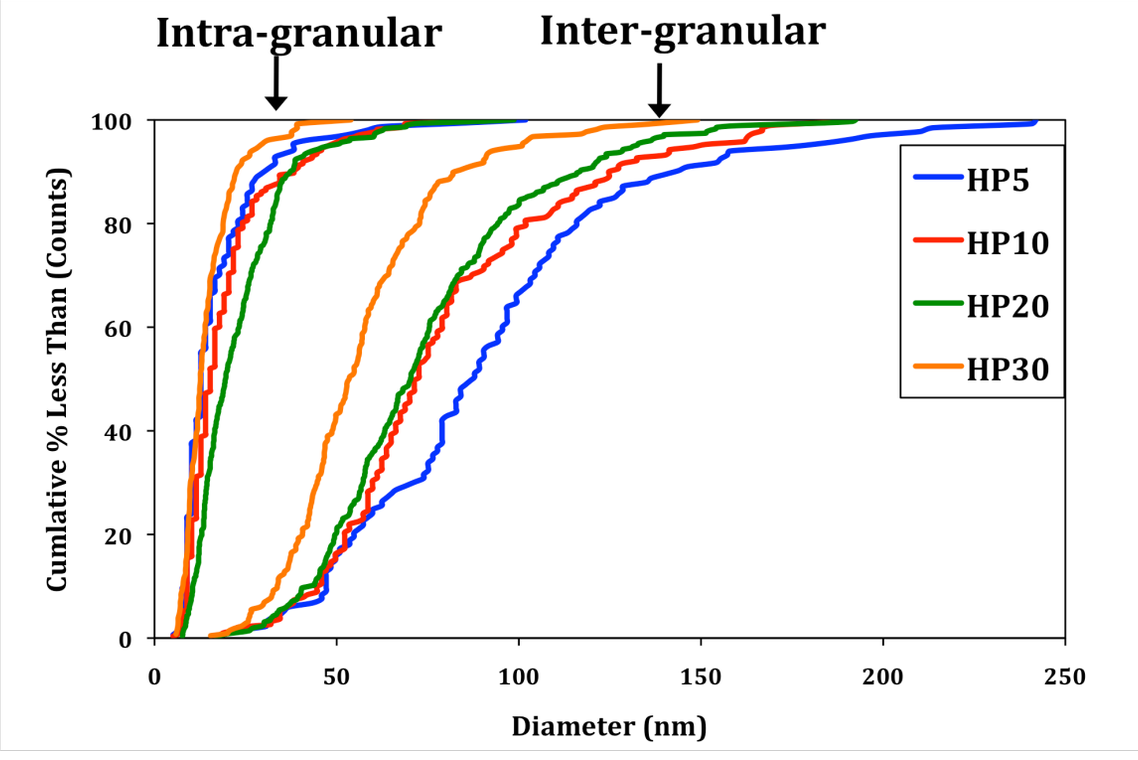

Figure 6.25 SiC grain size distribution in hot pressed samples.

Table 6.5 Table displaying the number of grains counted as well as the Intra/Inter-granular SiC count ratio.

	Intra	Inter	Intra/Inter
HP5	154	133	1.16
HP10	273	191	1.43
HP20	351	302	1.16
HP30	129	218	0.59

It should be noted that when investigating HP0, SiC grains were identified in the material as seen in Figure 6.21. However, their numbers were so few that the XRD pattern could not identify SiC for this sample. It was expected that some SiC would form in the HP0 sample from the results of the controlled ammonia pyrolysis studies (Section 5.4.1). From those studies the NH_3 substitution reaction proceeded enough where no SiC was seen in the XRD patterns; however, Raman spectroscopy revealed that free carbon still existed. This explains why SiC existed in the HP0 sample. There are so few SiC grains that it was not possible to have statistical analysis of the grains size distribution.

In addition to STEM-EELS, HRTEM was conducted to observe the both the SiC phase and the intergranular grain boundary phase. Figure 6.26 shows an HRTEM image of (a) intra- and (b) inter-granular SiC grains. The boundary between intra-granular SiC and Si_3N_4 appears to be clean without an interphase. This has been seen previously that there is a characteristic orientation relationship between β-SiC and β-Si_3N_4 ([0001]-Si_3N_4//[110]-SiC and $(10\bar{1}0)$-Si_3N_4//$(1\bar{1}1)$-SiC.) where the interface has very little lattice mismatch.[11] The inter-granular SiC (g) shows that it has many interfaces including a two-grain junction with Si_3N_4 and a three-grain junction where it borders the intergranular oxide phase.

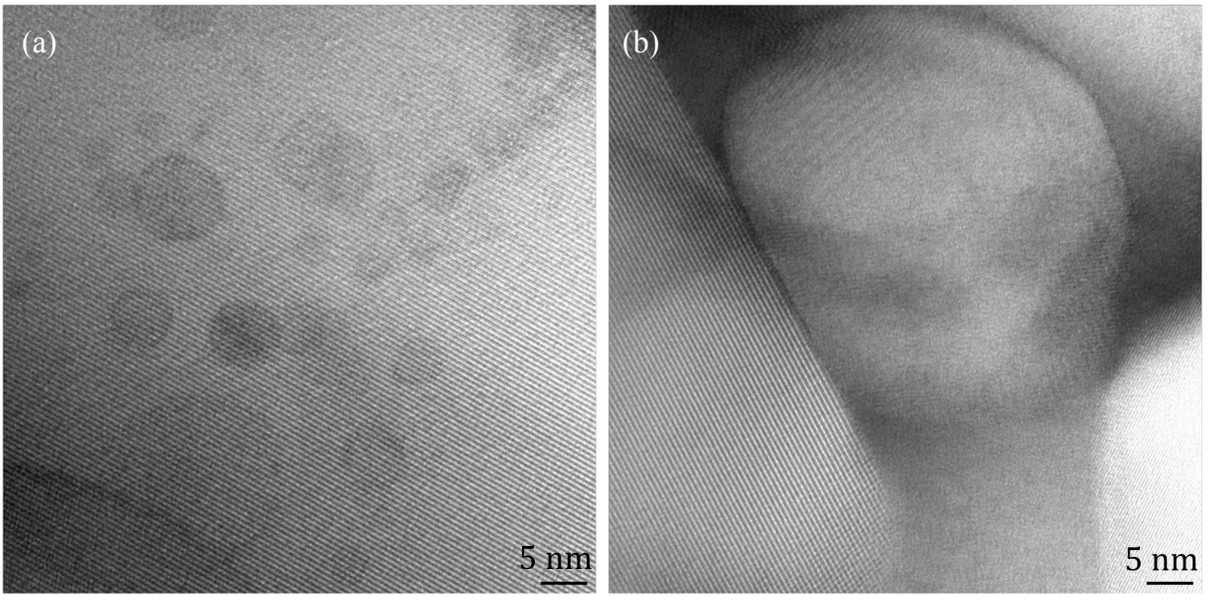

Figure 6.26 HRTEM image of HP20 showing the intra-granular (a) and inter-granular (b) SiC.

Figure 6.27 shows examples of the intergranular grain boundary phases present. The figure shows (a) a triple point intergranular oxide phase, (b) grain boundary phase with a thickness of ~1.5 nm and (c) and grain boundary with a very clean interface. These images show that there are multiple types of intergranular morphologies that occur. It is difficult to get any type of statistical quantification of these phases since HRTEM observes a very small region. These give a good qualitative representation of the type of grain boundaries present in the material.

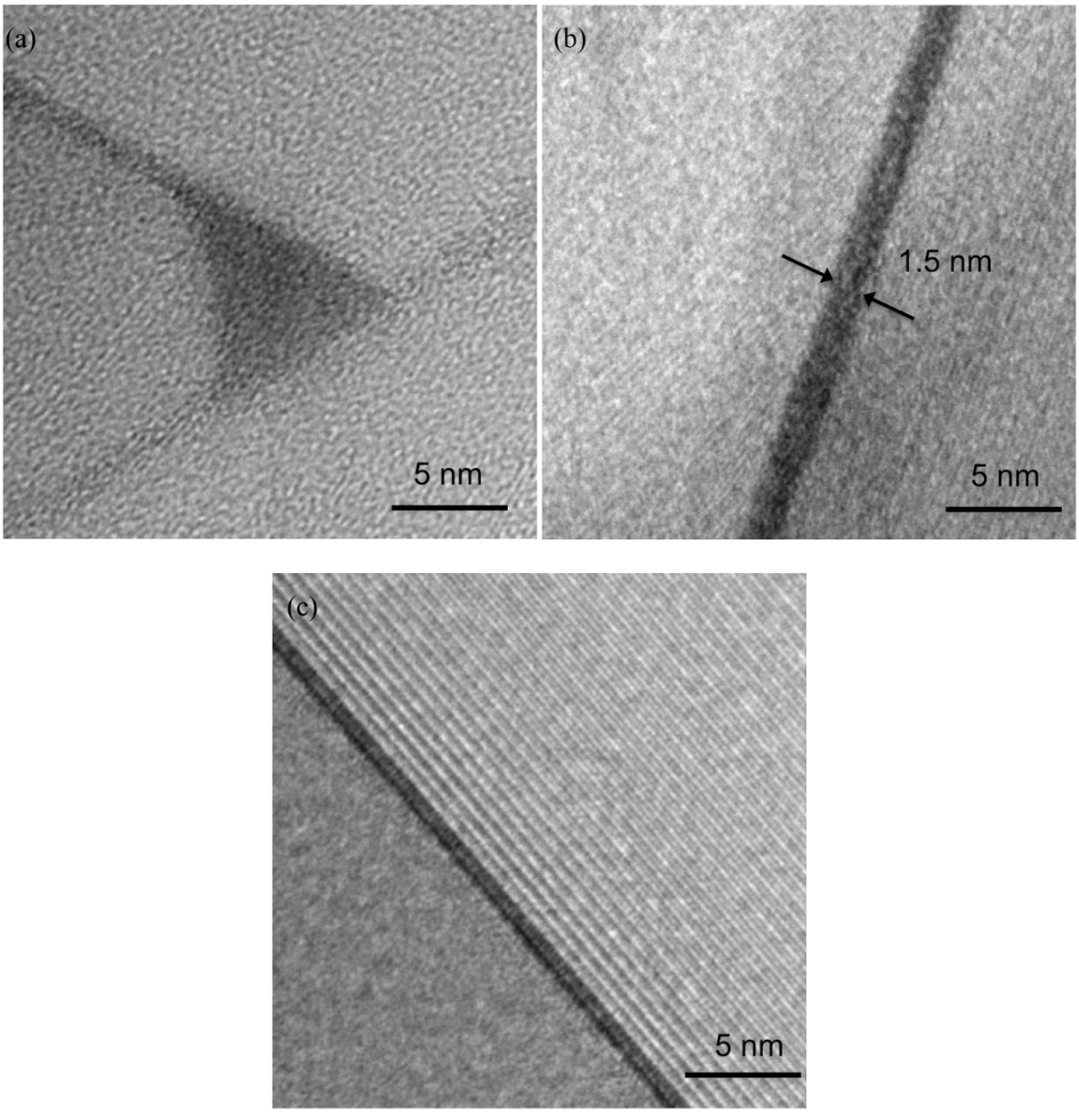

Figure 6.27 HRTEM of HP20 displaying examples of (a) three grain junction with amorphous glass phase, (b) two grain junction with 1.5 nm thick intergranular phase and (c) two grain junction with clean grain boundary.

6.3 Field Assisted Sintering

The SiCN powders used in the previous section for hot pressing were also used to create dense Si_3N_4/SiC nanocomposites using field assisted sintering (FAST). Powders were placed in a 20 mm diameter graphite die and field assisted sintered at 100 ˚C/min to 1700 ˚C for 10 min with an applied pressure of 50 MPa under vacuum with a SPS Model 10-4 (GT Advanced Technologies). The samples IDs for these specimens are reported as FAST0, FAST5, FAST10, FAST20 and FAST30. Table 6.6 displays the densities of sintered FAST samples. Their densities are somewhat lower than those of the hot pressed samples, but they are still quite high.

Table 6.6 Density measurements of field assisted sintered samples.

Sample ID	Density (g/cm^3)
FAST0	3.22
FAST5	3.29
FAST10	3.24
FAST20	3.29
FAST30	3.19

XRD results are shown in Figure 6.28. There are some significant differences in the crystalline phases of the FAST samples in comparison to the HP samples (Figure 6.10). One is the predominance of α-Si_3N_4 in the FAST samples. This indicates that the α→β was not fully completed. This is likely due to the short processing time (faster heating rate and shorter dwell time) in comparison to the hot pressing cycle. This did not allow adequate time at the elevated temperatures for the transformation to take place. Another interesting observation is the lack of lutetium silicate crystalline phases. There are a few small peaks of $Lu_4Si_2O_7N_2$ seen in FAST5 and FAST10, but none found in the other samples. Si_2N_2O is still present in the FAST0 sample as it is in the HP0 sample.

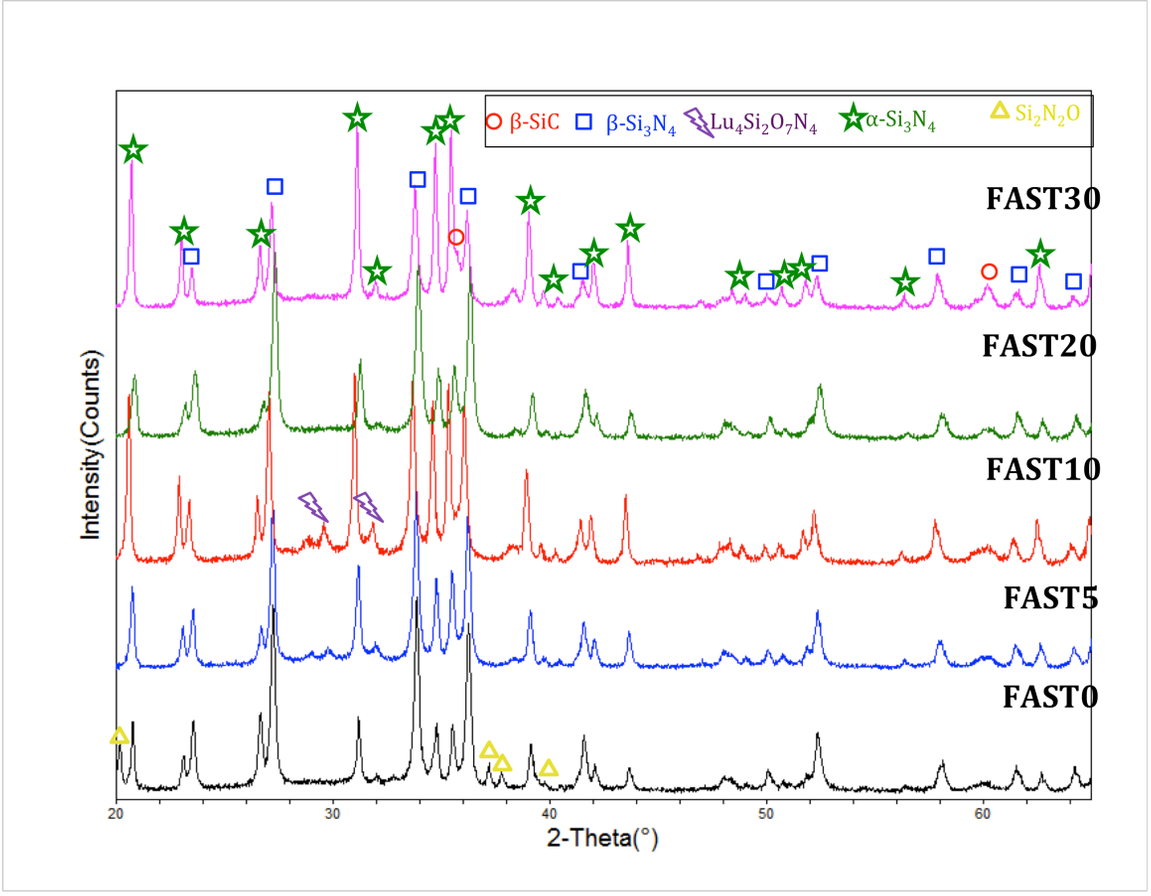

Figure 6.28 XRD patterns of field assisted sintered samples.

SEI images of plasma etched FAST samples are displayed in Figure 6.29 to reveal the Si_3N_4 phase of this material. One clear distinction of the FAST samples versus the HP samples is the very fine microstructures in the FAST samples. FAST processing tends to produce finer microstructures due to its short processing time, not allowing for significant Oswald ripening to occur. Another reason for the fine microstructures is due to the electrowetting effect that occurs due to the applied electric field during processing.[89] This causes the particle rearrangement stage of sintering to be more efficient allowing for optimal particle packing. Another interesting note from the images below are the large amount of pores in the FAST20 and FAST30 samples. These have been attributed to grain pull out due to sample preparation, which is confirmed in the TEM investigations discussed later.

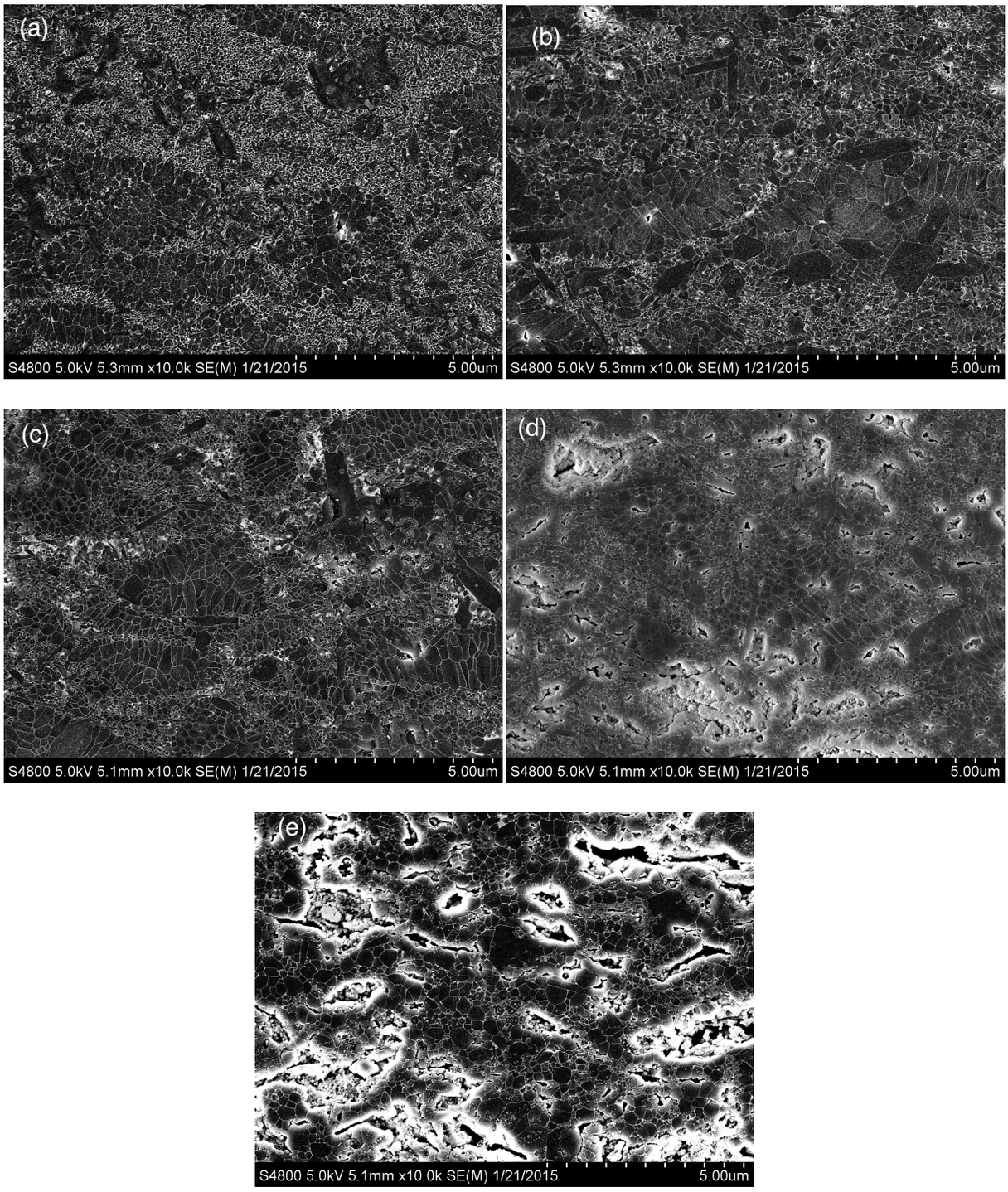

Figure 6.29 SEI images of plasma etched (CF_4/O_2 gas) a) FAST0, b) FAST5, c) FAST10, d) FAST20, and e) FAST30.

BEI images are shown in Figure 6.30. The same image analysis process used for analyzing the lutetium silicate "pockets" of the hot pressed samples was applied to the FAST samples. Figure 6.31 displays the area fraction of the lutetium silicate "pockets" as a function of

SiC content. The results show that the measured area fraction is significantly less than that of the hot pressed samples for the 0 and 5 vol.% SiC (Figure 6.18). This is not a result of the reduction in the intergranular phase, but is due to the even disbursement of the intergranular phase from the improved wetting properties of the applied electric field. An elemental analysis, particularly oxygen content, of both the hot pressed and the FAST samples would corroborate this deduction. The area fraction of the 10, 20 and 30 vol.% SiC samples are similar to that of the hot pressed samples.

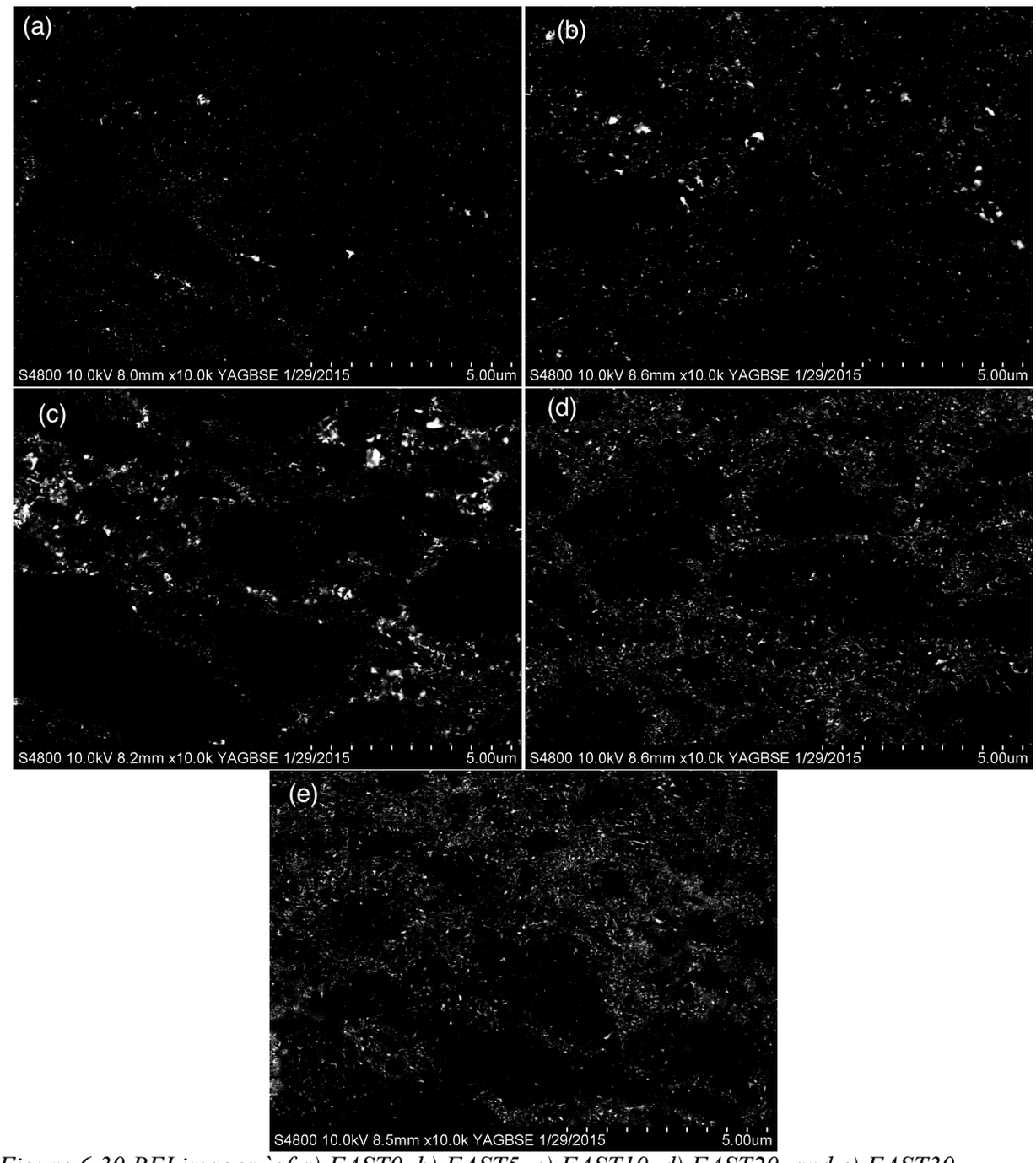

Figure 6.30 BEI images `of a) FAST0, b) FAST5, c) FAST10, d) FAST20, and e) FAST30.

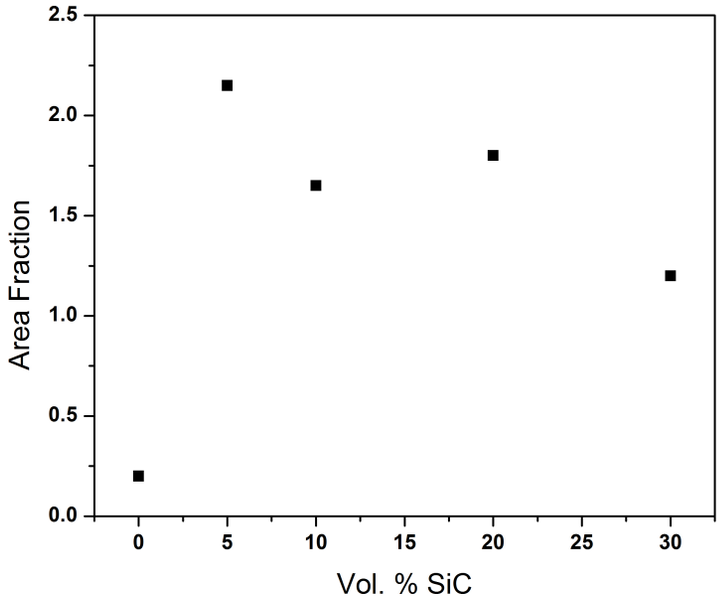

Figure 6.31 Area fraction of intergranular oxide phase as a function of vol.% SiC for the field assisted sintering samples.

The size distribution of the lutetium silicate "pockets" is displayed Figure 6.32. The majority of the lutetium silicate "pockets" are <0.05 μm^2, which is smaller than that of the hot pressed samples, which the majority were <0.1 μm^2. Again this is likely due to the electric field effect allowing an even distribution of the intergranular phase. Additional images should be acquired to have more quantitative information on the large (>0.1 μm^2) lutetium silicate "pockets" as these larger "pockets" are sites for flaws and have a significant effect on high temperature properties.

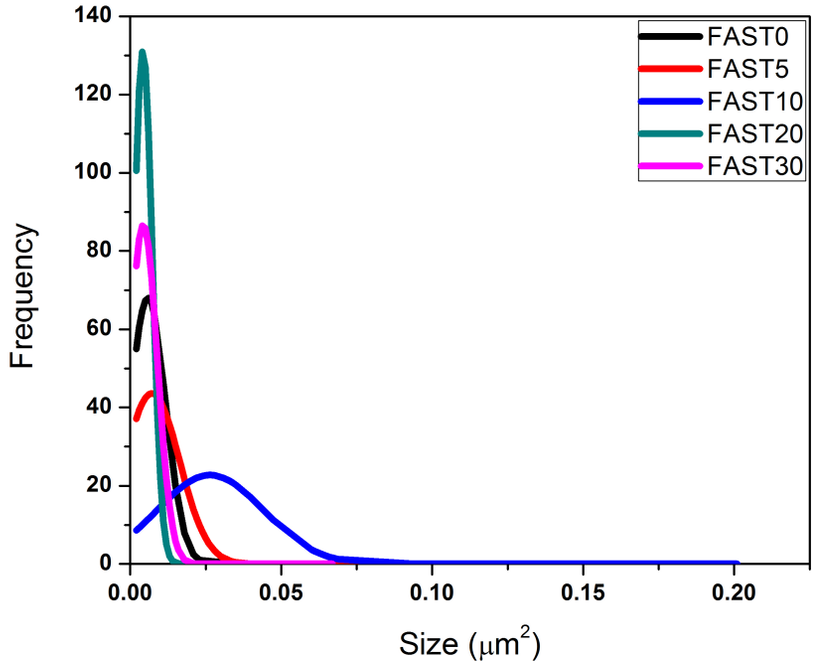

Figure 6.32 Normal distribution of the size of the lutetium silicate "pockets" for the field assisted sintering samples.

Microstructural investigation of the SiC grains was conducted using the same procedures as that described for the hot pressed samples. Figure 6.33 shows the STEM images of FAST5, FAST20 AND FAST30. The first visual difference in the FAST samples compared to the hot pressed samples is the bright white phase seen in the samples. It clearly is seen in the FAST30 samples and is present in the other two samples as well, albeit dispersed in the grain boundaries.

Figure 6.34 displays EELS spectrum of the white phase (EELS1), the grains bordering the white phase (EELS2), the large grains (EELS3) and the black phase (EELS4). The EELS data shows that the white phase does not contain silicon but only carbon. The small grains bordering the white phase are SiC with the large grains being Si_3N_4. The black phases are the lutetium silicate phase which as it contains Si, O, N and Lu but not C. (Note: EELS spectrum for Lu is not present but it was confirmed that Lu is in fact in the intergranular phase). The EELS spectrum clearly shows that free carbon exists in the FAST samples, which was not observed in the hot pressed samples. An enhanced look at the carbon jump ratio shows that the shape of the

carbon peak is different for the free carbon phase compared to the SiC phase. It is possible to observe π and π* bonds from two distinct peaks in the carbon spectrum. This also shows that the free carbon phase has some graphitic structure to it. The pores observed in the SEI images (Figure 6.29) are similar in shape as the free carbon phase observed in the STEM images. It is likely that this free carbon phase was pulled out during sample preparation which is why they are observed as pores in the SEM images.

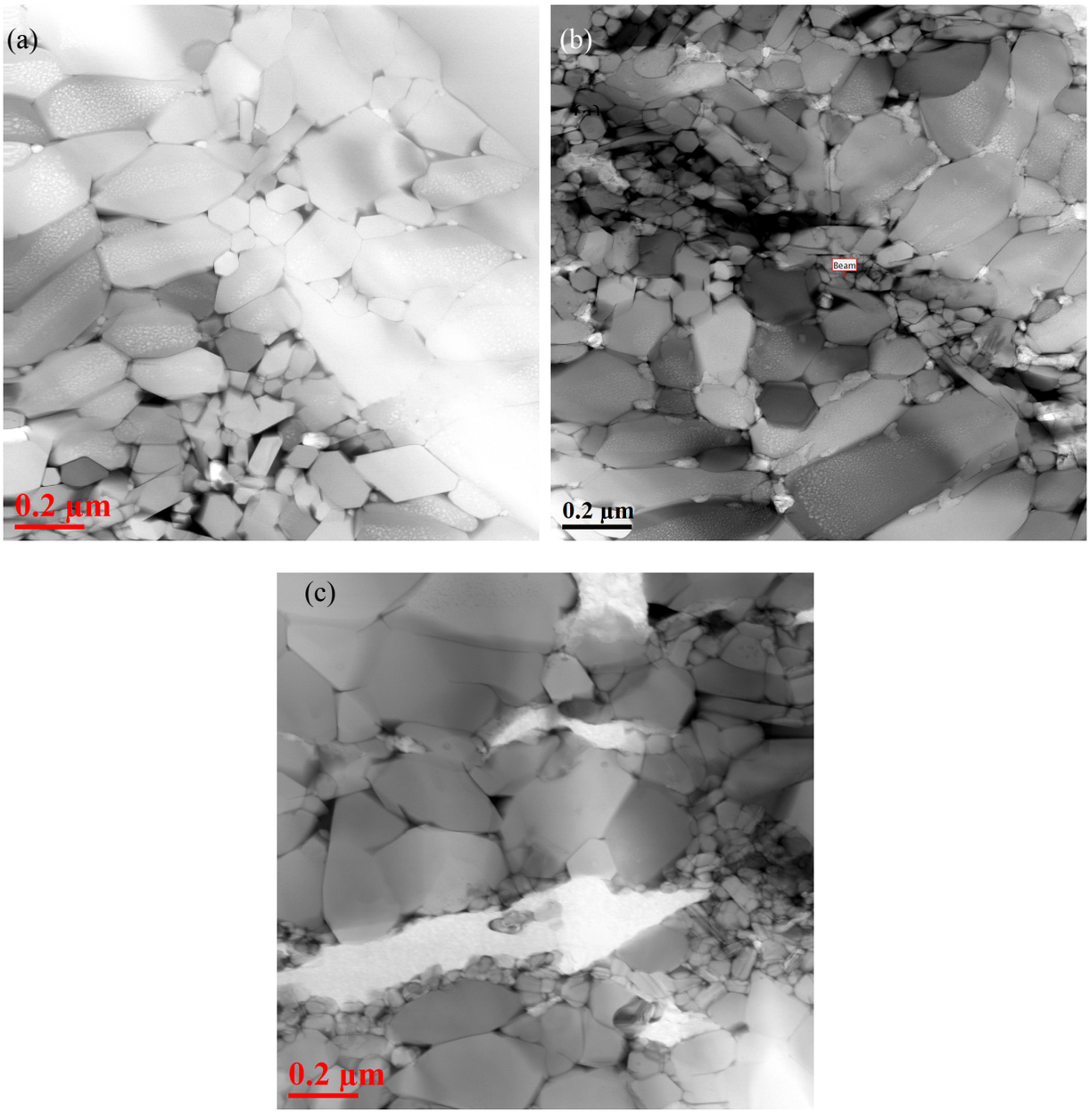

Figure 6.33 STEM images of (a) FAST5, (b) FAST20 and (c) FAST30.

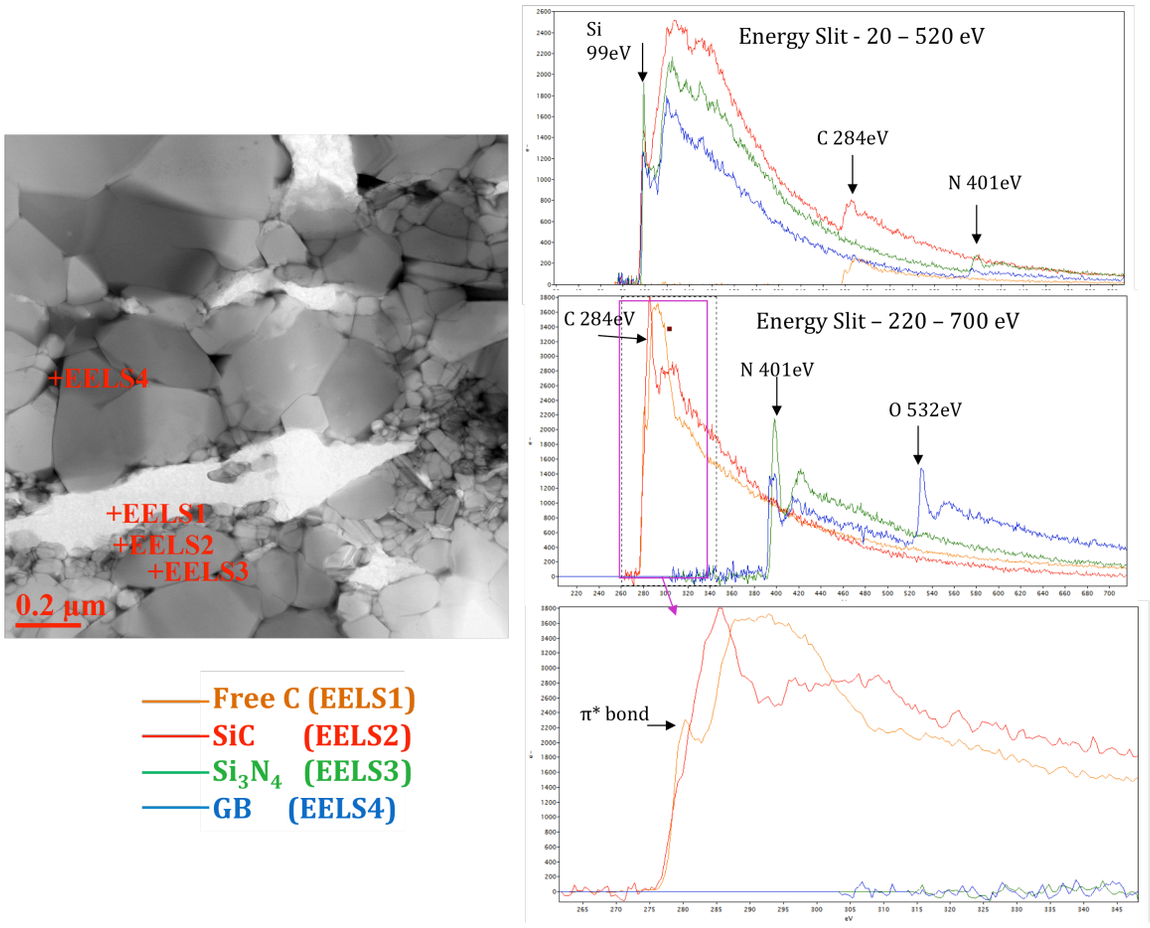

Figure 6.34 STEM image of FAST30 (left) with EELS spectrum of noted points (right).

For the FAST samples, the carbothermal reduction reactions did not fully complete as opposed to the hot pressed samples. This indicates that there is a kinetic component to this reaction. This is similar to the results seen in Section 5.4.2, where the free carbon phase remained in the samples even at 1750 ˚C for 2 hours. At 1850 ˚C the free carbon phase was not observed by Raman, so it can be assumed that the extra time and elevated temperatures helped to complete the carbothermal reaction. Another possible cause of the incomplete carbothermal reaction is the short exposure time of the crystalline Si_3N_4 with carbon. Golczewski showed that the crystallization of the amorphous SiCN phase is time dependent.[138] Because the FAST process had very short times at temperature above crystallization temperature (~12min), there

was not much time for the free carbon phase to react with the Si_3N_4 phase. This is also in agreement with the XRD patterns (Figure 6.28), which do not show the SiC phase for FAST5, FAST10 and FAST20. It should be noted that SiC does exist for these samples (as observed in the TEM investigation), there just is not a significant amount for XRD signal.

Chapter 7

Room Temperature Mechanical Testing

7.1 Hardness

Vickers microhardness results for the hot pressed and FAST samples are shown in Figure 7.1. Hardness for the FAST samples decreases with an increase in SiC content. However, due to the free carbon in the FAST samples, this result is due to an increase in free carbon as the nominal carbon content in SiCN increases. The carbon phase is very soft in comparison to SiC and Si_3N_4, which is why there is a decrease in hardness. The high hardness value for the FAST0 sample is due to the very fine microstructure that was observed. Materials with finer microstructure usually have higher hardness because of the Hall-Petch effect.[152,153] The hot pressed samples do not have any significant changes or trends with a change in SiC content. It is expected that there will be an increase in hardness since a single crystal SiC has higher hardness than a single crystal Si_3N_4. Balog *et al.* has shown that a slight increase in hardness with increasing SiC at low vol.% SiC (0 – 12%).[45] Others have reported little to no changes in hardness at high vol.% SiC (10 – 30v%).[43] Another factor that can affect the hardness is the intergranular phase. However, there have not been any repeated studies on the hardness of lutetium silicon oxide or lutetium silicon oxynitride.

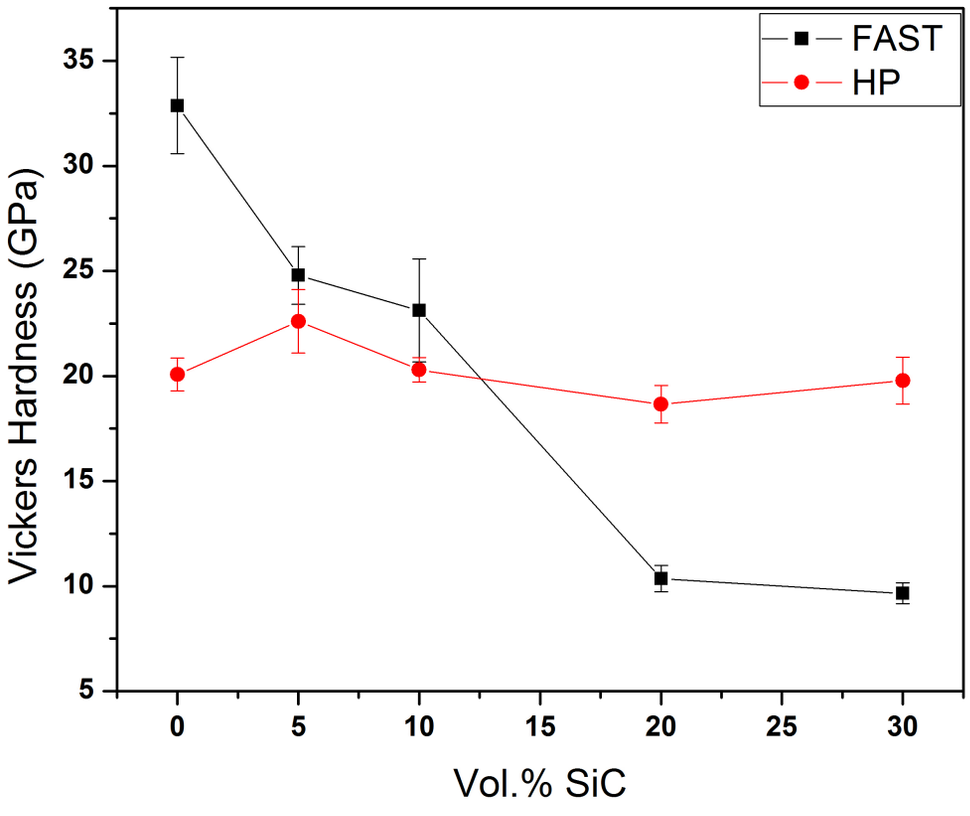

Figure 7.1 Hardness values as a function of SiC vol.% of the hot pressed (red) and FAST (black) samples. Solid lines are for visual guidance.

7.2 Fracture Toughness

Prior to testing the hot pressed samples, fracture toughness testing of a standard reference Si_3N_4 material was conducted using the SEVNB technique. SRM2100 (NC132) (obtained from NIST) was tested to show the validity of the SEVNB sample prep technique. A K_{IC} value of 4.34±0.11 MPa√m was calculated from 5 samples. This is slightly lower than the reported K_{IC}=4.57±0.11 MPa√m for SRM2100, however, the measured values are within reason, showing that this sample preparation technique is appropriate.

Fracture toughness results for the hot pressed samples are shown in Figure 7.2. HP0 and HP5 have similar K_{IC} values, but there is a decrease in K_{IC} from HP5 to HP10 to HP20. The toughness of HP30 is similar to that of HP20. This is likely due to the refined microstructures

that are observed with an increase in SiC content (Figure 6.15). The acicular $Si3N_4$ grains observed in HP0 and HP5 cause crack bridging which increases the resistance for crack growth. There are fewer of these acicular grains with increase in SiC content leading to lower toughness. Another factor that can influence the toughness is the nature and properties of the grain boundary phase. This also changes as the amount of SiC changes.

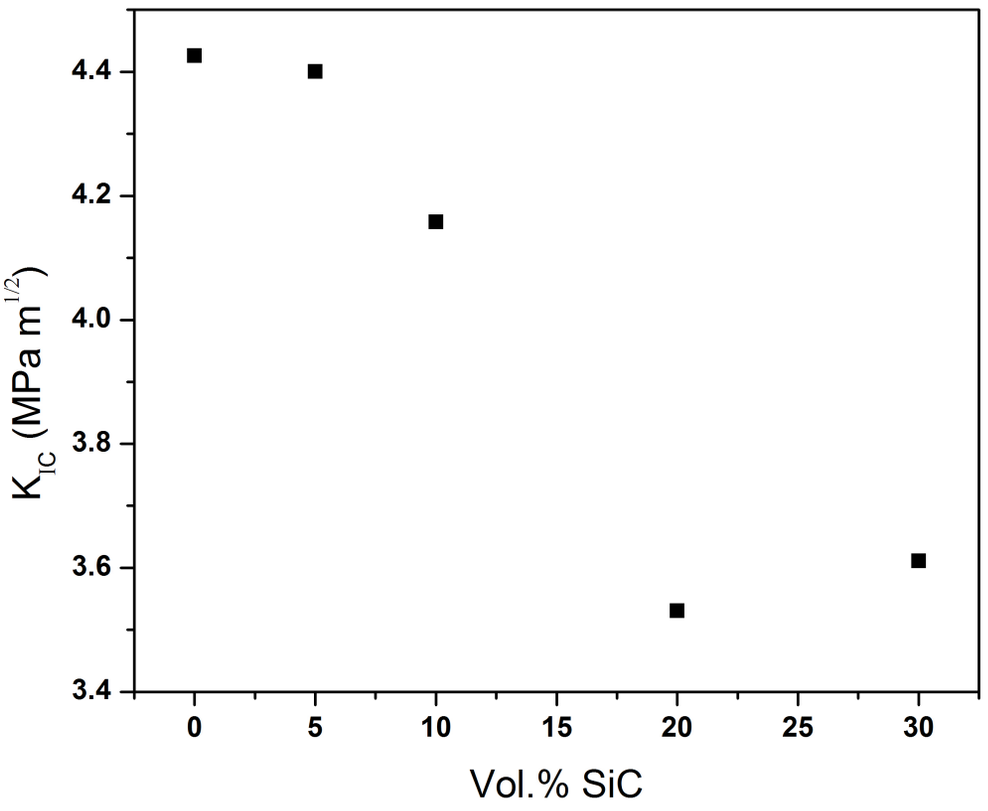

Figure 7.2 Fracture toughness as a function of vol.% SiC for the hot pressed samples.

7.3 High Temperature CTE

Measuring CTE as a function of temperature can act as an indicator for transitions that may occur in the intergranular glassy phase. Wereszczak *et al.*[122] showed that by using a dilatometer to measure the CTE in Si_3N_4 ceramics they could observe a transition by a sharp rise in CTE, which was linked to the T_g of the intergranular glass phase and the potential cause of a reduction

of strength above the T_g. Figure 7.3 displays the CTE data for HP0 and HP20. These samples were chosen because of their difference in intergranular phases (HP0 – Si_2N_2O and $Lu_2Si_2O_7$, HP20-$Lu_4Si_2O_7N_4$) and SiC content. FAST samples were not tested because large samples have not been processed using this technique. Both samples show an increase in CTE at high temperatures, which is likely related to the T_g of the intergranular phase. Even though XRD shows crystalline lutetium containing oxide, there is still amorphous phase between the crystalline oxide and nitride or carbide phase. This has been shown though TEM investigations[96] that an amorphous film tends to exist and has been modeled[100] as well. The HP0 has a lower transition temperature than the HP20 sample. This is likely due to the higher Lu:Si ratio for the HP20 due to the consumption of the glassy phase from the carbothermal reduction reaction. For the HP20 sample there is also a strange shape to the CTE curve in the intermediate temperature range. The cause of this feature is not clear at this time.

High temperature strength and fracture toughness testing is planned for the future of this project. The CTE results can be used to determine the suitable testing temperature.

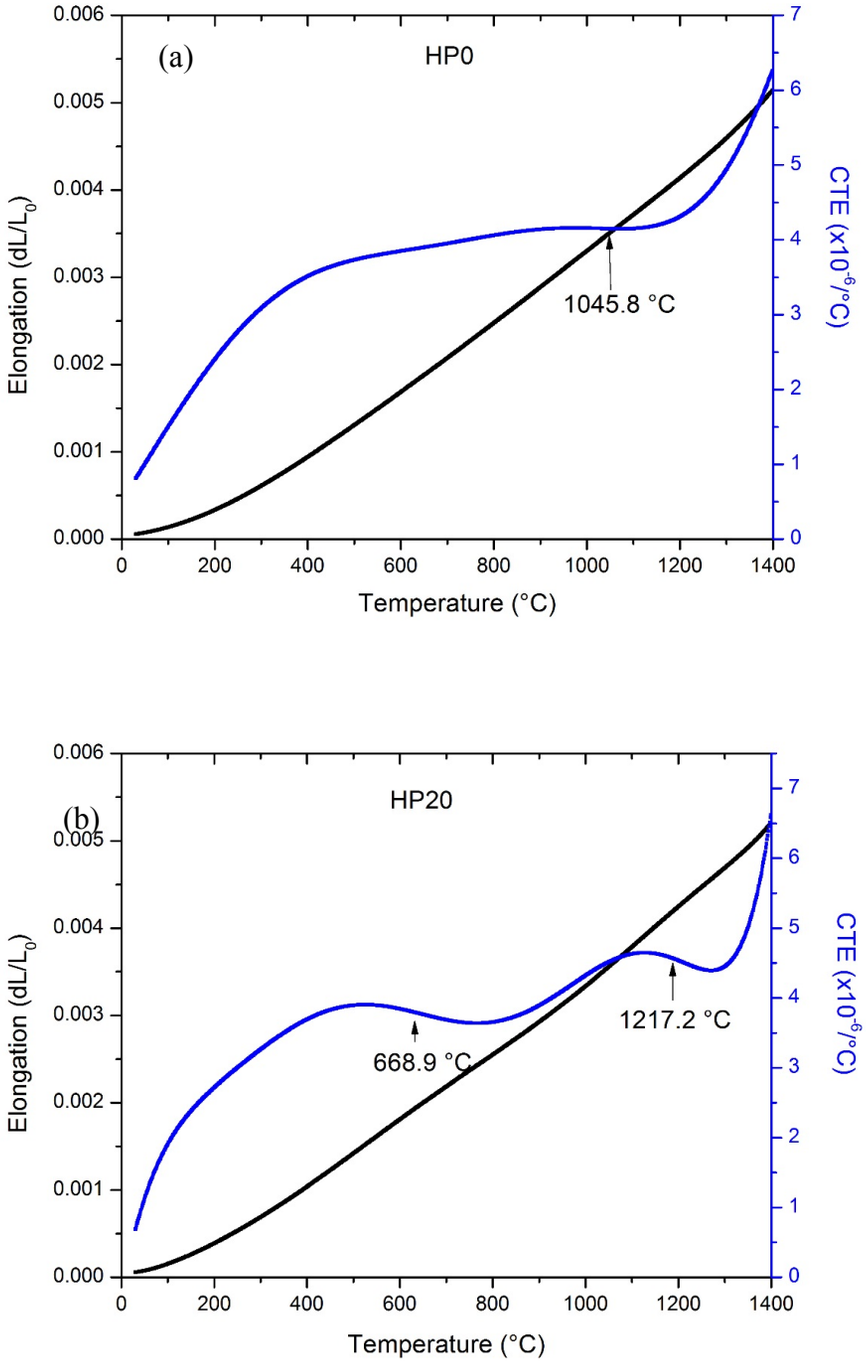

Figure 7.3 Elongation and CTE as a function of temperature for (a) HP0 and (b) HP20.

Chapter 8

Summary and Concluding Remarks

This study has focused on the processing, microstructural characterization and related mechanical property relationship of Si_3N_4/SiC nanocomposites from a single source polysilazane preceramic polymer.

The first half of the study focused on the development of processing protocols using preceramic polymers to produce Si_3N_4/SiC nanocomposites with varying vol.% SiC. A novel process was developed to vary the carbon content of a resulting SiCN polymer derived ceramic through a reactive atmosphere pyrolysis. NH_3 gas was used to react with the preceramic polymer during pyrolysis, which, through a substitution reaction, reduced the carbon content of the resulting SiCN PDC. FTIR characterization of the NH_3 reacted polymer corroborated that the substitution reactions proposed is indeed occurring. Raman spectroscopy was used to characterize the resulting ceramic phase and showed that free carbon existed in the system up to 1850 ˚C, showing that the carbothermal reduction reaction is not instantaneous after crystallization. The processing protocols developed were used to produce SiCN powders, which resulted in SiC content of 0, 5, 10, 20 and 30 vol. % after crystallization heat treatment. An apparatus and procedure to make large quantities of the SiCN powder with the desired C:N ratio was developed.

Hot Pressing (HP) and Field Assisted Sintering (FAST) were used with Lu_2O_3 as a sintering aid to make dense Si_3N_4/SiC nanocomposites. In observing the resulting microstructures, 5 important microstructural features were identified to characterize and quantify: 1) Inter- 2) Intra- granular SiC grain size and distribution, 3) Si_3N_4 grain size and morphology, 4) Lutetium silicate “pockets” and 5) Thin lutetium silicate grain boundaries.

The Si_3N_4 phase in the HP samples showed acicular grains at low volume% SiC. With an increase in SiC there was a reduction in the amount of acicular grains due to a refinement in the microstructure from grain boundary pinning. The FAST samples showed little to no acicular

Si_3N_4 grains. This was attributed to the short processing times, which did not allow for significant grain growth to occur.

There was a reduction in the amount of lutetium silicate "pockets" with an increase in SiC content of the hot pressed samples. This was attributed to the carbothermal reduction of the excess free carbon phase that forms after crystallization of the SiCN PDC with the intergranular glassy phase. The FAST samples showed significantly lower lutetium silicate "pockets" compared to the hot pressed samples. This was attributed to the enhanced wetting properties from the applied electric field, which allowed for even distribution of the lutetium silicate phase.

Quantitative grain size analysis of the SiC phase was completed for the hot press samples. The results showed that the intra-granular SiC was smaller than the inter-granular phase for all HP samples. The size of the SiC grains ranged from 10 – 150 nm. In investigating the SiC phase for the FAST samples a significant amount of free carbon was found in the samples. This was attributed to the short processing time at high temperatures, which did not allow all of the free carbon phase to go through the carbothermal reduction reaction.

Hardness results showed that the FAST0 sample had the highest hardness value due to the very fine microstructures. For FAST samples, there was a decrease in hardness with an increase in the carbon content from the amorphous SiCN due to the soft free phase that remained after processing. Hardness showed no significant change with SiC content for the HP samples. Fracture toughness results showed that there was a transition in fracture toughness where K_{IC} values decreased from HP5 to HP20. This was attributed to the reduction of size and number density of acicular grains with an increase in SiC content. Dilatometer testing showed that there was a sharp increase in CTE at elevated temperatures, which is attributed to the glass transition temperature of the intergranular grain boundary phase.

Chapter 9

Suggested Future Work

This research has focused on the development of a processing approach to make Si_3N_4/SiC nanocomposites with controlled microstructures. Detailed microstructural characterization and preliminary investigation of the mechanical properties has been completed. Suggestions for future work include:

- Image analysis of the Si_3N_4 grain size and morphology
- High temperature fracture toughness testing
- High temperature creep testing
- Room and high temperature elastic modulus testing with resonant ultrasound spectroscopy
- Fracture toughness and dilatometer testing of FAST samples after large samples are processed.
- Fracture toughness testing where the entire R-curve can be measured would be beneficial to determine what are the toughening mechanisms of these nanocomposites. Recent advances in R-curve testing allow for the determination of toughening mechanisms for Si_3N_4 ceramics. Not a significant amount of research has been conducted to determine if the mechanisms for Si_3N_4 are the same as that for the nanocomposite. This is important to determine, as the addition of SiC nanograins tends to reduce toughness in these ceramics.
- Further investigation of the intergranular oxide phase with the use of EELS would be beneficial. Specifically to determine where lutetium is bonding at the interface of the Si_3N_4 and grain boundary phase, and if this bonding changes as you move away from the

Si_3N_4 grains. This is important to understand as these interfaces have a significant effect on properties.

- Close collaboration with colleagues conducting numerical simulations to simulate the effect of the realistic microstructure on properties. Specifically to determine exactly how they numerically simulate microstructures and what information would be most useful to accurately recreate the developed microstructures.

Bibliography

1. Tomar, V.; Gan, M., "Temperature dependent nanomechanics of Si-C-N nanocomposites with an account of particle clustering and grain boundaries", *International Journal of Hydrogen Energy*,**36**, 4605-4616 (2011).
2. Li, Y.; Zhou, M., "Prediction of fracture toughness of Ceramic composites as function of microstructure: I. Numerical Simulations", *Journal of the Mechanics and Physics of Solids*, (2012).
3. Richerson, D. W., "Ceramics for turbine engines", *Mechanical Engineering*,**119** (1997).
4. Caws, R.; Graham, R.; Stoddart, D. E., "Silicon nitride materials for gas turbine components", *American Society of Mechanical Engineers*,**n 73 -GT-47** (1973).
5. Klemm, H., "Silicon Nitride for High-Temperature Applications", *Journal of the American Ceramic Society*,**93**, 1501-1522 (2010).
6. Niihara, K., "New design concept of structural ceramics—ceramic nanocomposites", *Journal of the Ceramic Socity of Japan*,**99**, 974-982 (1991).
7. Niihara, K.; Hirano, T.; Nakahara, A.; Ojima, K.; Izaki, K. In *MRS International Meeting on Advanced Materials, 1 st, Tokyo, Japan* 1989, p 107-112.
8. Niihara, K.; Izaki, K.; Kawakami, T., "Hot-pressed Si 3 N 4-32% SiC nanocomposite from amorphous Si-CN powder with improved strength above 1200° C", *Journal of materials science letters*,**10**, 112-114 (1991).
9. IZAKI, K.; HAKKEI, K.; ANDO, K.; KAWAKAMI, T.; NIIHARA, K., "Fabrication and mechanical properties of Si 3 N 4-SiC composites from fine, amorphous Si-C-N powder precursors", *Ultrastructure processing of advanced ceramics*, 891-900 (1988).
10. Sawaguchi, A.; Toda, K.; Niihara, K., "Mechanical and electrical properties of silicon nitride–silicon carbide nanocomposite material", *Journal of the American Ceramic Society*,**74**, 1142-1144 (1991).
11. Pan, X.; Mayer, J.; Ruhle, M.; Niihara, K., "Silicon nitride based ceramic nanocomposites", *Journal of the American Ceramic Society*,**79**, 585-590 (1996).
12. Niihara, K. H., T.; Izaki, K.; Wakai, F.;, "High Temperature Creep/ Deformation of Si3N4/SiC Nanocomposites", *Ceramic Transactions*,**42** (1994).
13. Niihara, K. H., T.; Nakahira, A.; Suganuma, K.; Izaki, K.; Kawakame, T., "Nanostructure and Thermomechanical Properties of Si3N4/SiC Composites Fabricated from Si-C-N Precursor Powders", *Journal of the Japan Society of Powder and Powder Metallurgy*,**36**, 243 - 247 (1989).
14. Niihara, K. I., K.; Nakahira, A., "The Silicon Nitride-Silicon Carbide Nanocomposites with High Strength at elevated Temperatures", *Journal of Japan Society of Powder and Powder Metallurgy*,**37**, 352 - 356 (1990).
15. Sasaki, G.; Nakase, H.; Suganuma, K.; Fujita, T.; Niihara, K., "Mechanical properties and microstructure of Si3N4 matrix composite with nano-meter scale SiC particles", *Nippon seramikkusu kyokai gakujutsu ronbunshi*,**100**, 536-540 (1992).
16. Hirano, T.; Nakahira, A.; Niihara, K., "Effects of SiC particles on α-β phase transformation and mechanical properties of Si3N4/SiC composites", *Journal of the Japan Society of Powder and Powder Metallurgy*,**41**, 1243 - 1248 (1994).
17. Pezzotti, G.; Sakai, M., "Effect of a Silicon Carbide “Nano-Dispersion” on the Mechanical Properties of Silicon Nitride", *Journal of the American Ceramic Society*,**77**, 3039-3041 (1994).
18. Greskovich, C.; Palm, J., "Observations on the Fracture Toughness of β-Si3N4-β-SiC Composites", *Journal of the American Ceramic Society*,**63**, 597-599 (1980).

19. Turan, S.; Knowles, K. In *Materials Science Forum*; Trans Tech Publ: 1996; Vol. 207, p 357-360.
20. Riedel, R.; Seher, M.; Becker, G., "Sintering of amorphous polymer-derived Si, N and C containing composite powders", *Journal of the European Ceramic Society*,**5**, 113-122 (1989).
21. Zemanova, M.; Lecomte, E.; Sajgalik, P.; Riedel, R., "Polysilazane derived micro/nano Si3N4/SiC composites", *Journal of the European Ceramic Society*,**22**, 2963-2968 (2002).
22. Wan, J.; Duan, R.; Gasch, M.; Mukherjee, A., "Methods of processing Si3N4/SiC nano-nano composites from polymer precursor", *Mat Sci Eng A-Struct*,**424**, 105-116 (2006).
23. Wan, J.; Gasch, M.; Mukherjee, A., "Silicon Nitride–Silicon Carbide Nancocomposites Fabricated by Electric-Field-Assisted Sintering", *Journal of the American Ceramic Society*,**86**, 526-528 (2003).
24. Sajgalik, P.; Hnatko, M.; Lofaj, F.; Hvizdos, P.; Dusza, J.; Warbichler, P.; Hofer, F.; Riedel, R.; Lecomte, E.; Hoffmann, M., "SiC/Si3N4 nano/micro-composite - processing, RT and HT mechanical properties", *Journal of the European Ceramic Society*,**20**, 453-462 (2000).
25. Dusza, J.; Sajgalik, P.; Steen, M., "Fracture toughness of a silicon nitride/silicon carbide nanocomposite at 1350 C", *Journal of the American Ceramic Society*,**82**, 3613-3615 (1999).
26. Dusza, J.; Kasiarova, M.; Vysocka, A.; Spakova, J.; Sajgalik, P., "High Temperature Properties of a SiCN Derived Si3N4+ SiC Micro/Nanocomposite", *High Temperature Materials and Processes*,**26**, 7-16 (2007).
27. Degenhardt, U.; Stegner, F.; Liebscher, C.; Glatzel, U.; Berroth, K.; Krenkel, W.; Motz, G., "Sintered silicon nitride/nano-silicon carbide materials based on preceramic polymers and ceramic powder", *Journal of the European Ceramic Society*, 1-7 (2011).
28. Suzuki, M.; Maniette, Y.; Nakata, Y.; Okutani, T., "Synthesis of silicon carbide–silicon nitride composite ultrafine particles using a carbon dioxide laser", *Journal of the American Ceramic Society*,**76**, 1195-1200 (1993).
29. Besson, J.; Mayne, M.; Bahloul-Hourlier, D.; Goursat, P., "Si3N4/SiCN nanocomposites: Influence of SiC nanoprecipitates on the creep behaviour", *Journal of the European Ceramic Society*,**18**, 1893-1904 (1998).
30. Cauchetier, M.; Croix, O.; Herlin, N.; Luce, M., "Nanocomposite Si/C/N powder production by laser–aerosol interaction", *Journal of the American Ceramic Society*,**77**, 993-998 (1994).
31. Hnatko, M.; Galusek, D.; Sajgalik, P., "Low-cost preparation of Si3N4-SiC micro/nano composites by in-situ carbothermal reduction of silica in silicon nitride matrix", *Journal of the European Ceramic Society*,**24**, 189-195 (2004).
32. Šajgalík, P.; Hnatko, M.; Lenčéš, Z.; Dusza, J.; Kašiarová, M., "In situ preparation of Si3N4/SiC nanocomposites for cutting tools application", *International Journal of Applied Ceramic Technology*,**3**, 41-46 (2006).
33. Hirano, T.; Niihara, K.; Ohji, T.; Wakai, F., "Improved creep resistance of Si3N4/SiC nanocomposites fabricated from amorphous SC-C-N precursor powder", *Journal of materials science letters*,**15**, 505-507 (1996).
34. Park, H.; Kim, H.; Niihara, K., "Microstructure and high-temperature strength of Si3N4-SiC nanocomposite", *Journal of the European Ceramic Society*,**18**, 907-914 (1998).
35. Wakai, F.; KODAMA, Y.; SAKAGUCHI, S.; MURAYAMA, N.; Izaki, K.; Niihara, K., "A SUPERPLASTIC COVALENT CRYSTAL COMPOSITE", *Nature*,**344**, 421-423 (1990).

36. Wan, J.; Gasch, M.; Mukherjee, A., "Silicon nitride-silicon carbide nancocomposites fabricated by electric-field-assisted sintering", *Journal of the American Ceramic Society*,**86**, 526-528 (2003).
37. Wan, J.; Duan, R.; Gasch, M.; Mukherjee, A., "Highly creep-resistant silicon nitride/silicon carbide nano-nano composites", *Journal of the American Ceramic Society*,**89**, 274-280 (2006).
38. Rendtel, A.; Hubner, H.; Herrmann, M.; Schubert, C., "Silicon nitride/silicon carbide nanocomposite materials: II, hot strength, creep, and oxidation resistance", *Journal of the American Ceramic Society*,**81**, 1109-1120 (1998).
39. Šajgalík, P.; Hnatko, M.; Lenčéš, Z.; Dusza, J., "Creep mechanism of SiCN-derived nano/micro composite", *Key Engineering Materials*,**223**, 201-208 (2002).
40. Dusza, J.; Kovalcik, J.; Hvizdos, P.; Sajgalik, P.; Hnatko, M.; Reece, M., "Enhanced creep resistant silicon-nitride-based nanocomposite", *Journal of the American Ceramic Society*,**88**, 1500-1503 (2005).
41. Hegedusova, L.; Kasiarova, M.; Dusza, J.; Hnatko, M.; Sajgalik, P., "Mechanical properties of carbon-derived Si3N4+SiC micro/nano-composite", *Int J Refract Met H*,**27**, 438-442 (2009).
42. Zhou, R.; Feng, Z.; Liang, Y.; Zheng, F.; Xian, Q., "Reactions between SiC and sintering aids in Si 3 N 4/SiC nanocomposites and their consequences", *Ceramics International*,**27**, 571-576 (2001).
43. Herrmann, M.; Schuber, C.; Rendtel, A.; Hubner, H., "Silicon nitride/silicon carbide nanocomposite materials: I, fabrication and mechanical properties at room temperature", *Journal of the American Ceramic Society*,**81**, 1095-1108 (1998).
44. Niihara, K.; Suganuma, K.; Nakahira, A.; Izaki, K., "INTERFACES IN SI3N4-SIC NANO-COMPOSITE", *Journal of materials science letters*,**9**, 598-599 (1990).
45. Balog, M.; Keckes, J.; Schoberl, T.; Galusek, D.; Hofer, F.; Krest'an, J.; Lences, Z.; Huang, J.-L.; Sajgalik, P., "Nano/macro-hardness and fracture resistance of Si3N4/SiC composites with up to 13 wt.% of SiC nano-particles", *Journal of the European Ceramic Society*,**27**, 2145-2152 (2007).
46. Lojanova, S.; Tatarko, P.; Chlup, Z.; Hnatko, M.; Dusza, J.; Lences, Z.; Sajgalik, P., "Rare-earth element doped Si3N4/SiC micro/nano-composites-RT and HT mechanical properties", *Journal of the European Ceramic Society*,**30**, 1931-1944 (2010).
47. Pezzotti, G.; Tanaka, I.; Okamoto, T., "Si3N4/SiC-Whisker Composites without Sintering Aids: III, High-Temperature Behavior", *Journal of the American Ceramic Society*,**74**, 326-332 (1991).
48. Goto, Y.; Tsuge, A., "Mechanical Properties of Unidirectionally Oriented SiC-Whisker-Reinforced Si3N4 Fabricated by Extrusion and Hot-Pressing", *Journal of the American Ceramic Society*,**76**, 1420-1424 (1993).
49. Backhaus-Ricoult, M.; Castaing, J.; Routbort, J., "Creep of SiC-whisker reinforced Si3N4", *Revue de physique appliquée*,**23**, 239-249 (1988).
50. Nixon, R.; Koester, D.; Chevacharoenkul, S.; Davis, R., "Steady-state creep of hot-pressed SiC whisker-reinforced silicon nitride", *Composites science and technology*,**37**, 313-328 (1990).
51. Hockey, B.; Wiederhorn, S.; Liu, W.; Baldoni, J.; Buljan, S.-T., "Tensile creep of whisker-reinforced silicon nitride", *Journal of Materials Science*,**26**, 3931-3939 (1991).
52. Chu, C. Y.; Singh, J. P.; Routbort, J. L., "High-Temperature Failure Mechanisms of Hot-Pressed Si3N4 and Si3N4/Si3N4-Whisker-Reinforced Composites", *Journal of the American Ceramic Society*,**76**, 1349-1353 (1993).

53. Claussen, N. In *Structural Ceramics, Processing, Microstructure and Properties. 11 th RISO Int. Symp. on Metallurgy and Materials Science Roskilde, Denmark* 1990; Vol. 3.
54. Pezzotti, G., "Si3N4/SiC-Platelet Composite without Sintering Aids: A Candidate for Gas Turbine Engines", *Journal of the American Ceramic Society*,**76**, 1313-1320 (1993).
55. Acchar, W.; Hubner, H.; Schubert, C., "CREEP OF HOT-PRESSED SILICON NITRIDE(HPSN) REINFORCED BY SILICON CARBIDE PLATELETS", *Euro-Ceramics II.*,**2**, 1559-1563 (1991).
56. Acchar, W.; Rendtel, A.; Hubner, H. In *Third ECers. Proc. 3 rd European Ceramic Society Conf.* 1993; Vol. 3, p 405-410.
57. Rendtel, A.; Huebner, H.; Schubert, C., "Effect of platelet addition on the strength and creep resistance of hot-pressed silicon nitride", *Silicates Industriels*,**60**, 305-312 (1995).
58. Lange, F., "EFFECT OF MICROSTRUCTURE ON STRENGTH OF SI3N4-SIC COMPOSITE SYSTEM", *Journal of the American Ceramic Society*,**56**, 445-450 (1973).
59. Rahaman, M. H. *Ceramic Processing and Sintering*; 2 ed.; CRC Press Taylor & Francis Group: Boca Raton, FL, 2003.
60. Ishizaki, K., "Phase diagrams under high total gas pressures--Ellingham diagrams for hot isostatic press processes", *Acta Metallurgica et Materialia*,**38**, 2059-2066 (1990).
61. Singhal, S. C., "Thermodynamic analysis of the high-temperature stability of silicon nitride and silicon carbide", *Ceramurgia International*,**2**, 123-130 (1976).
62. Deeley, G.; Herbert, J.; Moore, N., "DENSE SILICON NITRIDE*", *Powder Metallurgy*,**4**, 145-151 (1961).
63. TERWILLI.GR; Lange, F., "HOT-PRESSING BEHAVIOR OF SI3N4", *Journal of the American Ceramic Society*,**57**, 25-29 (1974).
64. Lange, F., "RELATION BETWEEN STRENGTH, FRACTURE ENERGY, AND MICROSTRUCTURE OF HOT-PRESSED SI3N4", *Journal of the American Ceramic Society*,**56**, 518-522 (1973).
65. Bowen, L.; Weston, R. J.; Carruthers, T.; Brook, R., "Hot-pressing and the α-β phase transformation in silicon nitride", *Journal of Materials Science*,**13**, 341-350 (1978).
66. Lange, F.; SINGHAL, S.; Kuznicki, R., "PHASE RELATIONS AND STABILITY STUDIES IN SI3N4-SIO2-Y2O3 PSEUDOTERNARY SYSTEM", *Journal of the American Ceramic Society*,**60**, 249-252 (1977).
67. Gazza, G. E., "EFFECT OF YTTRIA ADDITIONS ON HOT-PRESSED SI3N4", *Am. Ceram. Soc. Bull.*,**54**, 778-781 (1975).
68. Sajgalik, P.; Dusza, J.; Hoffmann, M., "RELATIONSHIP BETWEEN MICROSTRUCTURE, TOUGHENING MECHANISMS, AND FRACTURE-TOUGHNESS OF REINFORCED SILICON-NITRIDE CERAMICS", *Journal of the American Ceramic Society*,**78**, 2619-2624 (1995).
69. Sun, E.; Becher, P.; Plucknett, K.; Hsueh, C.; Alexander, K.; Waters, S.; Hirao, K.; Brito, M., "Microstructural design of silicon nitride with improved fracture toughness: II, effects of yttria and alumina additives", *Journal of the American Ceramic Society*,**81**, 2831-2840 (1998).
70. AHN, C.; THOMAS, G., "MICROSTRUCTURE AND GRAIN-BOUNDARY COMPOSITION OF HOT-PRESSED SILICON-NITRIDE WITH YTTRIA AND ALUMINA", *Journal of the American Ceramic Society*,**66**, 14-17 (1983).
71. Yang, J. F.; Ohji, T.; Niihara, K., "Influence of yttria-alumina content on sintering behavior and microstructure of silicon nitride ceramics", *Journal of the American Ceramic Society*,**83**, 2094-2096 (2000).

72. Drew, P.; Lewis, M., "The microstructures of silicon nitride/alumina ceramics", *Journal of Materials Science*,**9**, 1833-1838 (1974).
73. Becher, P.; Sun, E.; Plucknett, K.; Alexander, K.; Hsueh, C.; Lin, H.; Waters, S.; Westmoreland, C.; Kang, E.; Hirao, K.; Brito, M., "Microstructural design of silicon nitride with improved fracture toughness: I, effects of grain shape and size", *Journal of the American Ceramic Society*,**81**, 2821-2830 (1998).
74. Yang, J. F.; Ohji, T.; Niihara, K., "Influence of yttria–alumina content on sintering behavior and microstructure of silicon nitride ceramics", *Journal of the American Ceramic Society*,**83**, 2094-2096 (2000).
75. KRAMER, M.; Hoffmann, M.; Petzow, G., "GRAIN-GROWTH STUDIES OF SILICON-NITRIDE DISPERSED IN AN OXYNITRIDE GLASS", *Journal of the American Ceramic Society*,**76**, 2778-2784 (1993).
76. Lehner, W.; Kleebe, H.; Ziegler, G., "Variation of sintering parameters at an early stage of densification affecting beta-Si3N4-microstructure", *Journal of the European Ceramic Society*,**26**, 201-208 (2006).
77. Becher, P.; Sun, E.; Hsueh, C.; Alexander, K.; Hwang, S.; Waters, S.; Westmoreland, C., "Debonding of interfaces between beta-silicon nitride whiskers and Si-Al-Y oxynitride glasses", *Acta Materialia*,**44**, 3881-3893 (1996).
78. Becher, P. F.; Painter, G. S.; Shibata, N.; Satet, R. L.; Hoffmann, M. J.; Pennycook, S. J., "Influence of additives on anisotropic grain growth in silicon nitride ceramics", *Mat Sci Eng A-Struct*,**422**, 85-91 (2006).
79. Painter, G.; Becher, P.; Shelton, W.; Satet, R.; Hoffmann, M., "First-principles study of rare-earth effects on grain growth and microstructure in beta-Si3N4 ceramics", *Phys. Rev. B*,**70**, 144108 (2004).
80. Becher, P.; Ferber, M., "Temperature-dependent viscosity of SiREAl-based classes as a function of N : O and RE : Al ratios (RE = La, Gd, Y, and Lu)", *Journal of the American Ceramic Society*,**87**, 1274-1279 (2004).
81. Becher, P. F.; Shibata, N.; Painter, G. S.; Averill, F.; van Benthem, K.; Lin, H.-T.; Waters, S. B., "Observations on the Influence of Secondary Me Oxide Additives (Me = Si, Al, Mg) on the Microstructural Evolution and Mechanical Behavior of Silicon Nitride Ceramics Containing RE2O3 (RE = La, Gd, Lu)", *Journal of the American Ceramic Society*,**93**, 570-580 (2010).
82. GAZZA, G., "EFFECT OF YTTRIA ADDITIONS ON HOT-PRESSED SI3N4", *Am Ceram Soc Bull*,**54**, 778-781 (1975).
83. Stemmer, S.; Roebben, G.; Van der Biest, O., "Evolution of grain boundary films in liquid phase sintered silicon nitride during high-temperature testing", *Acta materialia*,**46**, 5599-5606 (1998).
84. Belmonte, M.; Gonzalez-Julian, J.; Miranzo, P.; Osendi, M. I., "Spark plasma sintering: A powerful tool to develop new silicon nitride-based materials", *Journal of the European Ceramic Society*,**30**, 2937-2946 (2010).
85. Shen, Z.; Zhao, Z.; Peng, H.; Nygren, M., "Formation of tough interlocking microstructures in silicon nitride ceramics by dynamic ripening_SUPPLEMENTAL", *Nature*, 1-5 (2002).
86. Herrmann, M.; Shen, Z.; Schulz, I.; Hu, J.; Jancar, B., "Silicon nitride nanoceramics densified by dynamic grain sliding", *Journal of Materials Research*,**25**, 2354-2361 (2010).
87. Hotta, M.; Shinoura, T.; Enomoto, N.; Hojo, J., "Spark Plasma Sintering of Nanosized Amorphous Silicon Nitride Powder with a Small Amount of Sintering Additive", *Journal of the American Ceramic Society*,**93**, 1544-1546 (2010).

88. Munir, Z.; Anselmi-Tamburini, U.; Ohyanagi, M., "The effect of electric field and pressure on the synthesis and consolidation of materials: A review of the spark plasma sintering method", *Journal of Materials Science*,**41**, 763-777 (2006).
89. Belmonte, M.; Osendi, M. I.; Miranzo, P., "Modeling the effect of pulsing on the spark plasma sintering of silicon nitride materials", *Scripta Materialia*,**65**, 273-276 (2011).
90. Norton, F., "THE FLOW OF CERAMIC BODIES AT ELEVATED TEMPERATURES*", *Journal of the American Ceramic Society*,**19**, 129-134 (1936).
91. Herring, C., "DIFFUSIONAL VISCOSITY OF A POLYCRYSTALLINE SOLID", *Journal of Applied Physics*,**21**, 437-445 (1950).
92. COBLE, R., "A MODEL FOR BOUNDARY DIFFUSION CONTROLLED CREEP IN POLYCRYSTALLINE MATERIALS", *Journal of Applied Physics*,**34**, 1679-& (1963).
93. Raj, R.; Chyung, C., "SOLUTION-PRECIPITATION CREEP IN GLASS-CERAMICS", *Acta Metallurgica*,**29**, 159-166 (1981).
94. Raj, R., "Creep in polycrystalline aggregates by matter transport through a liquid phase", *Journal of Geophysical Research*,**87**, 4731-4739 (1982).
95. Wakai, F., "STEP MODEL OF SOLUTION-PRECIPITATION CREEP", *Acta Metallurgica et Materialia*,**42**, 1163-1172 (1994).
96. Wiederhorn, S. M.; Hockey, B.; French, J., "Mechanisms of deformation of silicon nitride and silicon carbide at high temperatures", *Journal of the European Ceramic Society*,**19**, 2273-2284 (1999).
97. Luecke, W. E.; Wiederhorn, S. M., "A new model for tensile creep of silicon nitride", *Journal of the American Ceramic Society*,**82**, 2769-2778 (1999).
98. Wereszczak, A.; Ferber, M.; Kirkland, T.; Barnes, A.; Frome, E.; Menon, M., "Asymmetric tensile and compressive creep deformation of hot-isostatically-pressed Y2O3-doped-Si3N4", *Journal of the European Ceramic Society*,**19**, 227-237 (1999).
99. Kleebe, H.-J., "Structure and chemistry of interfaces in Si3N4 ceramics studied by transmission electron microscopy", *Nippon seramikkusu kyokai gakujutsu ronbunshi*,**105**, 453-475 (1997).
100. Clarke, D. R., "On the equilibrium thickness of intergranular glass phases in ceramic materials", *Journal of the American Ceramic Society*,**70**, 15-22 (1987).
101. Lofaj, F.; Satet, R.; Hoffmann, M.; de Arellano Lopez, A., "Thermal expansion and glass transition temperature of the rare-earth doped oxynitride glasses", *Journal of the European Ceramic Society*,**24**, 3377-3385 (2004).
102. Lofaj, F.; Dériano, S.; LeFloch, M.; Rouxel, T.; Hoffmann, M. J., "Structure and rheological properties of the RE–Si–Mg–O–N (RE= Sc, Y, La, Nd, Sm, Gd, Yb and Lu) glasses", *Journal of Non-Crystalline Solids*,**344**, 8-16 (2004).
103. Raghavendra, R.; Nestor, E.; Pomeroy, M.; Hampshire, S., "Formation of Ln-Si-Al-ON Glasses and their Properties", *Journal of the European Ceramic Society*, (1997).
104. Hampshire, S., "Oxynitride glasses, their properties and crystallisation–a review", *Journal of Non-Crystalline Solids*,**316**, 64-73 (2003).
105. Besson, J.; Doucey, B.; Lucas, S.; Bahloul-Hourlier, D.; Goursat, P., "SiCN nanocomposite: creep behaviour", *Journal of the European Ceramic Society*,**21**, 959-968 (2001).
106. Dusza, J.; Kovalik, J.; Hvizdos, P.; Sajgalik, P.; Hnatko, M.; Reece, M., "Creep behavior of a carbon-derived Si3N4/SiC nanocomposite", *Journal of the European Ceramic Society*,**24**, 3307-3315 (2004).
107. Tanaka, I.; Pezzotti, G., "Delayed-Failure Resistance of High-Purity Si3N4 at 1400° C", *Journal of the American Ceramic Society*,**75**, 1023-1025 (1992).
108. Green, D. J. *An introduction to the mechanical properties of ceramics*; Cambridge University Press, 1998.

109. Griffith, A. A., "The phenomena of rupture and flow in solids", *Philosophical transactions of the royal society of london. Series A, containing papers of a mathematical or physical character*, 163-198 (1921).
110. Lange, F. F., "Powder processing science and technology for increased reliability", *Journal of the American Ceramic Society*,**72**, 3-15 (1989).
111. Hübner, H.; Jillek, W., "Sub-critical crack extension and crack resistance in polycrystalline alumina", *Journal of Materials Science*,**12**, 117-125 (1977).
112. Faber, K.; Evans, A., "Crack deflection processes—I. Theory", *Acta Metallurgica*,**31**, 565-576 (1983).
113. Becher, P., "MICROSTRUCTURAL DESIGN OF TOUGHENED CERAMICS", *Journal of the American Ceramic Society*,**74**, 255-269 (1991).
114. Claussen, N.; Steeb, J.; Pabst, R. F., "Effect on induced microcracking on the fracture toughness of ceramics", *Am. Ceram. Soc. Bull.*,**56**, 559-562 (1977).
115. McMeeking, R.; Evans, A., "Mechanics of Transformation-Toughening in Brittle Materials", *Journal of the American Ceramic Society*,**65**, 242-246 (1982).
116. Fett, T. *New contributions to R-curves and bridging stresses-Applications of weight functions*; KIT Scientific Publishing, 2014.
117. Fuenfschilling, S.; Fett, T.; Hoffmann, M. J.; Oberacker, R.; Schwind, T.; Wippler, J.; Boehlke, T.; Oezcoban, H.; Schneider, G. A.; Becher, P. F.; Kruzic, J. J., "Mechanisms of toughening in silicon nitrides: The roles of crack bridging and microstructure", *Acta Materialia*,**59**, 3978-3989 (2011).
118. Sun, E.; Becher, P.; Hsueh, C.; Painter, G.; Waters, S.; Hwang, S.; Hoffmann, M., "Debonding behavior between beta-Si3N4 whiskers and oxynitride glasses with or without an epitaxial beta-SiAlON interfacial layer", *Acta Materialia*,**47**, 2777-2785 (1999).
119. Fett, T.; Fünfschilling, S.; Hoffmann, M. J.; Oberacker, R.; Jelitto, H.; Schneider, G. A., "R-Curve Determination for the Initial Stage of Crack Extension in Si3N4", *Journal of the American Ceramic Society*,**91**, 3638-3642 (2008).
120. Fünfschilling, S.; Fett, T.; Oberacker, R.; Hoffmann, M. J.; Özcoban, H.; Jelitto, H.; Schneider, G. A.; Kruzic, J. J., "R Curves from Compliance and Optical Crack-Length Measurements", *Journal of the American Ceramic Society*,**93**, 2814-2821 (2010).
121. Rouxel, T.; Wakai, F.; Sakaguchi, S., "R-Curve Behavior and Stable Crack Growth at Elevated Temperature (1500°–1650° C) in a Si3N4/SiC Nanocomposite", *Journal of the American Ceramic Society*,**77**, 3237-3243 (1994).
122. Wereszczak, A.; Lin, H.-T.; Kirkland, T.; Andrews, M.; Lee, S., "Strength and dynamic fatigue of silicon nitride at intermediate temperatures", *Journal of Materials Science*,**37**, 2669-2684 (2002).
123. Riedel, R.; Mera, G.; Hauser, R.; Klonczynski, A., "Silicon-Based Polymer-Derived Ceramics: Synthesis Properties and Applications-A Review Dedicated to Prof. Dr. Fritz Aldinger on the occasion of his 65th birthday", *Journal of the Ceramic Society of Japan*,**114**, 425-444 (2006).
124. Colombo, P.; Mera, G.; Riedel, R.; Soraru, G. D., "Polymer-Derived Ceramics: 40 Years of Research and Innovation in Advanced Ceramics", *Journal of the American Ceramic Society*,**93**, 1805-1837 (2010).
125. Colombo, P. *Polymer derived ceramics: from nano-structure to applications*; DEStech Publications, Inc, 2010.
126. Li, Y. L.; Kroke, E.; Riedel, R.; Fasel, C.; Gervais, C.; Babonneau, F., "Thermal cross-linking and pyrolytic conversion of poly (ureamethylvinyl) silazanes to silicon-based ceramics", *Appl. Organometal. Chem.*,**15**, 820-832 (2001).
127. Lee, R., "Carbosilanes: Reactions & Mechanisms of SMP-10 Pre-Ceramic Polymers", 1-23 (2009).

128. Iwamoto, Y.; Volger, W.; Kroke, E.; Riedel, R.; Saitou, T.; Matsunaga, K., "Crystallization behavior of amorphous silicon carbonitride ceramics derived from organometallic precursors", *Journal of the American Ceramic Society*,**84**, 2170-2178 (2001).
129. Lavedrine, A.; Bahloul, D.; Goursat, P.; Yive, N. C. K.; Corriu, R.; Leclerq, D.; Mutin, H.; Vioux, A., "Pyrolysis of polyvinylsilazane precursors to silicon carbonitride", *Journal of the European Ceramic Society*,**8**, 221-227 (1991).
130. Choong Kwet Yive, N.; Corriu, R.; Leclercq, D.; Mutin, P.; Vioux, A., "Silicon carbonitride from polymeric precursors: thermal cross-linking and pyrolysis of oligosilazane model compounds", *Chemistry of materials*,**4**, 141-146 (1992).
131. Babonneau, F.; Soraru, G.; Mackenzie, J., "29Si MAS-NMR investigation of the conversion process of a polytitanocarbosilane into SiC-TiC ceramics", *Journal of Materials Science*,**25**, 3664-3670 (1990).
132. Laine, R. M.; Babonneau, F.; Blowhowiak, K. Y.; Kennish, R. A.; Rahn, J. A.; Exarhos, G. J.; Waldner, K., "The Evolutionary Process during Pyrolytic Transformation of Poly (N-methylsilazane) from a Preceramic Polymer into an Amorphous Silicon Nitride/Carbon Composite", *Journal of the American Ceramic Society*,**78**, 137-145 (1995).
133. Seitz, J.; Bill, J.; Egger, N.; Aldinger, F., "Structural investigations of Si/C/N-ceramics from polysilazane precursors by nuclear magnetic resonance", *Journal of the European Ceramic Society*,**16**, 885-891 (1996).
134. Mera, G.; Riedel, R.; Poli, F.; Müller, K., "Carbon-rich SiCN ceramics derived from phenyl-containing poly (silylcarbodiimides)", *Journal of the European Ceramic Society*,**29**, 2873-2883 (2009).
135. CORRIU, R.; LECLERCQ, D.; MUTIN, P.; VIOUX, A., "THERMOGRAVIMETRIC MASS-SPECTROMETRIC INVESTIGATION OF THE THERMAL-CONVERSION OF ORGANOSILICON PRECURSORS INTO CERAMICS UNDER ARGON AND AMMONIA .1. POLY(CARBOSILANE)", *Chemistry of materials*,**4**, 711-716 (1992).
136. YIVE, N.; CORRIU, R.; LECLERCQ, D.; MUTIN, P.; VIOUX, A., "THERMOGRAVIMETRIC ANALYSIS MASS-SPECTROMETRY INVESTIGATION OF THE THERMAL-CONVERSION OF ORGANOSILICON PRECURSORS INTO CERAMICS UNDER ARGON AND AMMONIA .2. POLY(SILAZANES)", *Chemistry of materials*,**4**, 1263-1271 (1992).
137. Golczewski, J.; Aldinger, F., "Thermodynamic modeling of amorphous Si-CN ceramics derived from polymer precursors", *Journal of Non-Crystalline Solids*,**347**, 204-210 (2004).
138. GOLCZEWSKI, J., "Thermodynamic Analysis of Isothermal Crystallization of Amorphous Si-CN Ceramics Derived from Polymer Precursors", *Journal of the Ceramic Society of Japan*,**114**, 950-957 (2006).
139. Galusek, D.; Reschke, S.; Riedel, R.; Dressler, W.; Sajgalik, P.; Lencees, Z.; Majling, J., "In-situ carbon content adjustment in polysilazane derived amorphous SiCN bulk ceramics", *Journal of the European Ceramic Society*,**19**, 1911-1921 (1999).
140. Friess, M.; Bill, J.; Golczewski, J.; Zimmermann, A.; Aldinger, F.; Riedel, R.; Raj, R., "Crystallization of polymer-derived silicon carbonitride at 1873 K under nitrogen overpressure", *Journal of the American Ceramic Society*,**85**, 2587-2589 (2002).
141. Nicolich, J.; Lences, Z.; Dressler, W.; Riedel, R., "Phase quantification of beta-Si3N4/beta-SiC mixtures by X-ray powder diffraction analysis", *Journal of Materials Science*,**35**, 1427-1432 (2000).
142. LI, D.; OCONNOR, B.; CHEN, Q.; ZADNIK, M., "QUANTITATIVE POWDER X-RAY-DIFFRACTOMETRY PHASE-ANALYSIS OF SILICON NITRIC MATERIALS BY A MULTILINE, MEAN-NORMALIZED-INTENSITY METHOD", *Journal of the American Ceramic Society*,**77**, 2195-2198 (1994).

143. Standard, A., "C1327-08", *Standard Test Method for Vickers Indentation Hardness of Advanced Ceramics*, (2003).
144. Kübler, J. In *Proceedings of the 21st Annual Conference on Composites, Advanced Ceramics, Materials, and Structures-B: Ceramic Engineering and Science Proceedings, Volume 18, Issue 4*; Wiley Online Library: 1997, p 155-162.
145. Haluschka, C.; Kleebe, H.-J.; Franke, R.; Riedel, R., "Silicon carbonitride ceramics derived from polysilazanes Part I. Investigation of compositional and structural properties", *Journal of the European Ceramic Society*,**20**, 1355-1364 (2000).
146. Trassl, S.; Motz, G.; Rössler, E.; Ziegler, G., "Characterization of the Free-Carbon Phase in Precursor-Derived Si-CN Ceramics: I, Spectroscopic Methods", *Journal of the American Ceramic Society*,**85**, 239-244 (2002).
147. Concas, A.; Lai, N.; Pisu, M.; Cao, G., "Modelling of comminution processes in Spex Mixer/Mill", *Chemical Engineering Science*,**61**, 3746-3760 (2006).
148. Austin, L., "Understanding ball mill sizing", *Industrial & Engineering Chemistry Process Design and Development*,**12**, 121-129 (1973).
149. Rabe, T.; Linke, D., "Attrition milling of silicon nitride powder under conditions for minimal impurity pickup", *Ceramics international*,**18**, 161-166 (1992).
150. Suttor, D.; FISCHMAN, G., "DENSIFICATION AND SINTERING KINETICS IN SINTERED SILICON-NITRIDE", *Journal of the American Ceramic Society*,**75**, 1063-1067 (1992).
151. Chapman, S.; Rasch, R., "High Spatial Resolution X-Ray Analysis in a SEM", *Microscopy Today*,**22**, 24-27 (2014).
152. Hall, E., "The deformation and ageing of mild steel: III discussion of results", *Proceedings of the Physical Society. Section B*,**64**, 747 (1951).
153. Petch, N., "The cleavage strength of polycrystals", *J. Iron Steel Inst.*,**174**, 25-28 (1953).